

AD-A172 159

API-TR-129

RADAR CROSS-SECTION EVALUATION
OF ARBITRARY CYLINDERS

Final Report

ITEM 0004

September 12, 1986

Prepared by
Richard Holland
Kah-Song Cho

for
Office of Naval Research

Under
Contract Number N00014-85-C-0852

This document has been approved
for public release and sale; its
distribution is unlimited.

Applied Physics, Inc.

5353 Wyoming Blvd., NE, Suite 3 Albuquerque, New Mexico 87109
(505) 823-2334

86 9 19 067

UNCLASSIFIED
SECURITY CLASSIFICATION OF THIS PAGE

REPORT DOCUMENTATION PAGE				
1a. REPORT SECURITY CLASSIFICATION Unclassified		1b. RESTRICTIVE MARKINGS Approved for Public Release		
2a. SECURITY CLASSIFICATION AUTHORITY DARPA Technical Information Office		3. DISTRIBUTION/AVAILABILITY OF REPORT Distribution is unlimited		
2b. DECLASSIFICATION/DOWNGRADING SCHEDULE N/A				
4. PERFORMING ORGANIZATION REPORT NUMBER(S) Final Report Item 0004 API-TR-129		5. MONITORING ORGANIZATION REPORT NUMBER(S)		
6a. NAME OF PERFORMING ORGANIZATION Applied Physics, Inc.		6b. OFFICE SYMBOL (If applicable)		7a. NAME OF MONITORING ORGANIZATION Office of Naval Research
6c. ADDRESS (City, State and ZIP Code) 5353 Wyoming Blvd, NE, Suite 3 Albuquerque, NM 87109		7b. ADDRESS (City, State and ZIP Code) 800 N. Quincy Street Arlington, VA 22217		
8a. NAME OF FUNDING/SPONSORING ORGANIZATION DARPA		8b. OFFICE SYMBOL (If applicable)		9. PROCUREMENT INSTRUMENT IDENTIFICATION NUMBER N00014-85-C-0852
8c. ADDRESS (City, State and ZIP Code) 1400 Wilson Blvd. Arlington, VA 22209		10. SOURCE OF FUNDING NUMBERS PROGRAM ELEMENT NO. PROJECT NO. TASK NO. WORK UNIT ACCESSION NO.		
11. TITLE (Include Security Classification) Radar Cross Section Evaluation of Arbitrary Cylinders (U)				
12. PERSONAL AUTHOR(S) Richard Holland and Kah-Song Cho				
13a. TYPE OF REPORT Final		13b. TIME COVERED FROM 9/85 TO 9/86		14. DATE OF REPORT (Year, Month, Day) 15 Sept 86
15. PAGE COUNT 121				
16. SUPPLEMENTARY NOTATION				
17. COSATI CODES FIELD GROUP SUB-GROUP			18. SUBJECT TERMS (Continue on reverse if necessary and identify by block number) TDFD codes, echo widths, RCS calculation stealth, dielectric strips, Mathieu functions, anisotropic dielectrics, Prony analysis	
19. ABSTRACT (Continue on reverse if necessary and identify by block number) (U) This report presents 2D monostatic and bistatic RCS (echo width) calculations for electrically and magnetically conducting circular cylinders with and without an electromagnetically damping coat. Similar calculations for dielectric cylinders and thin dielectric strips are also given. In all cases, results are computed by our new TDFD code, transformed to the frequency domain, and overlaid with canonical calculations performed directly in the frequency domain. Agreement of 10% is achieved if the TDFD code uses at least 16 cells per wavelength. To date we have not used meshes larger than 50 x 50 cells or 125 x 25 cells, but these are not intrinsic limits.				
20. DISTRIBUTION/AVAILABILITY OF ABSTRACT <input checked="" type="checkbox"/> UNCLASSIFIED/UNLIMITED <input type="checkbox"/> SAME AS RPT. <input type="checkbox"/> DTIC USERS			21. ABSTRACT SECURITY CLASSIFICATION	
22a. NAME OF RESPONSIBLE INDIVIDUAL			22b. TELEPHONE (Include Area Code)	22c. OFFICE SYMBOL

(U) Detailed documentation of the TDFD RCS code is given. The TDFD code can treat anisotropic, frequency dependent scatterers and scatterers with abrupt electrical discontinuities, such as resistive or conducting cards. Results of these cases are not presented due to lack of canonical examples for comparison.

(U) Also presented, however, are the canonical solutions for scattering by a conducting elliptic cylinder, a lossless dielectric elliptic cylinder, and a lossless two-medium elliptic cylinder with the outer and inner media confocally delineated. In the latter case, the inner medium could be a perfectly conducting card.

CONTENTS

	Page
INTRODUCTION	1
ARCHITECTURE OF THE TIME-DOMAIN FINITE-DIFFERENCE	
RCS CODE	3
Equations to be Solved	3
Method of Solution	7
Introduction of Frequency Dependence	17
Transformation from the Near-field Time Domain to the	
Far-field Frequency Domain	25
CANONICAL SOLUTIONS AND CODE-CODE COMPARISONS.	36
Scattering from a Layered Dielectric Cylinder.	36
Scattering from a Thin Dielectric Strip.	74
Elliptic Cylinder Scattering	90
SUMMARY.	111
REFERENCES	112
APPENDIX 1	113



Accession For	
NTIS GRA&I	<input checked="checked" type="checkbox"/>
DTIC TAB	<input type="checkbox"/>
Unannounced	<input type="checkbox"/>
Justification	
By	
Distribution/	
Availability Codes	
Dist	Avail and/or Special
A-1	

CONTENTS

	Page
INTRODUCTION	1
ARCHITECTURE OF THE TIME-DOMAIN FINITE-DIFFERENCE	
RCS CODE	3
Equations to be Solved	3
Method of Solution	7
Introduction of Frequency Dependence	17
Transformation from the Near-field Time Domain to the	
Far-field Frequency Domain	25
CANONICAL SOLUTIONS AND CODE-CODE COMPARISONS.	36
Scattering from a Layered Dielectric Cylinder.	36
Scattering from a Thin Dielectric Strip.	74
Elliptic Cylinder Scattering	90
SUMMARY.	111
REFERENCES	112
APPENDIX 1	113

RADAR CROSS SECTION EVALUATION OF ARBITRARY CYLINDERS

INTRODUCTION

The objective of this program has been to develop a 2D code and numerical technique for determining the Radar Cross Section (RCS) and other electromagnetic scattering behavior of an infinite cylinder of arbitrary cross-sectional shape and material composition. Both monostatic and bistatic RCS's need be obtained.

The technique we have used to meet this objective differs greatly from conventional methods of RCS evaluation. Rather than working in the frequency domain, we have illuminated the target by an Electromagnetic Pulse (EMP) containing significant energy over all frequencies of interest. We have then solved the near-field problem by Time-Domain Finite Differencing (TDFD), and Fourier transformed the result to obtain the desired RCS as a function of frequency. A near-field to far-field transformation is also incorporated into our Fourier procedure.

Our technique has been tested with targets up to 5 m across to obtain results from 50 to 500 MHz. (These parameters correspond to a maximum of 8 free-space wavelengths.) There is no reason we could not obtain information up to 1 GHz, although we have not actually done this to date in the interest of conserving computer resources.

We have run test cases using generalized lossy inhomogeneous media, where the real and imaginary parts of the permittivity or permeability are frequency and position dependent. Additionally, the code is generalized to treat materials with anisotropy in the plane perpendicular to the cylinder axis. The code can also treat generalized material discontinuities including resistive, capacitive and conductive cards.

Additionally, we have obtained canonical solutions to several problems with known frequency-domain solutions in order to evaluate the accuracy of our code. These problems include a circular cylinder composed of an arbitrary number of concentric cylindrical shells, where the electrical

parameters of each shell are arbitrary (but isotropic). We have also computed the scattering by a thin dielectric strip of infinite extent, using the technique of Richmond.¹ Code-code comparisons between the canonical and TDFD results for these two problems will be presented later.

Additionally, we have derived the equations for scattering by a perfect, circular dielectric cylinder with anisotropy in the plane perpendicular to the cylinder axis. At present, we have not had time to code up this canonical solution.

Also, we have worked out the Mathieu-function expansion for scattering off a perfect, elliptic dielectric cylinder. This solution has been coded, and gives answers which, in the perfect-conductor limit, agree with known results. We have, as of yet, not run a comparative TDFD case. This Mathieu-function expansion has been generalized to treat the case of a two-media elliptical cylinder with the outer medium confocally coating the inner. For our two-medium case, the inner medium may be perfectly conducting. The two-medium solution has not yet been coded, nor a comparative TDFD run made.

In the following sections of this report, we will first document the TDFD code. Then we shall describe the canonical solutions and present code-code comparisons for those cases where comparisons have been performed.

ARCHITECTURE OF THE TIME-DOMAIN FINITE-DIFFERENCE RCS CODE

Equations to be Solved

We assume in this study that electromagnetically linear conditions prevail. Then the total field can be separated into an incident field (which would be the field in the absence of the scatterer) and a scattered field (the field modification caused by the scatterer's presence):

$$(\underline{E}^T, \underline{H}^T) = (\underline{E}^{inc}, \underline{H}^{inc}) + (\underline{E}^{scat}, \underline{H}^{scat}) \quad (1)$$

Under the linearity assumption, both the incident and the scattered fields individually satisfy Maxwell's equations.

If some background dissipation (σ_b, σ_b^*) is present, the incident fields will obey

$$\nabla \times \underline{E}^{inc} = -\mu_0 \frac{\partial \underline{H}^{inc}}{\partial t} - \sigma_b^* \underline{H}^{inc} \quad (2)$$

$$\nabla \times \underline{H}^{inc} = \epsilon_0 \frac{\partial \underline{E}^{inc}}{\partial t} + \sigma_b \underline{E}^{inc} \quad (3)$$

In the presence of an anisotropic scatterer with frequency dependent properties, the total fields conform to

$$\nabla \times \underline{E}^T = -\underline{\mu}_\infty \cdot \frac{\partial \underline{H}^T}{\partial t} - \underline{\sigma}_0^* \cdot \underline{H}^T - \int_{-\infty}^t \underline{K}^*(t-t') \cdot \frac{\partial \underline{H}^T(t')}{\partial t'} dt' - \underline{J}_f^* \quad (4)$$

$$\nabla \times \underline{H}^T = \underline{\epsilon}_\infty \cdot \frac{\partial \underline{E}^T}{\partial t} + \underline{g}_0 \cdot \underline{E}^T + \int_{-\infty}^t \underline{K}(t-t') \cdot \frac{\partial \underline{E}^T(t')}{\partial t'} dt' + \underline{J}_f \quad (5)$$

Subtraction of the first pair of equations from the second leaves us with the version of Maxwell's equations obeyed by the scattered fields:

$$\begin{aligned} \nabla \times \underline{E}^{\text{scat}} = & - \underline{\mu}_\infty \cdot \frac{\partial \underline{H}^{\text{scat}}}{\partial t} - \underline{g}_0^* \cdot \underline{H}^{\text{scat}} - \int_{-\infty}^t \underline{K}^*(t-t') \cdot \frac{\partial \underline{H}^{\text{scat}}(t')}{\partial t'} dt' \\ & - (\underline{\mu}_\infty - \underline{I}\mu_0) \cdot \frac{\partial \underline{H}^{\text{inc}}}{\partial t} - (\underline{g}_0^* - \underline{I}\sigma_b^*) \cdot \underline{H}^{\text{inc}} - \int_{-\infty}^t \underline{K}^*(t-t') \cdot \frac{\partial \underline{H}^{\text{inc}}(t')}{\partial t'} dt' \\ & - \underline{J}_f^* \end{aligned} \quad (6)$$

$$\begin{aligned} \nabla \times \underline{H}^{\text{scat}} = & \underline{\epsilon}_\infty \cdot \frac{\partial \underline{E}^{\text{scat}}}{\partial t} + \underline{g}_0 \cdot \underline{E}^{\text{scat}} + \int_{-\infty}^t \underline{K}(t-t') \cdot \frac{\partial \underline{E}^{\text{scat}}(t')}{\partial t'} dt' \\ & + (\underline{\epsilon}_\infty - \underline{I}\epsilon_0) \cdot \frac{\partial \underline{E}^{\text{inc}}}{\partial t} + (\underline{g}_0 - \underline{I}\sigma_b) \cdot \underline{E}^{\text{inc}} + \int_{-\infty}^t \underline{K}(t-t') \cdot \frac{\partial \underline{E}^{\text{inc}}(t')}{\partial t'} dt' \\ & + \underline{J}_f \end{aligned} \quad (7)$$

It is convenient to represent the inhomogeneous parts (or incident parts) of eqs. (6) and (7) as

$$[\underline{J}^{T*}] = - [\sigma_0^*] [\underline{H}^S] + [\underline{J}_f^*] + [\nabla \times \underline{E}^{\text{scat}}] =$$

$$\begin{aligned}
& + [\mu_{\infty} - \mu_0] \dot{H}^{inc} + [\sigma_0^* - \sigma_b^*] \dot{L}^{inc} \\
& + \int_{-\infty}^t [K^*(t-t')] [\dot{H}^{inc}(t')] dt' + [J_f^*] + [\nabla \times \underline{E}^{scat}]
\end{aligned} \tag{8}$$

$$\begin{aligned}
[J^T] = & - [\sigma_0] E^S + [J_f] - [\nabla \times \underline{H}^{scat}] = \\
& + [\epsilon_{\infty} - \epsilon_0] \dot{E}^{inc} + [\sigma_0 - \sigma_b] E^{inc} \\
& + \int_{-\infty}^t [K(t-t')] [\dot{E}^{inc}(t')] dt' + [J_f] - [\nabla \times \underline{H}^{scat}]
\end{aligned} \tag{9}$$

Thus, $[H^S]$ and $[E^S]$ become

$$[H^S] = - [\tau^*] \dot{H}^{inc} - [R^*] H^{inc} - \int_{-\infty}^t [A^*(t-t')] [\dot{H}^{inc}(t')] dt' \tag{10}$$

$$[E^S] = - [\tau] \dot{E}^{inc} - [R] E^{inc} - \int_{-\infty}^t [A(t-t')] [\dot{E}^{inc}(t')] dt' \tag{11}$$

In the last pair of equations, we have defined

$$[\tau^*] = [\sigma_0^*]^{-1} [\mu_{\infty} - \mu_0] \tag{12}$$

$$[R^*] = [\sigma_0^*]^{-1} [\sigma_0^* - \sigma_b^*] \tag{13}$$

$$[A^*] = [\sigma_0^*]^{-1} [K^*] \quad (14)$$

$$[\tau] = [\sigma_0]^{-1} [\epsilon_\infty - \epsilon_0] \quad (15)$$

$$[R] = [\sigma_0]^{-1} [\sigma_0 - \sigma_b] \quad (16)$$

$$[A] = [\sigma_0]^{-1} [K] \quad (17)$$

Substituting eqs. (8) - (17) back into (6) and (7) yields

$$\underline{\mu}_\infty \cdot \frac{\partial \underline{H}^{\text{scat}}}{\partial t} + \underline{\sigma}_0^* \cdot \underline{H}^{\text{scat}} + \int_{-\infty}^t \underline{K}^*(t-t') \cdot \frac{\partial \underline{H}^{\text{scat}}(t')}{\partial t'} dt' = - \underline{J}^{T*} \quad (18)$$

$$\underline{\epsilon}_\infty \cdot \frac{\partial \underline{E}^{\text{scat}}}{\partial t} + \underline{\sigma}_0 \cdot \underline{E}^{\text{scat}} + \int_{-\infty}^t \underline{K}(t-t') \cdot \frac{\partial \underline{E}^{\text{scat}}(t')}{\partial t'} dt' = - \underline{J}^T \quad (19)$$

These are the scattered field equations we will be treating.

Method of Solution

For now, we shall only concern ourselves with the 2D TM case. Thus, E_x , E_y and H_z will be present. Equation (18) reduces to a scalar equation, but (19) remains a two-component vector equation.

Figure 1 illustrates a typical TDFD 2D unit cell, and shows where the three field components associated with that cell are located.

In Appendix 1, we will derive a technique for solving this equation system using first-order exponential differencing. The result of this appendix is that, if we omit frequency dependence, $H_z(I,J)$ is advanced according to

$$H_z(I,J)^{n+1} = e^{-\mu_\infty^{-1} \sigma_0^* \Delta t} H_z(I,J)^n - (1 - e^{-\mu_\infty^{-1} \sigma_0^* \Delta t}) (\sigma_0^*)^{-1} J_z^T(I,J)^{n+1/2} \quad (20)$$

and $[E(I,J)]$ is advanced according to

$$\begin{aligned} [E(I,J)]^{n+1/2} &= e^{-[\epsilon_\infty]^{-1} [\sigma_0] \Delta t} [E(I,J)]^{n-1/2} \\ &\quad - ([I] - e^{-[\epsilon_\infty]^{-1} [\sigma_0] \Delta t}) [\sigma_0]^{-1} [J^T(I,J)]^n \end{aligned} \quad (21)$$

(The complication of frequency dependence will be considered later.)

As we have said, $[\sigma_0]$ is permitted to be anisotropic. In the actual code, it is represented by a total of five arrays:

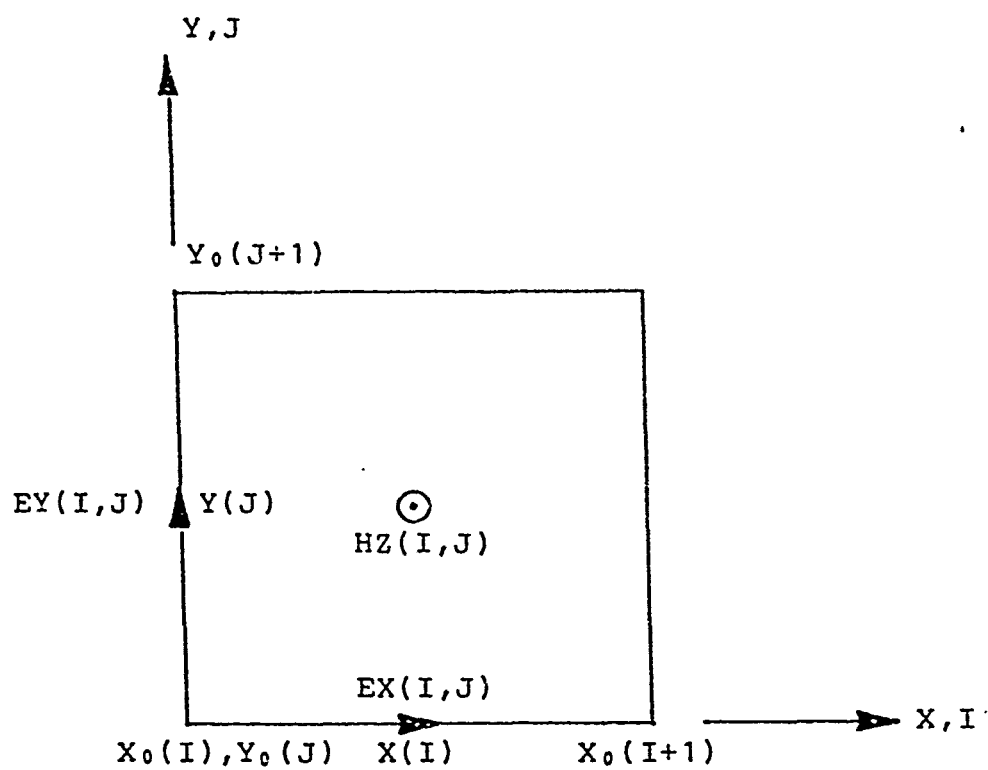


Figure 1. Location of field components in a unit cell.

SGX(I,J) is the bulk value characterizing the xx component of the conductivity tensor at cell (I,J)

SGY(I,J) is the bulk value characterizing the yy component of the conductivity tensor at cell (I,J)

SGXY(I,J) is the bulk value characterizing the xy and yx components of the conductivity tensor at cell (I,J) (gyrotropic materials are not permitted in the present code)

SGCX(I,J) is the surface conductivity in the x direction on the y-facing surface of cell (I,J)

SGCY(I,J) is the surface conductivity in the y direction of the x-facing surface of cell (I,J)

Thus, the actual conductivity seen by E_x at cell (I,J) is given by

$$\sigma_0(I,J)_{xx} = (SGX(I,J-1) + SGX(I,J))/2 + SGCX(I,J) \quad (22)$$

$$\sigma_0(I,J)_{xy} = (SGXY(I,J-1) + SGXY(I,J))/2 \quad (23)$$

$$\sigma_0(I,J)_{yx} = (SGXY(I,J-1)^{-1} + SGXY(I,J)^{-1})^{-1} \cdot 2 \quad (24)$$

$$\sigma_0(I,J)_{yy} = (SGY(I,J-1)^{-1} + SGY(I,J)^{-1})^{-1} \cdot 2 \quad (25)$$

This arrangement occurs because J_x sees the xx and xy conductivities in parallel, while J_y sees the yx and yy conductivities in series.

The conductivity matrix for E_y at cell (I,J) is analogously described

$$\sigma_0(I,J)_{xx} = (SGX(I-1,J)^{-1} + SGX(I,J)^{-1})^{-1} \cdot 2 \quad (26)$$

$$\sigma_0(I,J)_{xy} = (SGXY(I-1,J)^{-1} + SGXY(I,J)^{-1})^{-1} \cdot 2 \quad (27)$$

$$\sigma_0(I,J)_{yx} = (SGXY(I-1,J) + SGXY(I,J))/2 \quad (28)$$

$$\sigma_0(I,J)_{yy} = (SGY(I-1,J) + SGY(I,J))/2 + SGCY(I,J) \quad (29)$$

Note that, although the physical conductivity tensor is symmetric at each cell ($SGXY(I,J) = SGYX(I,J)$), the mathematical conductivity just described is not symmetric ($\sigma_0(I,J)_{xy} \neq \sigma_0(I,J)_{yx}$).

The dielectric properties of the scatterer are represented by five analogous arrays, EFX, EPY, EPXY, EPCX and EPCY. These are combined in the same way to form the mathematical permittivities $\epsilon_{\omega}(I,J)_{ij}$ at the E_x and E_y evaluation points of cell (I,J).

Due to the anisotropic cross-terms, it is necessary to know E_y at the E_x evaluation points. This is done by simple linear interpolation,

$$EY(I,J)_x = (EY(I,J) + EY(I+1,J) + EY(I,J-1) + EY(I+1,J-1))/4 \quad (30)$$

E_x at the E_y evaluation points, $EX(I,J)_y$ is obtained the same way. The matrix difference equation (21) is then solved twice at each cell and each time step, once centered at and to advance $EX(I,J)$, and once centered at and to advance $EY(I,J)$.

The following notation is also used:

QXX(I,J) is the (1, 1) component of $e^{-[\epsilon_\infty]^{-1}[\sigma_0]\Delta t}$ evaluated at the E_x points

QXY(I,J) is the (1, 2) component of $e^{-[\epsilon_\infty]^{-1}[\sigma_0]\Delta t}$ evaluated at the E_x points

QYX(I,J) is the (2, 1) component of $e^{-[\epsilon_\infty]^{-1}[\sigma_0]\Delta t}$ evaluated at the E_y points

QYY(I,J) is the (2, 2) component of $e^{-[\epsilon_\infty]^{-1}[\sigma_0]\Delta t}$ evaluated at the E_y points

SXX(I,J), SXY(I,J), SYX(I,J) and SYY(I,J) are $([I] - e^{-[\epsilon_\infty]^{-1}[\sigma_0]\Delta t})[\sigma_0]^{-1}$ correspondingly located and defined.

Additionally, if we refer back to eqs. (15) - (17),

TAUXX(I,J), TAUXY(I,J), TAUYX(I,J) and TAUYY(I,J) are $[\sigma_0]^{-1}[\epsilon_\infty - \epsilon_0]$ analogously located and defined, and

RXX(I,J), RXY(I,J), RYX(I,J) and RYY(I,J) are $[\sigma_0]^{-1}[\sigma_a - \sigma_b]$ analogously located and defined.

It is necessary to evaluate both components of $[E^S]$ as given in eq. (11) at both E_x and E_y points in each cell. The above conventions indicate how to combine the σ_0 and ϵ_∞ tensors for an inhomogeneous scatterer so this complete set of evaluations may be achieved. In particular, we denote E_{xy}^S as E_y^S evaluated at the E_x mesh point and E_{yx}^S as E_x^S evaluated at the E_y mesh point.

Thus, $E_{xx}^S(I,J)$ is, from eq. (11) with frequency dependence not yet included,

$$\begin{aligned} E_{xx}^S(I,J) = & - \text{TAUXX}(I,J) E_{xx}^{\text{inc}}(I,J) - \text{TAUXY}(I,J) E_{xy}^{\text{inc}}(I,J) \\ & - \text{RXX}(I,J) E_{xx}^{\text{inc}}(I,J) - \text{RXY}(I,J) E_{xy}^{\text{inc}}(I,J) \end{aligned} \quad (31)$$

where $E_{xx}^{\text{inc}}(I,J)$ is the analytically specified E_x^{inc} field evaluated at E_x mesh points, and $E_{xy}^{\text{inc}}(I,J)$ is the analytically specified E_y^{inc} field evaluated at E_x mesh points. Additionally, $E_{yy}^S(I,J)$ is

$$\begin{aligned} E_{yy}^S(I,J) = & - \text{TAUYY}(I,J) E_{yy}^{\text{inc}}(I,J) - \text{TAUYX}(I,J) E_{yx}^{\text{inc}}(I,J) \\ & - \text{RYY}(I,J) E_{yy}^{\text{inc}}(I,J) - \text{RYX}(I,J) E_{yx}^{\text{inc}}(I,J) \end{aligned} \quad (32)$$

where $E_{yy}^{\text{inc}}(I,J)$ is the analytically specified E_y^{inc} field evaluated at the E_y mesh points and $E_{yx}^{\text{inc}}(I,J)$ is the analytically specified E_x^{inc} field evaluated at the E_x mesh points. Finally, $E_{xy}^S(I,J)$ and $E_{yx}^S(I,J)$ are, in analogy with eq. (30),

$$E_{xy}^S(I,J) = (E_{yy}^S(I,J) + E_{yy}^S(I+1,J) + E_{yy}^S(I,J-1) + E_{yy}^S(I+1,J-1))/4 \quad (33)$$

$$E_{yx}^S(I,J) = (E_{xx}^S(I,J) + E_{xx}^S(I,J+1) + E_{xx}^S(I-1,J) + E_{xx}^S(I-1,J+1))/4 \quad (34)$$

It is also necessary to evaluate both components of $[J^T]$ as given in eq. (9) at both E_x and E_y points in each cell. Using the same convention as

above, we let J_{xy}^T be J_y^T evaluated at the E_x points and J_{yx}^T be J_x^T evaluated at the E_y points. Then equation (21), where $[J^T]$ is actually required, uses $[J^T]$ in the form

$$[\sigma_0]^{-1}[J^T] = -[E^S] + [\sigma_0]^{-1}[J_f] - [\sigma_0]^{-1}[\nabla \times H^{scat}] \quad (35)$$

We have already described how to find the $[E^S]$ contribution to $[J^T]$. It is easy to evaluate $[\sigma_0]^{-1}[J_f]$ because J_f is a prescribed analytic forcing term which can readily be evaluated at either the E_x or the E_y points. The troublesome term is $[\nabla \times H^{scat}]$. This will have both an x and a y component, each of which must be evaluated at the E_x and the E_y points.

Let us designate $(\nabla \times H^{scat})_{xx}$ as the x-component of this term evaluated at the E_x points:

$$(\nabla \times H^{scat})_{xx} = \frac{HZ(I,J) - HZ(I,J-1)}{Y(J) - Y(J-1)} \quad (36)$$

The y-component evaluated at an E_x point is

$$\begin{aligned} (\nabla \times H^{scat})_{xy} = & \\ & - \frac{1}{2} \left[\frac{(HZ(I+1,J) + HZ(I+1,J-1)) - (HZ(I,J) + HZ(I,J-1))}{2(X(I+1) - X(I))} \right. \\ & \left. + \frac{(HZ(I,J) + HZ(I,J-1)) - (HZ(I-1,J) + HZ(I-1,J-1))}{2(X(I) - X(I-1))} \right] \end{aligned} \quad (37)$$

The y component evaluated at an E_y point is

$$(\nabla \times H^{scat})_{yy} = - \frac{HZ(I,J) - HZ(I-1,J)}{X(I) - X(I-1)} \quad (38)$$

and the x component evaluated at an E_y point is

$$\begin{aligned}
 (\nabla \times \underline{H}^{\text{scat}})_{yx} = & \\
 & \frac{1}{2} \left[\frac{(\text{HZ}(\text{I}, \text{J}+1) + \text{HZ}(\text{I}-1, \text{J}+1)) - (\text{HZ}(\text{I}, \text{J}) + \text{HZ}(\text{I}-1, \text{J}))}{2(\text{Y}(\text{J}+1) - \text{Y}(\text{J}))} \right. \\
 & \left. + \frac{(\text{HZ}(\text{I}, \text{J}) + \text{HZ}(\text{I}-1, \text{J})) - (\text{HZ}(\text{I}, \text{J}-1) + \text{HZ}(\text{I}-1, \text{J}-1))}{2(\text{Y}(\text{J}) - \text{Y}(\text{J}-1))} \right] \quad (39)
 \end{aligned}$$

Consequently, for example, eq. (21) for advancing $\text{EX}(\text{I}, \text{J})$ in all its glory, becomes

$$\begin{aligned}
 \text{EX}(\text{I}, \text{J})^{n+1/2} = & \text{QXX}(\text{I}, \text{J})\text{EX}(\text{I}, \text{J})^{n-1/2} + \text{QXY}(\text{I}, \text{J})\text{EY}(\text{I}, \text{J})_x^{n-1/2} \\
 & + (1 - \text{QXX}(\text{I}, \text{J}))\text{E}_{xx}^S(\text{I}, \text{J})^n - \text{QXY}(\text{I}, \text{J})\text{E}_{xy}^S(\text{I}, \text{J})^n \\
 & - \text{SXX}(\text{I}, \text{J})(\text{J}_f(\text{I}, \text{J})_{xx}^n - (\nabla \times \underline{H}^{\text{scat}})_{xx}^n) \\
 & - \text{SXY}(\text{I}, \text{J})(\text{J}_f(\text{I}, \text{J})_{xy}^n - (\nabla \times \underline{H}^{\text{scat}})_{xy}^n) \quad (40)
 \end{aligned}$$

where QXX and QXY are defined after eq. (30), $\text{EY}(\text{I}, \text{J})_x$ is defined by eq. (30), $\text{E}_{xx}^S(\text{I}, \text{J})$ is defined by eq. (31), $\text{E}_{xy}^S(\text{I}, \text{J})$ is defined by eq. (33), SXX and SXY are defined after eq. (30), $\text{J}_f(\text{I}, \text{J})_{xx}$ and $\text{J}_f(\text{I}, \text{J})_{xy}$ are the forcing currents, $(\nabla \times \underline{H}^{\text{scat}})_{xx}$ is defined by eq. (36), and $(\nabla \times \underline{H}^{\text{scat}})_{xy}$ is defined by eq. (37).

The scalar equations for advancing $H_z(I,J)$, eq. (20), is much easier to implement than the matrix equation for advancing $[E(I,J)]$. We now need to define

$XMUZ(I,J)$ as the bulk permeability at cell (I,J) , μ_∞ of eq. (4),

$SGMZ(I,J)$ as the bulk magnetic conductivity at cell (I,J) , σ_0^* of eq. (4),

$$QMZZ(I,J) = e^{-XMUZ(I,J)} \cdot SGMZ(I,J) \cdot \Delta t \quad (41)$$

$$SMZZ(I,J) = (1 - QMZZ(I,J))/SGMZ(I,J) \quad (42)$$

$$TAUMZZ(I,J) = \sigma_0^{*-1} (\mu_\infty - \mu_0) \quad (43)$$

evaluated at the center of cell (I,J) , and

$$RMZZ(I,J) = \sigma_0^{*-1} (\sigma_0^* - \sigma_b^*) \quad (44)$$

also evaluated at the center of cell (I,J)

The murderously complicated interpolations involved in advancing E do not occur in advancing H_z partly because H_z is the only component of H present, and partly because H_z is evaluated at the center, not on an edge of the cell.

From eq (10), $H_{zz}^S(I,J)$ is then, with frequency dependence still not included,

$$H_{zz}^S(I,J) = -TAUMZZ(I,J)H_{zz}^{inc}(I,J) - RMZZ(I,J)H_{zz}^{inc}(I,J) \quad (45)$$

where $H_{zz}^{inc}(I,J)$ is the analytically specified H_z^{inc} field evaluated at the cell centers.

One also need only evaluate $J_z^{*T}(I,J)$ of eq. (8) at the cell centers. Equation (20), where $J_z^{*T}(I,J)$ actually appears, uses the form

$$\begin{aligned}
(\sigma_0^*)^{-1} J_z^{*T}(I,J) = & - H_{zz}^S(I,J) + (\sigma_0^*)^{-1} J_f^*(I,J)_{zz} \\
& + (\sigma_0^*)^{-1} (\nabla \times \underline{E}^{scat})_{zz}
\end{aligned} \tag{46}$$

Here, we already have found $H_{zz}^S(I,J)$, $J_f^*(I,J)_{zz}$ is a prescribed magnetic current density (which would be zero on any physically real problem), and $(\nabla \times \underline{E}^{scat})_{zz}$ is just

$$(\nabla \times \underline{E}^{scat})_{zz} = \frac{EY(I+1,J) - EY(I,J)}{X_0(I+1) - X_0(I)} - \frac{EX(I,J+1) - EX(I,J)}{Y_0(J+1) - Y_0(J)} \tag{47}$$

Thus, eq. (20) for advancing $HZ(I,J)$ becomes

$$\begin{aligned}
HZ(I,J)^{n+1} = & QMZZ(I,J)HZ(I,J)^n + (1 - QMZZ(I,J))H_{zz}^S(I,J)^{n+1/2} \\
& - SMZZ(I,J)(J_f^*(I,J)_{zz})^{n+1/2} + (\nabla \times \underline{E}^{scat})_{zz}^{n+1/2}
\end{aligned} \tag{48}$$

Introduction of Frequency Dependence

Let us assume the frequency-dependent term in eq. (19) has a kernel of the form

$$\underline{\kappa}(\mu) = \sum_{m=1}^M \underline{a}_m e^{-\beta_m \mu} \quad (49)$$

where \underline{a}_m has the units of conductivity. This assumption is equivalent to expanding the frequency-dependence of the material's electrical properties in a Prony series under the constraint that all the poles be on the real axis. (Appendix 1 indicates how one may relax the real-poles-only constraint.)

Equation (19) then becomes

$$\underline{\epsilon}_\infty \cdot \frac{\partial \underline{E}^{\text{scat}}}{\partial t} + \underline{\sigma}_0 \cdot \underline{E}^{\text{scat}} + \sum_{m=1}^M \underline{a}_m \cdot \underline{J}_m^{\text{scat}} = - \underline{J}^T \quad (50)$$

where

$$\underline{J}_m^{\text{scat}}(t) = e^{-\beta_m t} \int_{-\infty}^t \frac{\partial \underline{E}^{\text{scat}}(t')}{\partial t'} e^{\beta_m t'} dt' \quad (51)$$

In eq. (50), \underline{J}^T is still given by eq. (35), but with the understanding that \underline{E}^S has the frequency-dependent term restored. In other words, \underline{E}^S is now represented by eq. (11), not eqs. (31) and (32).

The $\underline{J}_m^{\text{scat}}$ of eq. (50) are not clearly identifiable either as conduction or as displacement currents. We shall coin the name "Prony currents" for them. Equation (50) for $\underline{J}_m^{\text{scat}}(t)$ is much easier to recognize if we differentiate it once; its homogeneous solution is just a decaying exponential:

$$\frac{\partial \underline{J}_m^{\text{scat}}}{\partial t} + \beta_m \underline{J}_m^{\text{scat}} = \frac{\partial \underline{E}^{\text{scat}}}{\partial t} \quad (52)$$

In the 2D TM case, the components of eqs. (50) and (52) then comprise $2(M+1)$ coupled first-order differential equations for $\underline{E}^{\text{scat}}$ and $\underline{J}_m^{\text{scat}}$. Ideally, these equations should all be advanced from $(n-1/2)\Delta t$ to $(n+1/2)\Delta t$ simultaneously each cycle. A technique for doing this is also described in Appendix 1.

However, the present code actually implements a slightly less accurate algorithm where $\underline{E}^{\text{scat}}$ alone is advanced first in each cycle, and then the $\underline{J}_m^{\text{scat}}$ are advanced separately. Finally, a correction is made to the advanced $\underline{E}^{\text{scat}}$ to account for the effects of the $\underline{J}_m^{\text{scat}}$.

At this point, it is most instructive to go back to eq. (7) and perform a rearrangement:

$$\begin{aligned} \nabla \times \underline{H}^{\text{scat}} = & \underline{\epsilon}_\infty \cdot \frac{\partial \underline{E}^{\text{scat}}}{\partial t} + \underline{\sigma}_0 \cdot \underline{E}^{\text{scat}} + (\underline{\epsilon}_\infty - \underline{I}\epsilon_0) \cdot \frac{\partial \underline{E}^{\text{inc}}}{\partial t} \\ & + (\underline{\sigma}_0 - \underline{I}\sigma_b) \cdot \underline{E}^{\text{inc}} + \int_{-\infty}^t \underline{E}(t-t') \cdot \frac{\partial \underline{E}^T(t')}{\partial t'} + \underline{J}_f \end{aligned} \quad (53)$$

The inhomogeneous part of this equation can be written

$$[\underline{J}^T] + [\underline{J}^P] = -[\sigma_0][\underline{E}^S] + [\underline{J}^P] + [\underline{J}_f] - [\nabla \times \underline{H}^{\text{scat}}] + [\underline{J}^P] \quad (54)$$

where $[\underline{E}^S]$ and $[\underline{J}^P]$ are

$$[\underline{E}^S] = -[\tau][\dot{\underline{E}}^{\text{inc}}] - [R][\underline{E}^{\text{inc}}] \quad (55)$$

$$[J^P] = \int_{-\infty}^t [K(t-t')] [\dot{E}^T(t')] dt' \quad (56)$$

with $[r]$ and $[R]$ still respectively given by eqs. (15) and (16).

Substituting eqs. (54) - (56) back into (53) then results in

$$\underline{\epsilon}_{\infty} \cdot \frac{\partial \underline{E}^{scat}}{\partial t} + \underline{\sigma}_0 \cdot \underline{E}^{scat} = - \underline{J}^T - \underline{J}^P \quad (57)$$

This equation is just (19) with the frequency-dependent term transferred to the right and represented as \underline{J}^P . It is advanced according to eq. (21):

$$\begin{aligned} [E(I,J)]^{n+1/2} &= e^{-[\epsilon_{\infty}]^{-1}[\sigma_0]\Delta t} [E(I,J)]^{n-1/2} \\ &- ([I] - e^{-[\epsilon_{\infty}]^{-1}[\sigma_0]\Delta t}) [\sigma_0]^{-1} [J^T(I,J) + J^P(I,J)]^n \quad (58) \end{aligned}$$

The problem with direct application of this procedure is that we do not know the portion of \underline{J}^P associated with \dot{E}^{scat} at $n\Delta t$ until we have advanced the Prony currents, and we cannot, strictly speaking, do that until we have advanced \underline{E}^{scat} .

As mentioned previously, the code does not presently utilize the procedure described in Appendix 1 for simultaneous advancement of \underline{E}^{scat} and \underline{J}_m^{scat} . Rather, we first find an intermediate value of \underline{E}^{scat} obtained with effects of the Prony currents omitted:

$$[E(I,J)]^{int} = e^{-[\epsilon_{\infty}]^{-1}[\sigma_0]\Delta t} [E(I,J)]^{n-1/2}$$

$$= ([I] - e^{-[\epsilon_\omega]^{-1}[\sigma_0]\Delta t})[\sigma_0]^{-1}[J^T(I, J)]^n \quad (59)$$

The procedure for obtaining this intermediate value is identical to the procedure described in the previous section for advancement through a total cycle in the absence of frequency-dependent effects. Its implementation in the code is also identical to what was described in the previous section.

Let us next turn to the advancement of the total Prony current \underline{J}^P as given by eqs. (49) and (56):

$$\underline{J}^P = \sum_{m=1}^M \underline{a}_m \cdot \underline{J}_m^T \quad (60)$$

where

$$\underline{J}_m^T(t) = e^{-\beta_m t} \int_{-\infty}^t \frac{\partial \underline{E}^T(t')}{\partial t'} e^{\beta_m t'} dt' \quad (61)$$

Equation (61), like (51), is made more recognizable by differentiating with respect to time:

$$\frac{\partial \underline{J}_m^T}{\partial t} + \beta_m \underline{J}_m^T = \frac{\partial \underline{E}^T}{\partial t} = \frac{\partial (\underline{E}^{\text{inc}} + \underline{E}^{\text{scat}})}{\partial t} \quad (62)$$

The equation for exponential-difference advancement of this result is

$$\underline{J}_m^T(I, J)^{n+1/2} = e^{-\beta_m \Delta t} \underline{J}_m^T(\tau, J)^{n-1/2}$$

$$+ (1 - e^{-\beta_m \Delta t}) (\underline{E}^{inc}(I,J) + \underline{E}^{scat}(I,J))^n / \beta_m \quad (63)$$

The incident field \underline{E}^{inc} is a specified analytic function. At present, the code evaluates $\underline{E}^{scat}(I,J)^n$ as

$$\underline{E}^{scat}(I,J)^n = \frac{\underline{E}(I,J)^{int} - \underline{E}(I,J)^{n-1/2}}{\Delta t} \quad (64)$$

Equations (63) and (64) may be combined to give an expression for $\underline{J}_m^T(I,J)^{n+1/2}$ in terms of known quantities. We can then determine $\underline{J}^P(I,J)^n$ as

$$\underline{J}^P(I,J)^n = \sum_{m=1}^M [a_m(I,J)] [\underline{J}_m^T(I,J)^{n+1/2} + \underline{J}_m^T(I,J)^{n-1/2}] / 2 \quad (65)$$

Subtraction of eq. (59) from eq. (58) then permits us to advance $[E(I,J)]$ from its intermediate value to its value at the new time step, $(n+1/2)\Delta t$:

$$\begin{aligned} [E(I,J)]^{n+1/2} &= [E(I,J)]^{int} \\ &- ([I] - e^{-[\epsilon_\infty]^{-1}[\sigma_0]\Delta t}) [\sigma_0]^{-1} [\underline{J}^P(I,J)]^n \end{aligned} \quad (66)$$

Frequency dependence in the magnetic properties of the material can be treated in an exactly dual manner to what we have just described for the electrical properties.

At present, we have not coded up magnetic frequency dependence, nor have we combined frequency dependence with off-diagonal type anisotropy. Both these generalizations would be perfectly obvious extensions of what has been done, but we cannot conceive a canonical problem we could check the results against.

Not mixing off-diagonal anisotropy and frequency dependence means we only treat diagonal \underline{a}_m tensors. If eq. (65) is substituted in eq. (66), we obtain

$$[E(I,J)]^{n+1/2} = [E(I,J)]^{int} - ([I] - e^{-[\epsilon_\infty]^{-1}[\sigma_0]\Delta t}) \cdot \sum_{m=1}^M [SA_m(I,J)] [J_m^T(I,J)^{n+1/2} + J_m^T(I,J)^{n-1/2}] \quad (67)$$

where

$$[SA_m(I,J)] = [\sigma_0(I,J)]^{-1} [A_m(I,J)] \quad (68)$$

In the actual code, two arrays are used to describe the material effects of each term in the Prony series. Let $\sigma_0(I,J)_{xx}^{-1}$ represent the xx element of the inverse of the matrix described by eqs. (22) - (25) at cell (I,J). Let $\sigma_0(I,J)_{yy}^{-1}$ similarly represent the yy element of the inverse of the matrix described by eqs. (26) - (29) at cell (I,J).

Moreover, let AAMX(I,J) represent the xx element of the mth Prony tensor of the bulk material at cell (I,J), and let AAMY(I,J) represent the corresponding yy element. Then the xx element of $[SA_m(I,J)]$ which actually relates the x component of $\underline{J}_m^T(I,J)$ to the x component of $\underline{E}(I,J)$ is called

$$SAMX(I,J) = \sigma_0(I,J)_{xx}^{-1} (AAMX(I,J-1) + AAMX(I,J))/2 \quad (69)$$

Similarly, the yy element of $[SA_m(I,J)]$ which actually relates the y component $J_m^T(I,J)$ to the y component of $\underline{E}(I,J)$ is called

$$SAMY(I,J) = \sigma_0(I,J)_{yy}^{-1} (AAMY(I-1,J) + AAMY(I,J))/2 \quad (70)$$

In keeping with our simplification of not mixing off-diagonal anisotropy with frequency dependence, we ignore any possible off-diagonal nonzero values in $[SA_m(I,J)]$.

It turns out that only $SAMX(I,J)$ and $SAMY(I,J)$ need actually be stored. That is, it is not necessary to assign arrays for keeping $\sigma_0(I,J)_{xx}^{-1}$, $\sigma_0(I,J)_{yy}^{-1}$, $AAMX(I,J)$ and $AAMY(I,J)$.

Consequently, the actual equation used in the code for implementing the x-component of the Prony correction is

$$EX(I,J)^{n+1/2} = EX(I,J)^{int} - (1 - QXX(I,J)) \sum_{m=1}^M SAMX(I,J) XJMSX(I,J)^n \quad (71)$$

where

$$XJMX(I,J)^n = [J_m^T(I,J)_x^{n+1/2} + J_m^T(I,J)_x^{n-1/2}]/2 \quad (72)$$

Similarly, the actual equation used for implementing the y-component of the Prony correction is

$$\begin{aligned}
 EY(I,J)^{n+1/2} &= EY(I,J)^{int} \\
 &- (1 - QYV(I,J)) \sum_{m=1}^M SAMY(I,J) XJMY(I,J)^n
 \end{aligned} \tag{73}$$

where

$$XJMY(I,J)^n = [J_m^T(I,J)_y^{n+1/2} + J_m^T(I,J)_y^{n-1/2}] / 2 \tag{74}$$

Transformation from the Near-field Time Domain to the Far-field Frequency Domain

The foregoing work described the determination of the scatterer's electromagnetic response and associated near fields. We are actually interested in the RCS, which is a far-field quantity. Now we shall describe how the code extracts the RCS from the near-field results. In this process, we also transform from time domain to frequency domain.

Any electromagnetic field can be expressed in terms of an electric and a magnetic vector potential, \underline{A} and \underline{A}^* . These vector potentials (in the frequency domain) obey the inhomogeneous wave equations.

$$\nabla^2 \underline{A} + k^2 \underline{A} = -\mu_0 \underline{J} \quad (75)$$

$$\nabla^2 \underline{A}^* + k^2 \underline{A}^* = \epsilon_0 \underline{J}^* \quad (76)$$

Here \underline{J}^* is the fictitious magnetic current density often found useful in manipulating Maxwell's equations. Equations (75) and (76) can be generalized to apply to any linear medium, although we shall find their free-space form adequate for our uses.

In 2D, we define the far field to be the region where all fields drop off as $r^{-1/2}$; i.e., where all the faster falling terms have vanished. We can then separate the electric and magnetic fields into two parts,

$$\underline{E} = \underline{E}_e + \underline{E}_m \quad (77)$$

$$\underline{H} = \underline{H}_e + \underline{H}_m \quad (78)$$

The e-subscripted parts are associated with the electric vector potential \underline{A} , and the m-subscripted parts are associated with the magnetic vector potential \underline{A}^* . In particular, if we call Y_0 and Z_0 the admittance and impedance of free space, we can show in the far field that

$$\underline{H}_e = \nabla \times \underline{A} / \mu_0 = i\omega Y_0 \underline{i}_r \times \underline{A} \quad (79)$$

$$\underline{E}_m = \nabla \times \underline{A}^* / \epsilon_0 = i\omega Z_0 \underline{i}_r \times \underline{A}^* \quad (80)$$

$$\underline{E}_e = i\omega \underline{A}_t = i\omega(\underline{i}_\phi A_\phi + \underline{i}_z A_z) \quad (81)$$

$$\underline{H}_m = -i\omega \underline{A}_t^* = -i\omega(\underline{i}_\phi A_\phi^* + \underline{i}_z A_z^*) \quad (82)$$

Here, a t subscript indicates that only the transverse components (ϕ and z) are retained. Equations (79) - (82) are analogous to 3D formulas, and depend on the fact that

$$\frac{e^{i(kr-\omega t)}}{\sqrt{r}} \quad (83)$$

is a valid far-field frequency-domain 2D solution of the wave equation even if the more general

$$\frac{f(t - r/c)}{\sqrt{r}} \quad (84)$$

is not a valid time-domain solution. These equations tell us that if we can evaluate \underline{A} and \underline{A}^* , we can find the 2D RCS without undue complication.

In two dimensions, the Green's function for the scalar wave equation in the frequency domain obeys

$$\nabla^2 G(\underline{r}|\underline{r}') + k^2 G(\underline{r}|\underline{r}') = \delta(\underline{r}-\underline{r}') \quad (85)$$

where \underline{r} is the scatterer location and \underline{r}' is the observer location. This equation has solution, with $R = |\underline{r}' - \underline{r}|$,

$$G(\underline{r}|\underline{r}') = -\frac{i}{4} H_0^{(1)}(kR) \quad (86)$$

Thus, at least in cartesian coordinates, \underline{A} and \underline{A}^* become

$$\underline{A}(\underline{r}', \omega) = \iint \frac{i H_0^{(1)}(kR)}{4\mu_0} \underline{J}(\underline{r}, \omega) d\underline{r} \quad (87)$$

$$\underline{A}^*(\underline{r}', \omega) = - \iint \frac{i H_0^{(1)}(kR)}{4\epsilon_0} \underline{J}^*(\underline{r}, \omega) d\underline{r} \quad (88)$$

For the far field region, $G(\underline{r}|\underline{r}')$ asymptotically approaches

$$G(\underline{r}|\underline{r}') = \frac{e^{-i3\pi/4}}{4} \sqrt{\frac{2}{\pi kR}} e^{ikR} \quad (89)$$

This expression may be further manipulated by letting r' replace R in the denominator of the radical. The phase term requires a bit more care:

$$kR \rightarrow k(r' - \underline{i}' \cdot \underline{r}) = kr' - (kx \cos\phi' + ky \sin\phi') \quad (90)$$

where

$$\underline{\underline{r}}' = \underline{\underline{x}} \cos \phi' + \underline{\underline{y}} \sin \phi' \quad (91)$$

is a unit vector pointing from the target to a far-field observer.

Using these expansions, we can rewrite the formula for $\underline{\underline{A}}$ in the far field as

$$\begin{aligned} \underline{\underline{A}}(\underline{\underline{r}}', \omega) = \\ - \frac{\mu_0 e^{-3i\pi/4}}{4} \sqrt{\frac{2}{\pi k r'}} e^{ikr'} \iint \underline{\underline{J}}(\underline{\underline{r}}, \omega) e^{-ik(\underline{\underline{x}} \cos \phi' + \underline{\underline{y}} \sin \phi')} d\underline{\underline{r}} \end{aligned} \quad (92)$$

A corresponding expression exists for $\underline{\underline{A}}^*(\underline{\underline{r}}', \omega)$. The far-field expression for $\underline{\underline{E}}_e$ then becomes

$$\begin{aligned} \underline{\underline{E}}_e(\underline{\underline{r}}', \omega) = i\omega \underline{\underline{A}}_t(\underline{\underline{r}}', \omega) = \\ - \frac{i\omega\mu_0 e^{-3i\pi/4}}{4} \sqrt{\frac{2}{\pi k r'}} e^{ikr'} \iint \underline{\underline{J}}_t(\underline{\underline{r}}, \omega) e^{-ik(\underline{\underline{x}} \cos \phi' + \underline{\underline{y}} \sin \phi')} d\underline{\underline{r}} \end{aligned} \quad (93)$$

Similarly, $\underline{\underline{H}}_m$ becomes

$$\underline{\underline{H}}_m(\underline{\underline{r}}', \omega) = i\omega \underline{\underline{A}}_t^*(\underline{\underline{r}}', \omega) =$$

$$\frac{i\omega\epsilon_0 e^{-3i\pi/4}}{4} \sqrt{\frac{2}{\pi k r'}} e^{ikr'} \iint \underline{J}_t^*(\underline{r}, \omega) e^{-ik(x \cos\phi' + y \sin\phi')} d\underline{r} \quad (94)$$

Analogous formulas exist for \underline{E}_m and \underline{H}_e .

Equations (93) and (94) are not directly applicable to the output of our 2D Maxwell solver as these equations demand the frequency-domain \underline{J} and \underline{J}^* , while the Maxwell solver outputs the time-domain currents.

Let us say we want $\underline{E}_e(\underline{r}'_p, \omega_q)$ where \underline{r}'_p points in one of N_p discrete angles of interest and ω_q is one of N_q discrete frequencies of interest. We can then write

$$\underline{E}_e(\underline{r}'_p, \omega_q) = - \frac{i\omega_q \mu_0 e^{-3i\pi/4}}{8\pi} \sqrt{\frac{2}{\pi k_q r'_p}} e^{ik_q r'_p} \int_{-\infty}^{\infty} e^{j\omega_q t} dt \iint \underline{J}_t(\underline{r}, t) e^{i\mathbf{k}'_{pq} \cdot \underline{r}} d\underline{r} \quad (95)$$

where \mathbf{k}'_{pq} is the wavenumber pointing towards the observer at location \underline{r}'_p and frequency ω_q , and where we have interchanged the order of time and space integration after replacing $\underline{J}_t(\underline{r}, \omega)$ with its inverse Fourier representation.

Analogously, $\underline{H}_m(\underline{r}'_p, \omega_q)$ becomes

$$\underline{H}_m(\underline{r}'_p, \omega_q) = \frac{i\omega_q \epsilon_0 e^{-3i\pi/4}}{8\pi} \sqrt{\frac{2}{\pi k'_q r'_p}} e^{ik_q r'_p} \int_{-\infty}^{\infty} e^{j\omega_q t} dt \iint \underline{J}_t^*(\underline{r}, t) e^{-i\mathbf{k}'_{pq} \cdot \underline{r}} d\underline{r} \quad (96)$$

Equations (95) and (96), and the two companion equations for \underline{E}_m and \underline{H}_e are in a form which is compatible with our time-domain Maxwell solver. Taking the time integration outside the space integration is vitally important to the efficiency of our algorithm. Were this not done, $\underline{J}_t(\underline{r}, t)$ and $\underline{J}_t^*(\underline{r}, t)$ would have to be Fourier transformed at every point before being integrated over space. The form of eqs. (95) and (96) replaces this enormous computation with a single Fourier transform on the result of the space integral.

If we let $\underline{J}^{\text{scat}}$ represent the total current (conduction, displacement and Prony) associated with the scattered electromagnetic field (see eq. (53)).

$$\begin{aligned} \underline{J}^{\text{scat}} = & \underline{\epsilon}_{\infty} \cdot \frac{\partial \underline{E}^{\text{scat}}}{\partial t} + \underline{\sigma}_0 \cdot \underline{E}^{\text{scat}} + (\underline{\epsilon}_{\infty} - \underline{I}\epsilon_0) \cdot \frac{\partial \underline{E}^{\text{inc}}}{\partial t} \\ & + (\underline{\sigma}_0 - \underline{I}\sigma_b) \cdot \underline{E}^{\text{inc}} + \int_{-\infty}^t \underline{K}(t-t') \cdot \frac{\partial \underline{E}^T(t')}{\partial t'} dt' \end{aligned} \quad (97)$$

and if we substitute $\underline{J}_t^{\text{scat}}$ for \underline{J}_t in eq. (95), \underline{E}_e of eq. (95) becomes the scattered field $\underline{E}^{\text{scat}}$ of the first section unless magnetic materials are present. That is, $\underline{J}_t^{\text{scat}}$ integrated over the scatterer cross-section according to eq. (95) gives $\underline{E}^{\text{scat}}$ in the absence of magnetic materials.

$$\text{RCS}(\phi'_p, \omega_q) = 2\pi \left| \frac{\underline{E}_e^{\text{scat}}(\underline{r}'_p, \omega_q) \cdot \sqrt{\underline{r}'_p}}{\underline{E}^i(\underline{r}'_p, \omega_q)} \right|^2 \quad (98)$$

In this convention, \underline{A}^* and \underline{E}_m are zero.

However, it is possible to replace the area integral of eqs. (95) and (96) with a contour integral by means of Huygens principle. In particular,

let S be a closed contour which completely surrounds the target. For instance, let S be a rectangle defined by $x = x_1, x_2$ and $y = y_1, y_2$.

(At this point, it may be well to digress a moment and present a map of the problem space we are using. Let us refer to Figure 2. The entire problem space is described by $1 \leq I \leq NX$, $1 \leq J \leq NY$ or $X_0(1) \leq x \leq X_0(NX)$, $Y_0(1) \leq y \leq Y_0(NY)$, where NX and NY are typically around 250. The working volume actually occupied by the scatterer is $(NXB - 1)$ by $(NYB - 1)$ cells centered in the overall problem space where NXB and NYB are typically on the order of 75. Thus, the working volume is separated from the problem space boundary by $(1/2)(NX - NXB)$ cells along x and $(1/2)(NY - NYB)$ cells along y . This separation, which is on the order of 80 cells, is necessary to decouple the outer boundary from the reactive fields of the scatterer. The Huygens surface S is normally placed one cell outside the actual working volume, at $I = ILOW$ or $IHIGH$ and $J = JLOW$ or $JHIGH$. Then x_1 is $X_0(ILOW)$, etc.)

Let \underline{E}^{scat} and \underline{H}^{scat} be the scattered fields which our Maxwell solver predicts will exist on S due to the time-domain illumination. Let \underline{n} be an outward-pointing unit normal on S . If we then remove the scatterers and its currents, but let an electric surface current

$$\underline{K} = \underline{n} \times \underline{H}^{scat} \quad (99)$$

and a magnetic surface current

$$\underline{K}^* = -\underline{n} \times \underline{E}^{scat} \quad (100)$$

flow on S , the scattered electromagnetic field will be replicated outside S . This means the area integral of eq. (95) may be replaced by

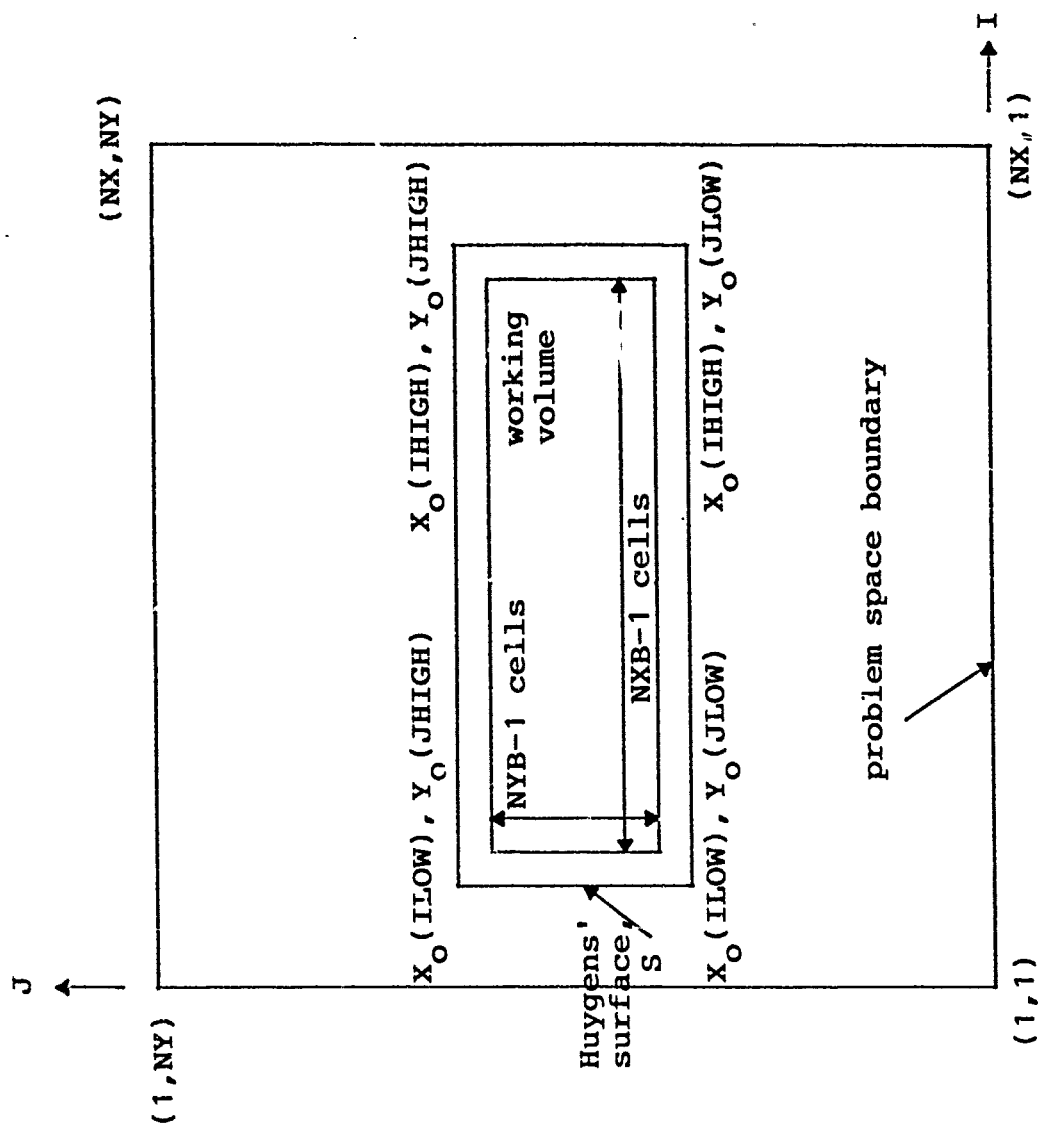


Figure 2. Map of overall problem space showing location of working volume and Huygens' surface.

$$\sum_i (\underline{n} \times \underline{H}^{\text{scat}}(\underline{r}_i, t))_t e^{-ik'_{pq} \cdot \underline{r}_i} \Delta s_i = \underline{I}_{pq}^{\text{scat}}(t)_t \quad (101)$$

where the summation over i represents integration over the finite difference cell edges which lie on S and $\underline{H}^{\text{scat}}(\underline{r}_i, t)$ is $\underline{H}^{\text{scat}}$ evaluated at the middle of Δs_i . This summation is represented by I because it has the dimension of amperes. In the actual code, it goes by the name XIEST_q if one is computing a monostatic RCS or XIESTB_p if one is computing a bistatic RCS. Figure 1 indicates that $\underline{H}_z^{\text{scat}}$ is actually evaluated at the cell centers, not on the cell edges. Thus, an interpolation is necessary to obtain $\underline{H}^{\text{scat}}(\underline{r}_i, t)$. For instance, on the $y = Y_0(\text{JLOW})$ portion of S , we have

$$(\underline{n} \times \underline{H}^{\text{scat}}(\underline{r}_i, t))_t = -\frac{1}{\phi} \sin \phi' (HZ(I, \text{JLOW}) + HZ(I, \text{JLOW} - 1))/2 \quad (102)$$

Analogously, the area integral present in eq. (96) for $\underline{H}_m(\underline{r}'_p, \omega_q)$ can be written

$$\sum_i (-\underline{n} \times \underline{E}^{\text{scat}}(\underline{r}_i, t))_t e^{-ik'_{pq} \cdot \underline{r}_i} \Delta s_i = \underline{I}_{pq}^{\text{scat}}(t)^*_t \quad (103)$$

(Remember the t subscript on \underline{I} , \underline{I}^* , or anything else implies evaluation with the r component omitted.) In the code, this variable is called XIMST_q or XIMSTB_p . Since $\underline{E}^{\text{scat}}$ is evaluated at the middle of the cell edges, no interpolation is necessary to obtain $\underline{E}^{\text{scat}}(\underline{r}_i, t)$. On the $y = Y_0(\text{JLOW})$ portion of S , the equation analogous to (102) is

$$(-\underline{n} \times \underline{E}^{\text{scat}}(\underline{r}_i, t))_t = -\frac{1}{z} EX(I, \text{JLOW}) \quad (104)$$

Equations (95) and (101) indicate the z-component of $\underline{H}^{\text{scat}}$ is associated with the ϕ' -component of $\underline{E}_e(\underline{r}, \omega_q)$. The ϕ -component of $\underline{E}^{\text{scat}}$ in eq. (103) has the same association, as the cross with \underline{i}_r in eq. (80) proves. These scattered fields are the TM solution.

Analogously, the ϕ -component of $\underline{H}^{\text{scat}}$ in eq. (101) and the z-component of $\underline{E}^{\text{scat}}$ in eq. (103) relate to the (decoupled) TE solution, which we are not treating in detail at this time.

Let us use $\underline{I}_{pq}^{\text{scat}}(t)_t^n$ to denote this "current" evaluated from the finite-difference code at $n\Delta t$. Let us analogously denote $\underline{I}_{pq}^{\text{scat}}(t)_t^{*n+1/2}$. As the finite-difference calculation progresses, we can then keep running summations of each scattering direction \underline{r}'_p and each frequency ω_q ,

$$\underline{Q}_{pq}^{\text{scat}}(t)_t^n = \sum_{m=1}^n \underline{I}_{pq}^{\text{scat}}(t)_t^m e^{j\omega_q m \Delta t} \quad (105)$$

$$\underline{Q}_{pq}^{\text{scat}}(t)_t^{*n+1/2} = \sum_{m=1}^n \underline{I}_{pq}^{\text{scat}}(t)_t^{*m+1/2} e^{j\omega_q (m+1/2) \Delta t} \quad (106)$$

When the time-domain finite difference calculation is complete, these Q's will then respectively contain quantities which are directly proportional to the electric and magnetic contribution to the RCS in direction \underline{r}'_p or at ω_q . Note that it is only necessary to back store $2(N_p + N_q)$ complex quantities during the time-domain finite-difference calculation in order to preserve all the information necessary to generate a monostatic RCS as a function of ω and a bistatic RCS as a function of scattering direction.

The symbol Q is used in eq. (105) because it represents a quantity with units of coulombs. In the code, it is written SIEST_q if one is computing a monostatic RCS or SIESTB_p if one is computing a bistatic RCS. The scattered electric field associated with $\underline{Q}_{pq}^{\text{scat}}(t)_t$ is

$$\underline{E}_e^{scat}(\underline{r}'_p, \omega_q) = - \frac{i\omega_q \mu_0 e^{-3i\pi/4}}{8\pi} \sqrt{\frac{2}{\pi k_q r'_p}} e^{ik_q r'_p} Q_{pq}^{scat}(\omega)_t^{\infty} \quad (107)$$

The code tracks the ϕ' -component of this quantity as EPES_q or EPESB_p, when $\sqrt{r'_p}$ is normalized out. Analogously, the scattered magnetic field associated with $Q_{pq}^{scat}(\omega)_t^*$ is

$$\underline{H}_m^{scat}(\underline{r}'_p, \omega_q) = \frac{i\omega_q \epsilon_0 e^{-3i\pi/4}}{8\pi} \sqrt{\frac{2}{\pi k_q r'_p}} e^{ik_q r'_p} Q_{pq}^{scat}(\omega)_t^* \quad (108)$$

In the code, the z-component of this quantity is HZMS_q or HZMSB_p when $\sqrt{r'_p}$ is normalized out. The scattered electric field associated with the magnetic current is obtained by combining eqs. (80) and (108),

$$\underline{E}_m^{scat}(\underline{r}'_p, \omega_q) = \frac{i\omega_q e^{-3i\pi/4}}{8\pi c} \sqrt{\frac{2}{\pi k_q r'_p}} e^{ik_q r'_p} \underline{i}'_{rp} \times Q_q^{scat}(\omega)^{\infty} \quad (109)$$

In the code, the ϕ' -component of this quantity, less the $\sqrt{r'_p}$ factor, is EPMS_q or EPMSB_p.

The radar cross section then becomes

$$RCS(\phi'_p, \omega_q) = 2\pi \left| \frac{(\underline{E}_e^{scat}(\underline{r}'_p, \omega_q) + \underline{E}_m^{scat}(\underline{r}'_p, \omega_q))\sqrt{r'_p}}{\underline{E}^i(\underline{r}'_p, \omega_q)} \right|^2 \quad (110)$$

In the code, SCATXE_q or SCATXEB_p is the E_e^{scat} contribution to the ratio inside the absolute value signs, and SCATXM_q or SCATXMB_p is the E_m^{scat} contributions.

CANONICAL SOLUTIONS AND CODE-CODE COMPARISONS

Scattering from a Layered Dielectric Cylinder

Let us first discuss scattering of a plane wave by a circular dielectric cylinder composed of concentric layers of different materials. Assume there are N layers, with layer i characterized by ϵ_i , μ_i , ω_i , σ_i^* and outer radius a_i . We shall here treat the TM case (\underline{H} along the cylinder axis; \underline{E} transverse), although the TM problem is nearly identical mathematically.

Assume the incident wave is at angular frequency ω_q , and is propagating in the $+y$ direction,

$$\underline{H}^{inc}(\underline{r}, t) = \underline{i}_z Y_0 e^{i(k_{0q} r \sin \phi - \omega_q t)} \quad (1)$$

$$\underline{E}^{inc}(\underline{r}, t) = -\underline{i}_x e^{i(k_{0q} r \sin \phi - \omega_q t)} \quad (2)$$

Here, $Y_0 = \frac{\epsilon_0}{\mu_0}$ is the admittance of free space. The same symbol will subsequently be used to designate Neuman functions, but context should keep the meaning unambiguous. Additionally, k_{0q} is the free space wavenumber, $\omega_q \sqrt{\epsilon_0 \mu_0} = \omega_q / c$.

Equation (1) may be expanded in cylindrical harmonics,

$$\underline{H}^{inc}(\underline{r}, \omega_q) = \underline{i}_z Y_0 \sum_{n=-\infty}^{\infty} J_n(k_{0q} r) e^{in\phi}$$

$$= Y_0 \underline{i}_z \left[J_0(k_{0q}r) + \sum_{n=2,2}^{\infty} 2J_n'(k_{0q}r) \cos n\phi + \sum_{n=1,2}^{\infty} 2iJ_n(k_{0q}r) \sin n\phi \right] \quad (3)$$

In the future, it will be useful to designate the coefficients of these harmonics as a_n^{inc} ;

$$\begin{aligned} a_0^{inc} &= 1 \\ a_n^{inc} &= 2 \quad n > 0, \text{ even} \\ a_n^{inc} &= 2i \quad n \text{ odd} \end{aligned} \quad (4)$$

Since $\nabla \times \underline{H}^{inc} = -j\omega_q \epsilon_0 \underline{E}^{inc}$, the cylindrical harmonic expansion for \underline{E}^{inc} becomes

$$\begin{aligned} \underline{E}^{inc}(\underline{r}, \omega_q) &= \frac{iY_0}{\omega_q \epsilon_0} \left[-\frac{\underline{i}_r}{r} \left(\sum_{n=0,2}^{\infty} a_n^{inc} J_n(k_{0q}r) n \sin n\phi - \sum_{n=1,2}^{\infty} a_n^{inc} J_n(k_{0q}r) n \cos n\phi \right) \right. \\ &\quad \left. - \underline{i}_\phi k_q \left(\sum_{n=0,2}^{\infty} a_n^{inc} J_n'(k_{0q}r) \cos n\phi + \sum_{n=1,2}^{\infty} a_n^{inc} J_n'(k_{0q}r) \sin n\phi \right) \right] \quad (5) \end{aligned}$$

The innermost material will include the cylinder axis. Thus, only Bessel functions of the first kind are permitted in the solution there:

$$\underline{H}^1(\underline{r}, \omega_q) = Y_{1q} \underline{i}_z \left[\sum_{n=0,2}^{\infty} a_{nq}^1 J_n(k_{1q}r) \cos n\phi + \sum_{n=1,2}^{\infty} a_{nq}^1 J_n(k_{1q}r) \sin n\phi \right] \quad (6)$$

$$\begin{aligned}
E^1(r, \omega_q) = & \frac{iY_{1q}}{\omega_q \epsilon_1} \left[-\frac{i}{r} \left(\sum_{n=0,2}^{\infty} a_{nq}^1 J_n(k_{1q}r) n \sin n\phi - \sum_{n=1,2}^{\infty} a_{nq}^1 J_n(k_{1q}r) n \cos n\phi \right) \right. \\
& \left. - \frac{i}{\phi} k_{1q} \left(\sum_{n=0,2}^{\infty} a_{nq}^1 J'_n(k_{1q}r) \cos n\phi + \sum_{n=1,2}^{\infty} a_{nq}^1 J'_n(k_{1q}r) \sin n\phi \right) \right] \quad (7)
\end{aligned}$$

where Y_{1q} is the admittance of medium 1

$$Y_{1q} = \frac{\sqrt{\epsilon_1 + j\sigma_1/\omega_q}}{\mu_1 + j\sigma_1^*/\omega_q} \quad (8)$$

and k_{1q} is the wavenumber of medium 1 at ω_q ,

$$k_{1q} = \omega_q \sqrt{(\epsilon_1 + j\sigma_1/\omega_q)(\mu_1 + j\sigma_1^*/\omega_q)} \quad (9)$$

The $N-1$ concentric shells will permit solutions of both kinds. Thus, in region i , $1 < i \leq N$, $a_{nq}^1 J_n(k_{1q}r)$ of eqs. (6) - (9) becomes replaced by

$$a_{nq}^1 J_n(k_{1q}r) \rightarrow a_{nq}^i J_n(k_{iq}r) + b_{nq}^i Y_n(k_{iq}r) \quad (10)$$

Finally, in free space outside the cylinder, the first Hankel function is the only permitted solution for the scattered field. Thus, in this region, $a_n^{\text{inc}} J_n(k_{0q}r)$ is replaced by

$$a_n^{\text{inc}} J_n(k_{0q}r) \rightarrow a_{nq}^{\text{scat}} H_n^{(1)}(k_{0q}r) \quad (11)$$

in eqs. (3) - (5).

The boundary conditions at each interface are that ϵE_r , E_ϕ and H_z be continuous. It turns out that the first and third of these conditions are equivalent. Thus, matching of coefficients at the innermost interface leads to

$$a_{nq}^1 Y_{1q} J_n(k_{1q} a_1) - a_{nq}^2 Y_{2q} J_n(k_{2q} a_1) - b_{nq}^2 Y_{2q} Y_n(k_{2q} a_1) = 0$$

$$a_{nq}^1 J'_n(k_{1q} a_1) - a_{nq}^2 J'_n(k_{2q} a_1) - b_{nq}^2 Y'_n(k_{2q} a_1) = 0 \quad (12)$$

Matching of coefficients at any other interface except the outer boundary of the cylinder gives

$$a_{nq}^{i-1} Y_{i-1,q} J_n(k_{i-1,q} a_{i-1}) + b_{nq}^{i-1} Y_{i-1,q} Y_n(k_{i-1,q} a_{i-1})$$

$$- a_{nq}^i Y_{iq} J_n(k_i a_{i-1}) - b_{nq}^i Y_{iq} Y_n(k_{iq} a_{i-1}) = 0$$

$$a_{nq}^{i-1} J'_n(k_{i-1,q} a_{i-1}) + b_{nq}^{i-1} Y'_n(k_{i-1,q} a_{i-1})$$

$$- a_{nq}^i J'_n(k_{iq} a_{i-1}) - b_{nq}^i Y'_n(k_{iq} a_{i-1}) = 0 \quad (13)$$

Finally, the boundary condition at the outermost surface is

$$a_{nq}^N Y_{Nq} J_n(k_{Nq} a_N) + b_{nq}^N Y_{Nq} Y_n(k_{Nq} a_N) - a_{nq}^{\text{scat}} Y_0 H_n^{(1)}(k_{0q} a_N)$$

$$= a_n^{\text{inc}} Y_0 J_n(k_{0q} a_N)$$

$$a_{nq}^N J'_n(k_{Nq} a_N) + b_{nq}^N Y'_n(k_{Nq} a_N) - a_{nq}^{\text{scat}} H_n^{(1)'}(k_{0q} a_N) = a_n^{\text{inc}} J'_n(k_{0q} a_N) \quad (14)$$

For each azimuthal harmonic and each frequency, eqs. (12) - (14) comprise a set of $2N$ linear equations in $2N$ unknowns. The associated matrix is five-banded, and extremely easy to solve by Gaussian elimination. (The main diagonal and first diagonal off each side of the main is full. The second diagonal off each side of the main is half zeros.)

The quantities of interest in RCS evaluation are the $a_{nq}^{\text{scat},s}$. A two-dimensional bistatic RCS is defined by

$$\text{RCS}(\phi'_p, \omega_q) = 2\pi r \lim_{r \rightarrow \infty} \left| \frac{\underline{E}^{\text{scat}}(\phi'_p, \omega_q) \sqrt{r'_p}}{\underline{E}^{\text{inc}}} \right|^2 \quad (15)$$

The scattered electric field (neglecting the reactive radial component) is

$$\begin{aligned} \underline{E}^{\text{scat}}(\underline{r}'_p, \omega_q) \\ = - \frac{i}{\phi} \left(\sum_{n=0,2}^{\infty} a_{nq}^{\text{scat}} H_n^{(1)'}(k_{0q} r'_p) \cos n\phi'_p + \sum_{n=1,2}^{\infty} a_{nq}^{\text{scat}} H_n^{(1)'}(k_{0q} r'_p) \sin n\phi'_p \right) \end{aligned} \quad (16)$$

Here, use is made of the identity $k_{0q} Y_0 = \omega_q \epsilon_0$.

For large arguments, Hankel functions have the asymptotic limit

$$H_n^{(1)}(k_0 r'_p) \rightarrow \sqrt{\frac{2}{\pi k_0 r'_p}} e^{i(kr'_p - \frac{2n+1}{4}\pi)} \quad (17)$$

Substitution of eqs. (16) and (17) in (15) then yields the RCS in terms of the a_{nq}^{scat} :

$$\text{RCS}(\phi'_p, \omega_q) = \frac{4}{k_0} \left| \sum_{n=0,2}^{\infty} a_{nq}^{\text{scat}} (-j)^n \cos n\phi'_p + \sum_{n=1,2}^{\infty} a_{nq}^{\text{scat}} (-1)^n \sin n\phi'_p \right|^2 \quad (18)$$

A total of six code-code comparisons have been made between the cylindrical-harmonic frequency-domain algorithm and our TDFD code. First we examined a solid dielectric circular cylinder of $\epsilon_r = 2$. The cylinder was given a radius $a = .5$ m. We used an angle of incidence of $\phi^{\text{inc}} = +45^\circ$ from the x-axis. Meshing was square, with each cell .04 m on a side. Figure 3 illustrates the TDFD cross-sectional model for the cylinder.

Figure 4 is a linear comparison of the monostatic result, and Figure 5 is a dB comparison. Figure 6 is a linear comparison of the bistatic result of 250 MHz, and Figure 7 is a dB comparison. Figures 8 and 9 are bistatic comparisons at 500 MHz.

The second comparison was an identical cylinder except that ϵ_r was increased to $\epsilon_r = 9$. Figures 10 - 15 compare the same data as Figures 4 - 9 did for the first example.

Figure 16 is a four-way dB comparison of the monostatic RCS computed by both techniques for both values of ϵ_r .

Good agreement occurs for all the $\epsilon_r = 2$ comparisons, but discrepancies occur above 300 MHz when $\epsilon_r = 9$. For instance, agreement is not good in the bistatic result at $\epsilon_r = 9$ when frequency is 500 MHz (Fig. 15). If $\epsilon_r = 9$, 300 MHz corresponds to a wavelength in the cylinder of .33 m, or about 16 cells per wavelength. The conclusion that a wavelength must be resolved into 16 segments to get good finite-difference results is neither new nor surprising.

DIELECTRIC ROD CROSS SECTION

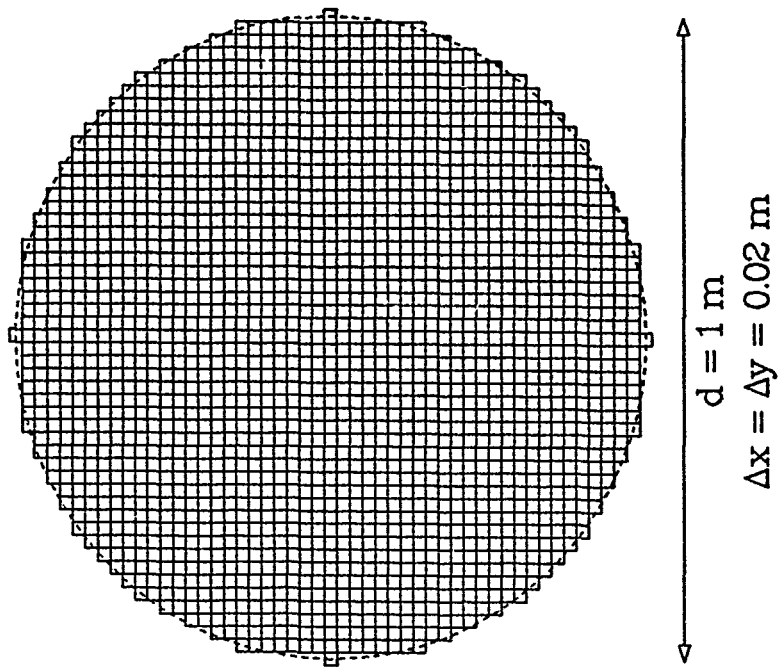


Figure 3. TDFD model of a dielectric cylinder with .5 m radius and .02 m square cells.

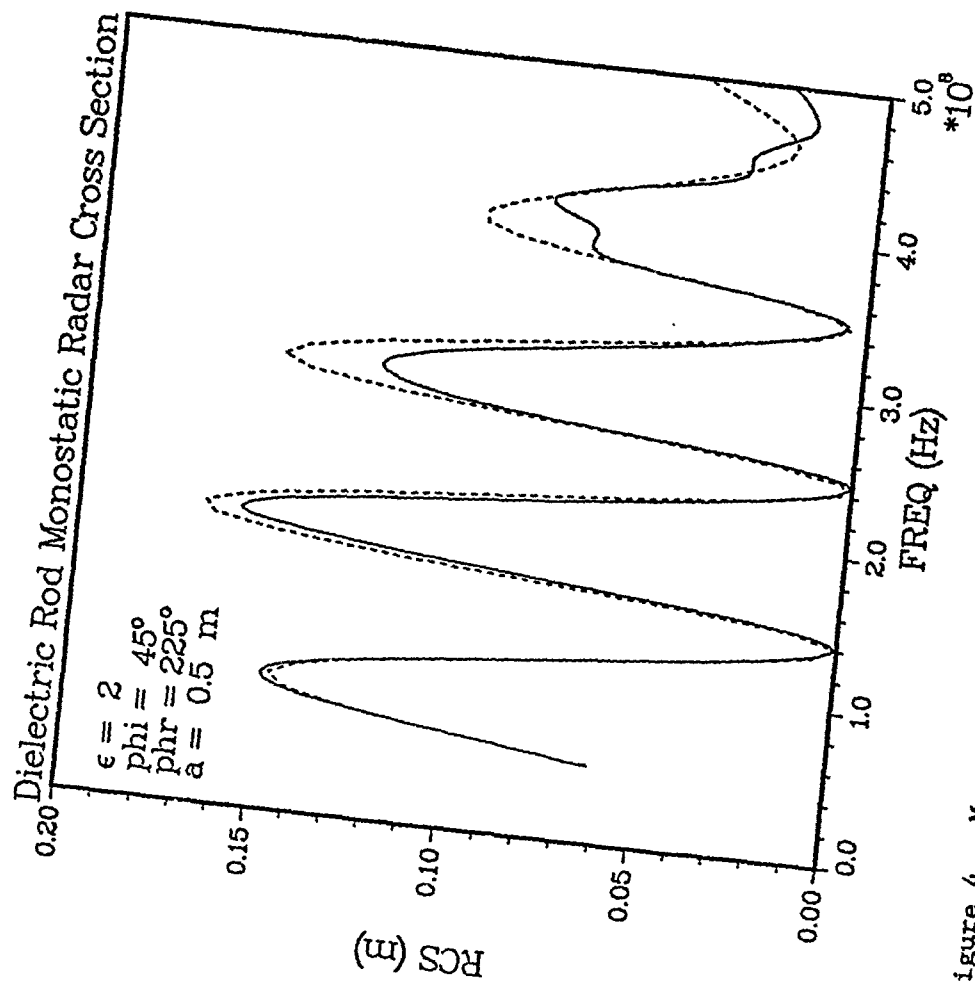


Figure 4. Monostatic RCS for a circular dielectric cylinder with $\epsilon_r = 2$. Solid curve is the TDFD result, and dashed line is the cylindrical-harmonic result. Plot is based on illumination at $\phi_{inc} = \pi/4$.

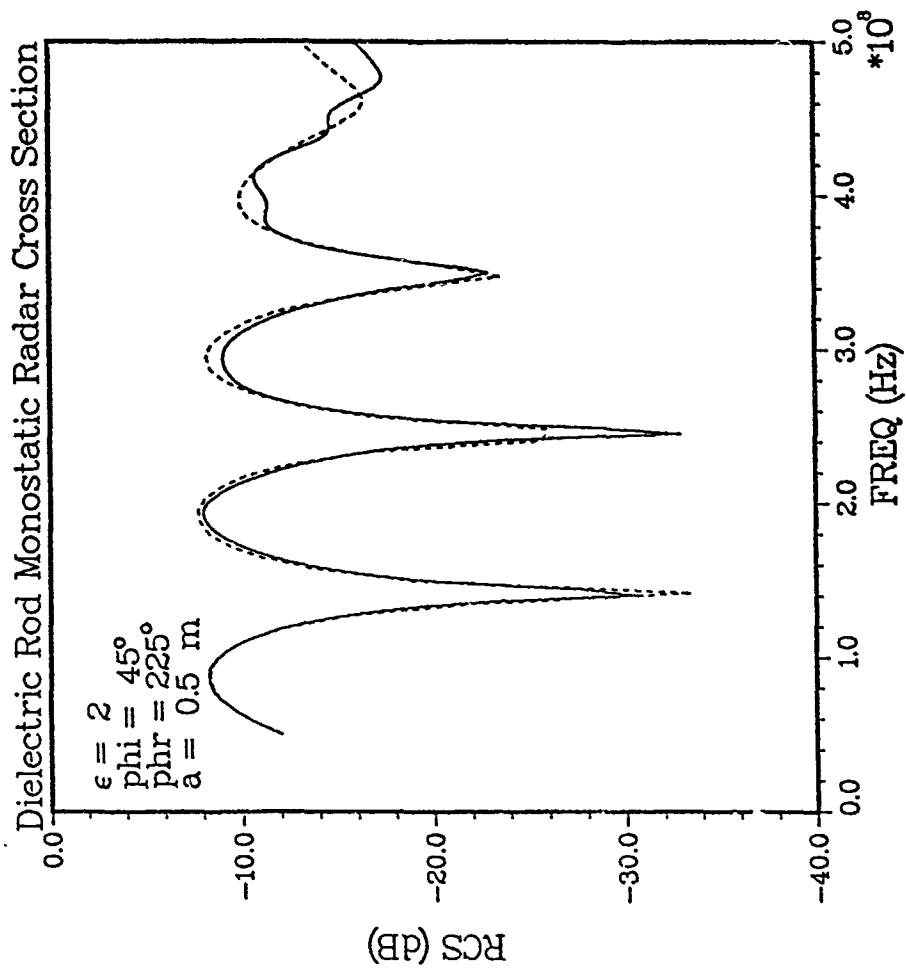


Figure 5. Monostatic RCS for a circular dielectric cylinder with $\epsilon_r = 2$. Solid curve is the TDFD result, and dashed line is the cylindrical-harmonic result. Plot is based on illumination at $\phi_{inc} = \pi/4$.

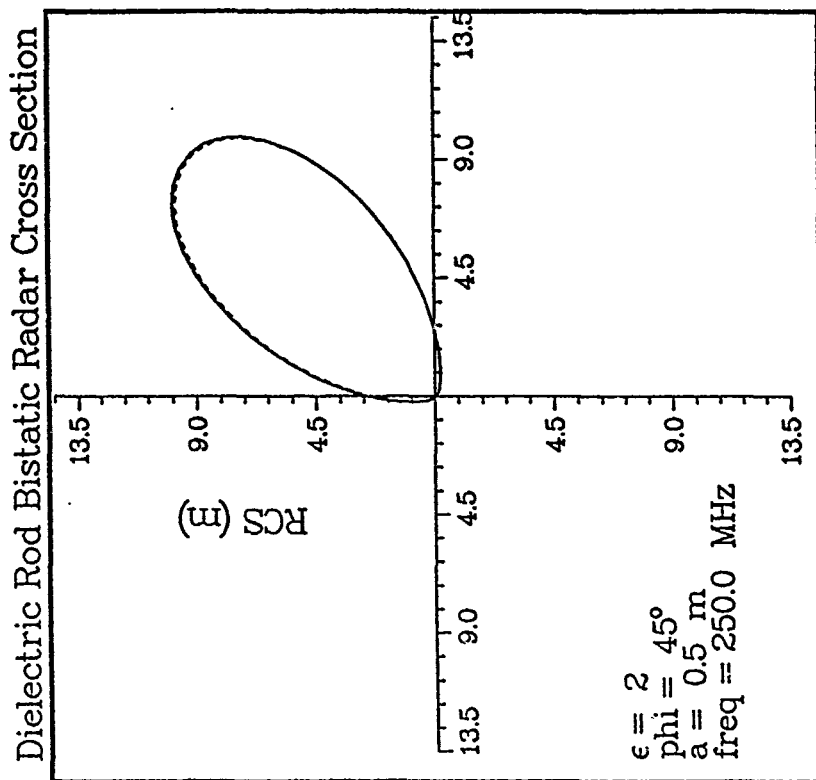


Figure 6. Bistatic RCS for a circular dielectric cylinder with $\epsilon_r = 2$ at 250 MHz. Solid curve is the TDFD result, and dashed line is the cylindrical-harmonic result. Plot is based on illumination at $\phi_{\text{inc}} = \pi/4$.

Dielectric Rod Bistatic Radar Cross Section

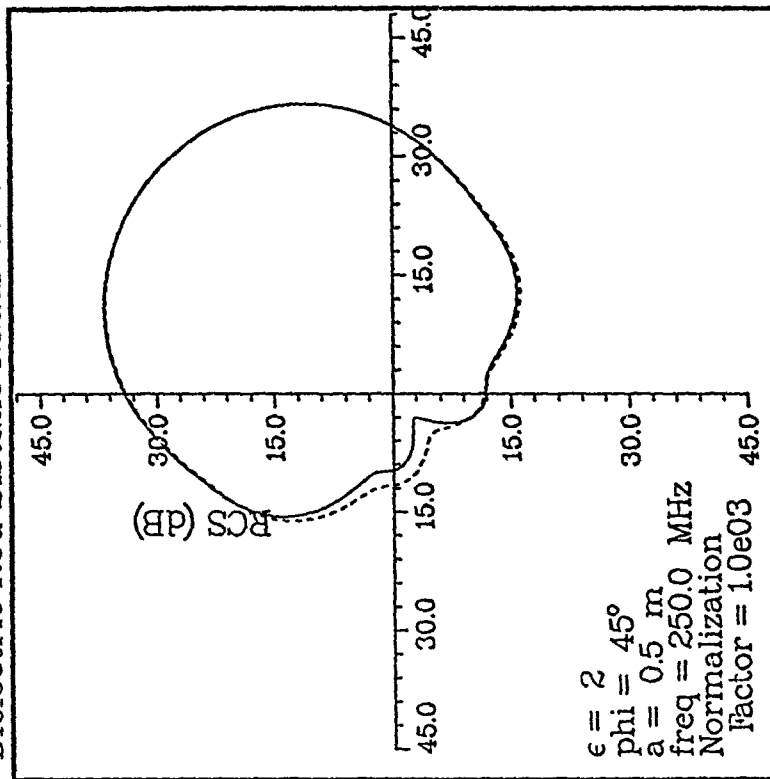


Figure 7. Bistatic RCS for a circular dielectric cylinder with $\epsilon_r = 2$ at 250 MHz. Solid curve is the TDFD result, and dashed line is the cylindrical-harmonic result. Plot is based on illumination at $\phi_{\text{inc}} = \pi/4$.

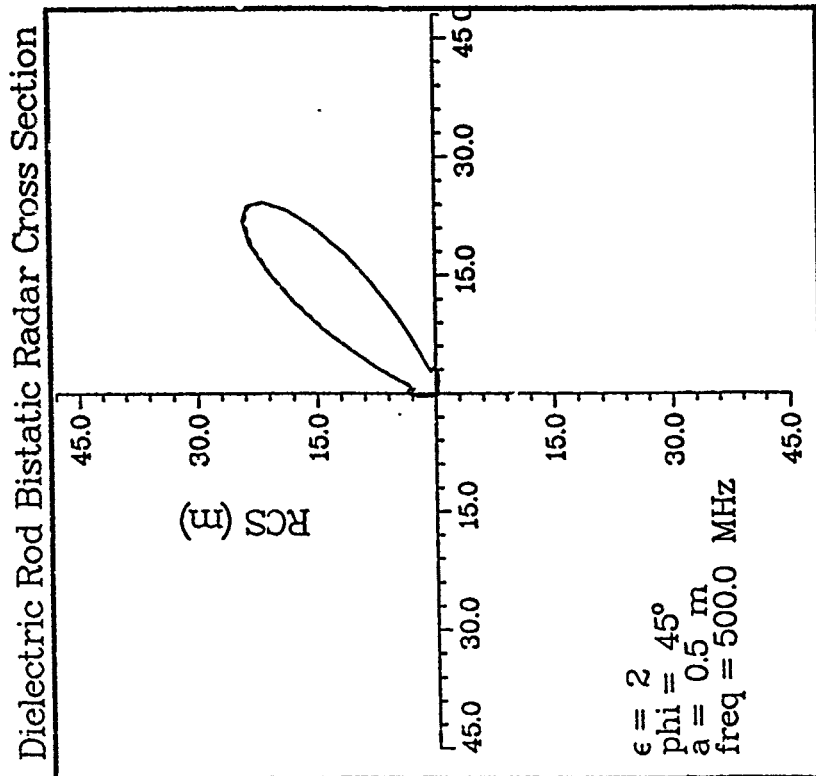


Figure 8. Bistatic RCS for a circular dielectric cylinder with $\epsilon_r = 2$ at 500 MHz. Solid curve is the TDFD result, and dashed line is the cylindrical-harmonic result. Plot is based on illumination at $\phi_{inc} = \pi/4$.

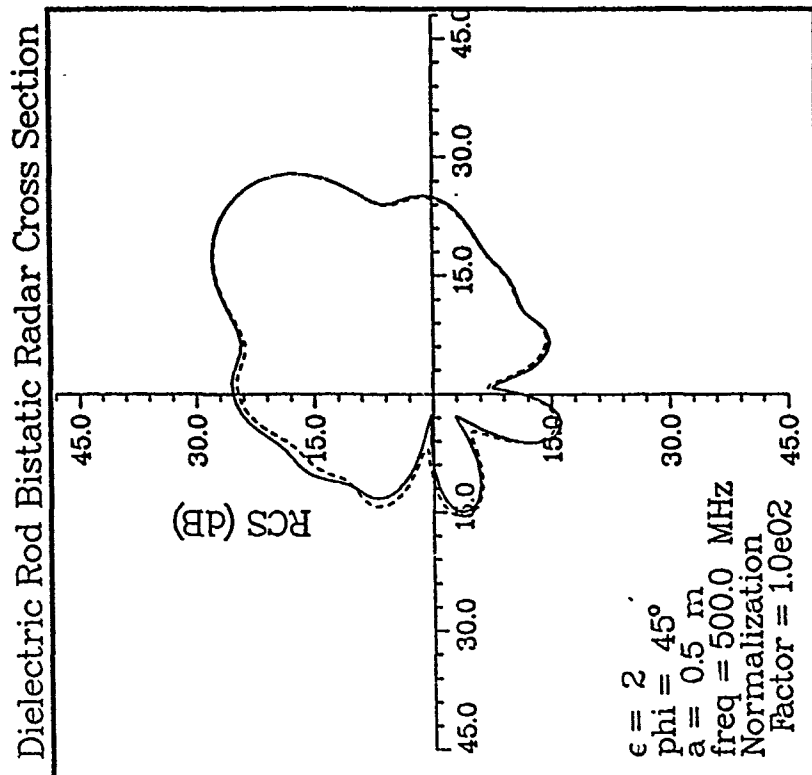


Figure 9. Bistatic RCS for a circular dielectric cylinder with $\epsilon_r = 2$ at 500 MHz. Solid curve is the TDFD result, and dashed line is the cylindrical-harmonic result. Plot is based on illumination at $\phi_{\text{inc}} = \pi/4$.

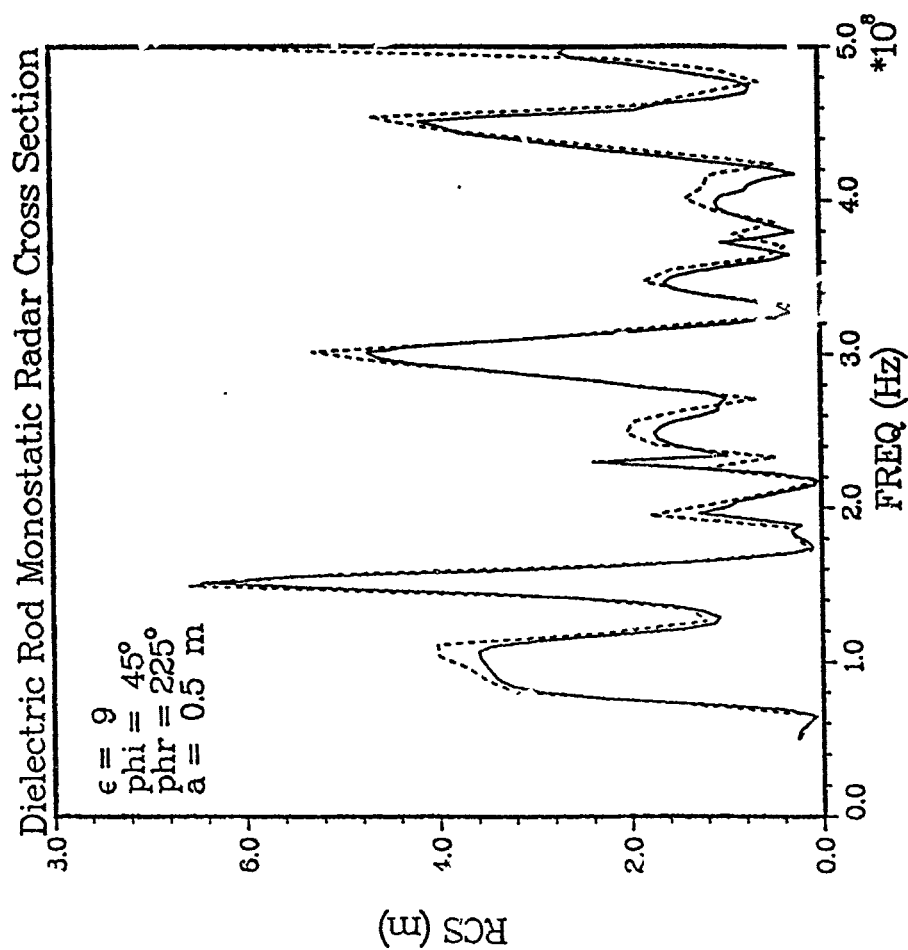


Figure 10. Monostatic RCS for a circular dielectric cylinder with $\epsilon_r = 9$. Solid curve is the TDFD result, and dashed line is the cylindrical-harmonic result. Plot is based on illumination at $\phi_{inc} = \pi/4$.

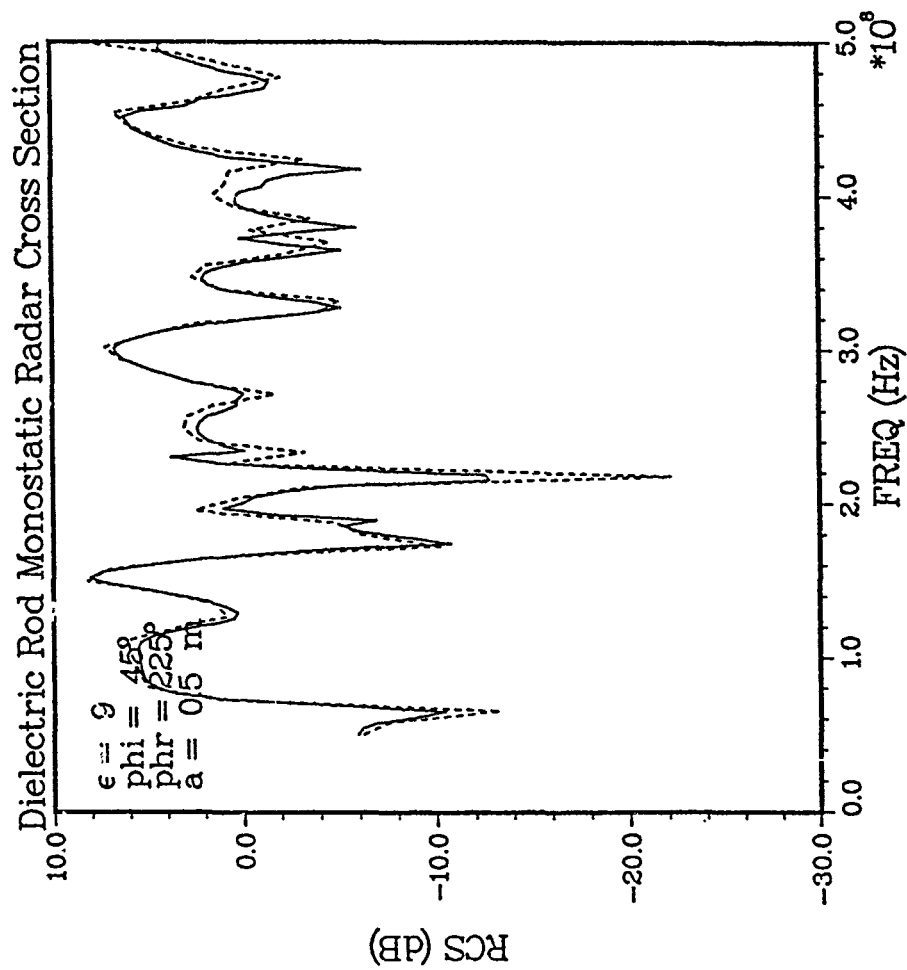


Figure 11. Monostatic RCS for a circular dielectric cylinder with $\epsilon_r = 9$. Solid curve is the TDFD result, and dashed line is the cylindrical-harmonic result. Plot is based on illumination at $\phi^{\text{inc}} = \pi/4$.

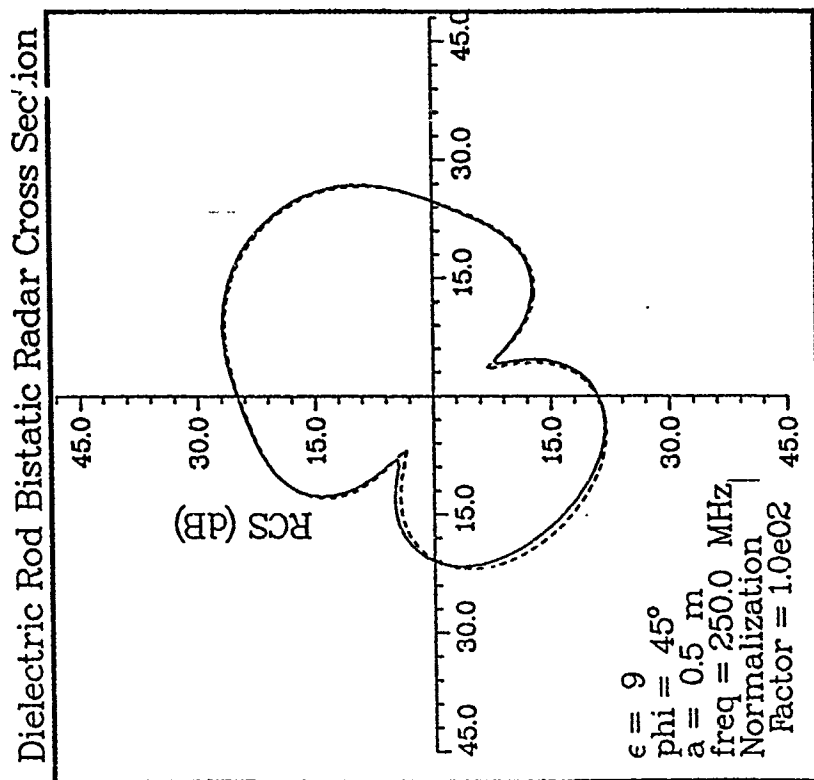


Figure 13. Bistatic RCS for a circular dielectric cylinder with $\epsilon_r = 9$ at 250 MHz. Solid curve is the TDFD result, and dashed line is the cylindrical-harmonic result. Plot is based on illumination at $\phi_{\text{inc}} = \pi/4$.

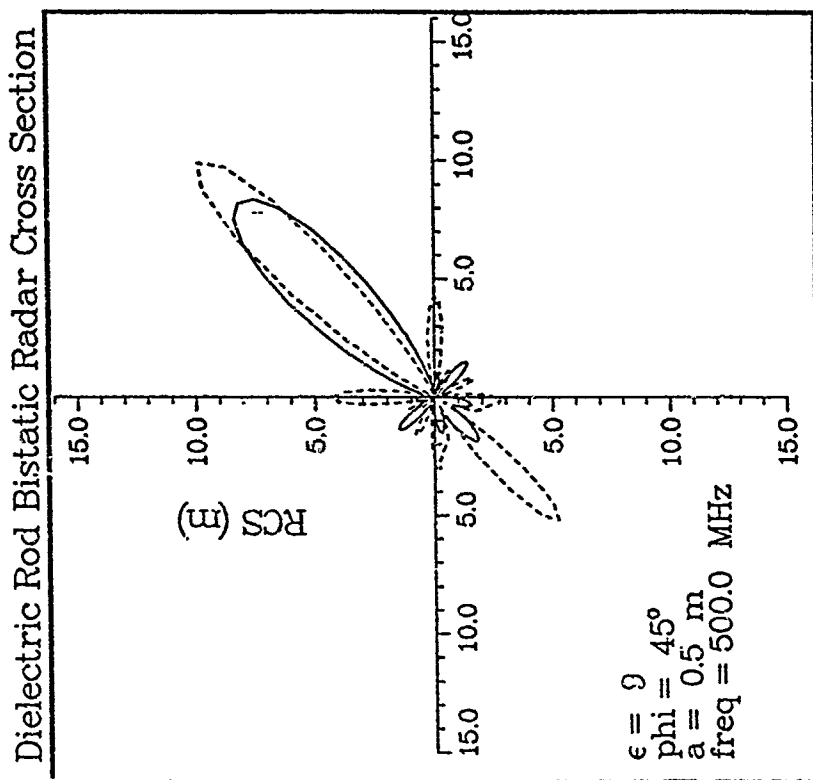


Figure 14. Bistatic RCS for a circular dielectric cylinder with $\epsilon_r = 9$ at 500 MHz. Solid curve is the TDFD result, and dashed line is the cylindrical-harmonic result. Plot is based on illumination at $\phi_{\text{inc}} = \pi/4$.

Dielectric Rod Bistatic Radar Cross Section

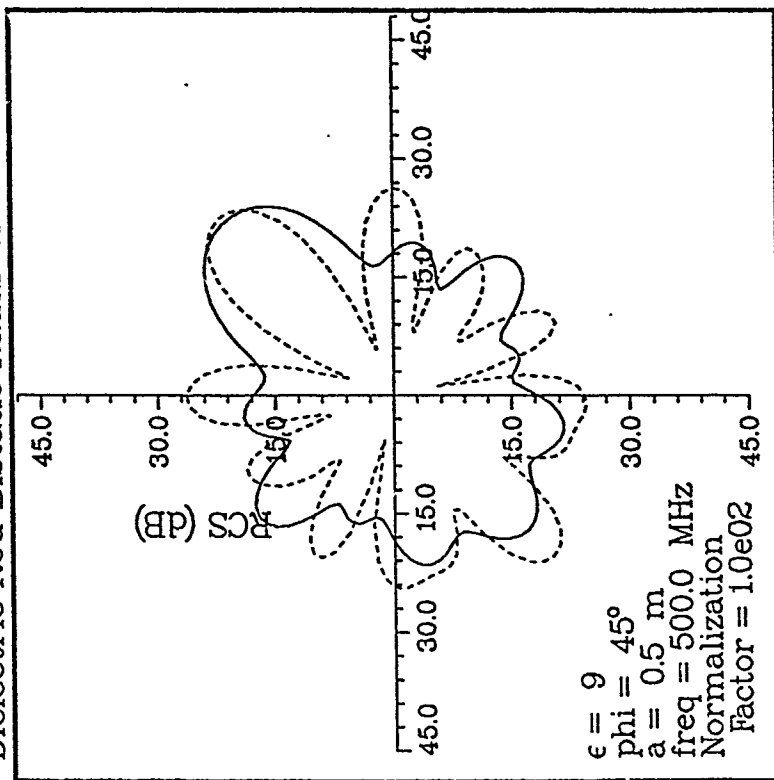


Figure 15. Bistatic RCS for a circular dielectric cylinder with $\epsilon_r = 9$ at 500 MHz. Solid curve is the TDFD result, and dashed line is the cylindrical-harmonic result. Plot is based on illumination at $\phi_{\text{inc}} = \pi/4$.

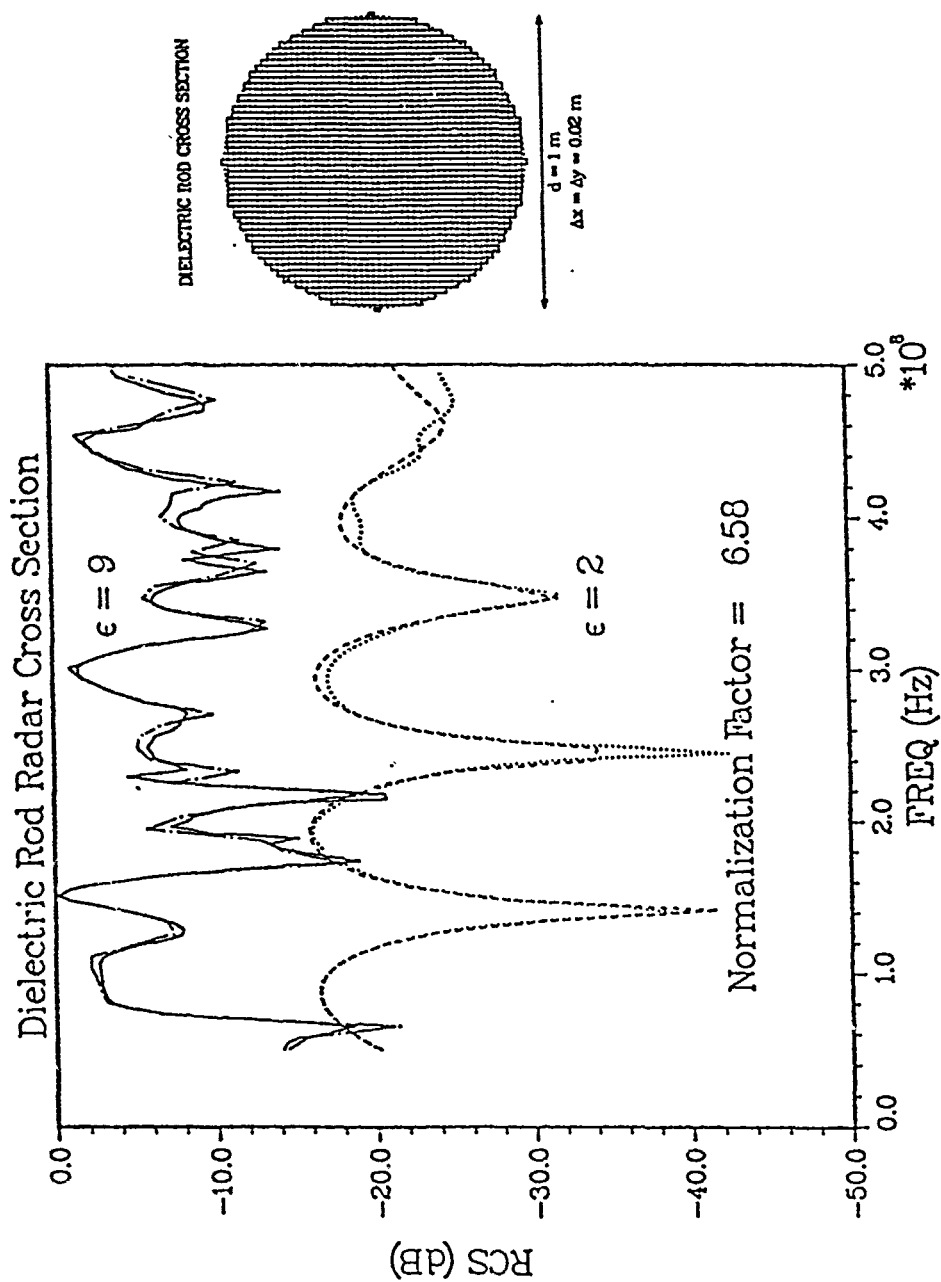


Figure 16. Monostatic RCS of a circular dielectric cylinder with \underline{E} transverse to the rod axis. Based on a rod radius of .5 m and cells .02 m on a side.

The third comparison was for a perfectly magnetically conducting cylinder of $a = .5$ m radius. Meshing was again square, but with each cell now .04 m on a side. Figure 17 illustrates this TDFD model.

(TM scattering off a perfectly magnetically conducting cylinder will give identical RCS results as the more familiar problem of TE scattering off a perfectly electrically conducting cylinder.)

Figure 18 shows a linear comparison of the two monostatic RCS calculations, and Figure 19 gives a dB comparison. Figure 20 is a linear comparison of the bistatic result at 250 MHz, and Figure 21 is a dB comparison. Figures 22 and 23 are bistatic comparisons at 500 MHz.

Although all these magnetic-cylinder results show good agreement between the two techniques an interesting minor difference does appear, especially in the second and fourth quadrants, of Figures 21 and 23. In particular, the cylindrical-harmonic bistatic RCS results are exactly symmetrical about the main diagonal ($\phi = 45^\circ$), while the TDFD result is not. We believe a low-grade bug is present in the TDFD coding, but that this bug was undetectable until bistatic capability was added to the TDFD code in the final days of the effort.

The fourth comparison was for a perfectly magnetically conducting rod of the same radius, but coated by a damper .5 m thick. Thus, the overall radius of the composite rod was now 1 m. The damping material had properties $\epsilon_r = 1$, $\mu_r = 1$, $\sigma = \epsilon \sigma^*/\mu = 4 \times 10^{-3}$. These values were selected to give a skin depth on the order of the damper thickness at frequencies (50 - 500 MHz) for which calculations were run. Square cells .04 m on a side were again used.

Figure 24 illustrates the TDFD model of the damped cylinder. Figures 25 - 30 compare the same data as Figures 18 - 23 did for the bare cylinder.

It is important to note that damping the rod reduces the RCS in all but the forward direction, where it enhances the RCS. This occurs because the

MAGNETIC ROD CROSS SECTION

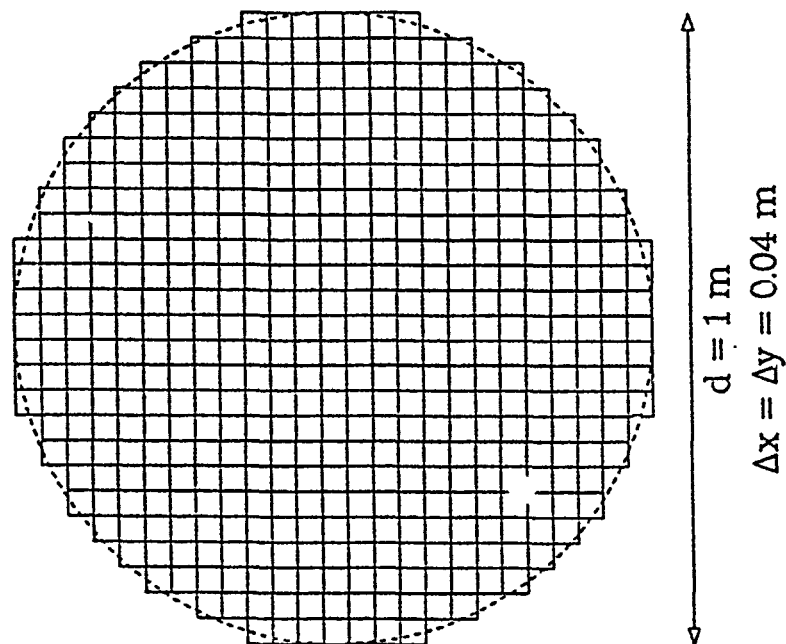


Figure 17. TDFD model of a magnetically conducting circular cylinder with .5 m radius and .04 m square cells.

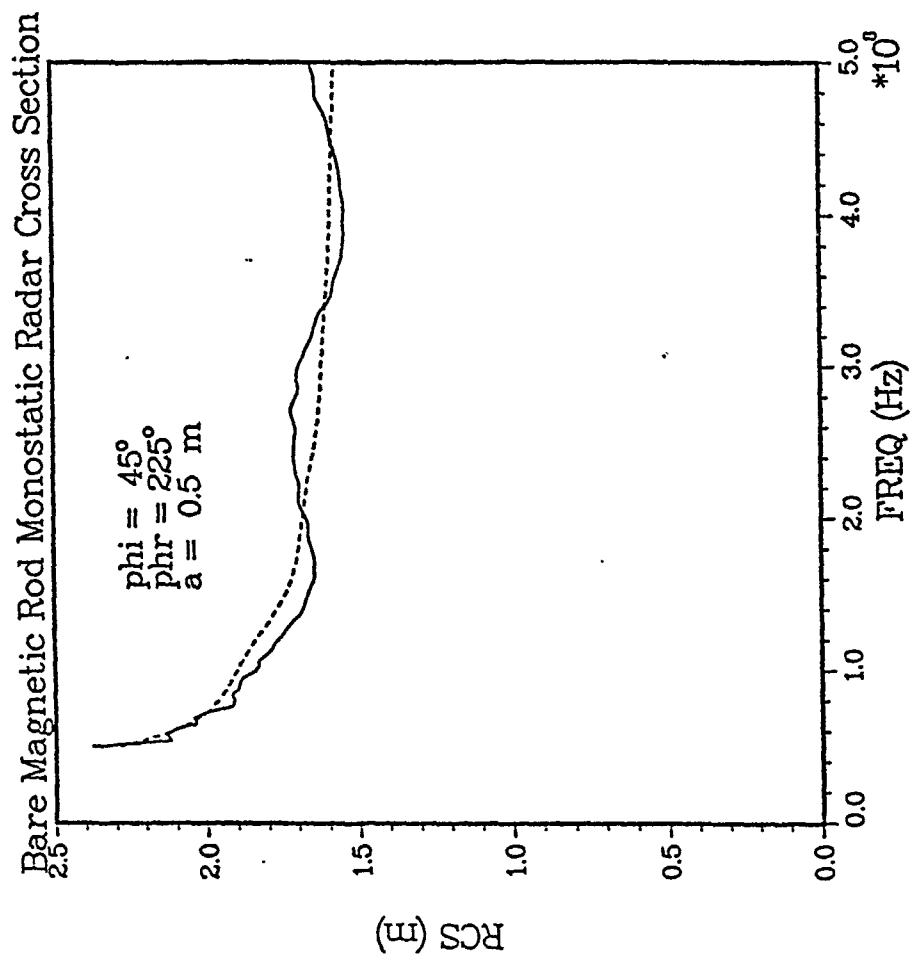


Figure 18. Monostatic RCS for a bare, magnetically conducting circular cylinder. Solid curve is the TDFD result, and dashed line is the cylindrical-harmonic result. Plot is based on illumination at $\phi_{inc} = \pi/4$.

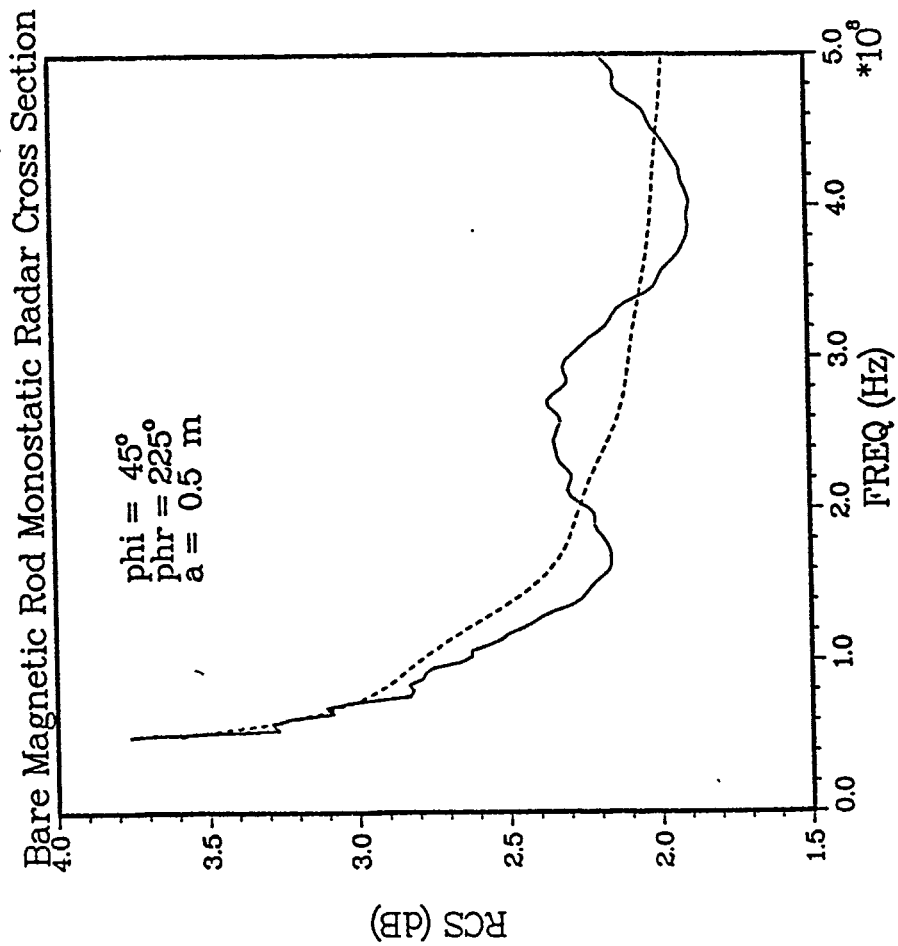


Figure 19. Monostatic RCS for a bare, magnetically conducting circular cylinder. Solid curve is the TDFD result, and dashed line is the cylindrical-harmonic result. Plot is based on illumination at $\phi_{inc} = \pi/4$.

Bare Magnetic Rod Bistatic Radar Cross Section

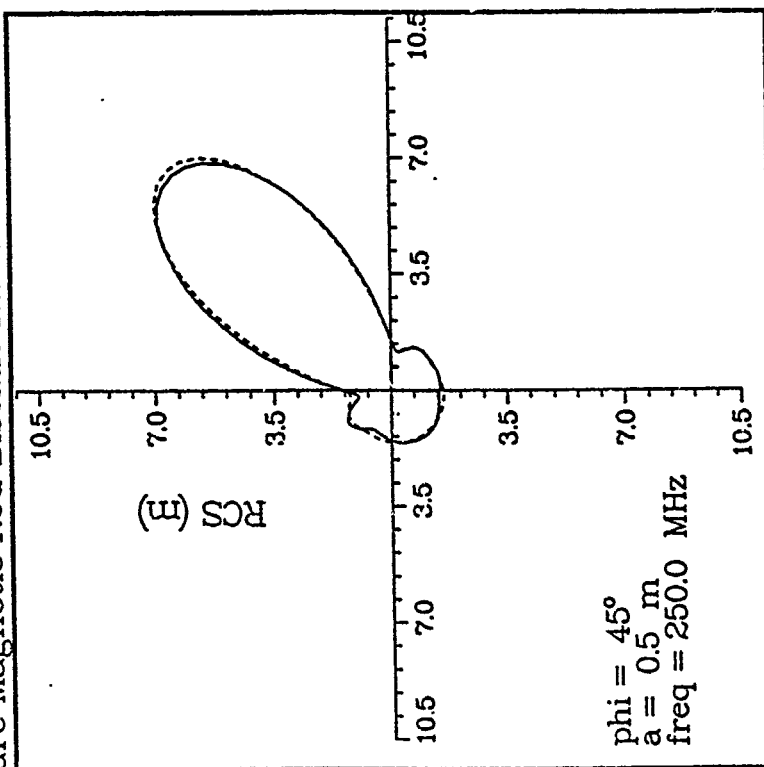


Figure 20. Bistatic RCS for a bare, magnetically conducting circular cylinder at 250 MHz. Solid curve is the TDFD result, and dashed line is the cylindrical-harmonic result. Plot is based on illumination at: $\phi_{\text{inc}} = \pi/4$.

Bare Magnetic Rod Bistatic Radar Cross Section

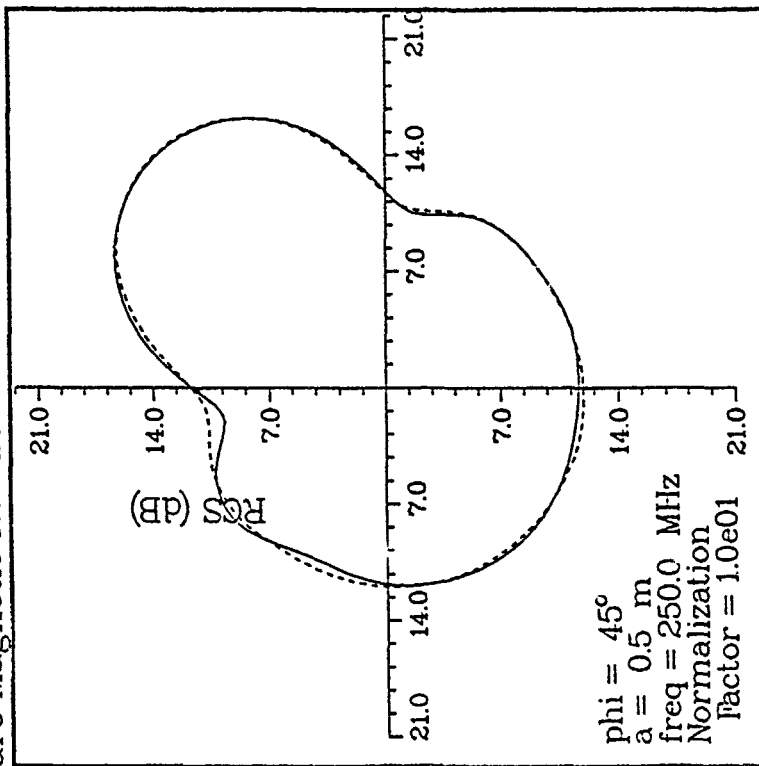


Figure 21. Bistatic RCS for a bare, magnetically conducting circular cylinder at 250 MHz. Solid curve is the TDFD result, and dashed line is the cylindrical-harmonic result. Plot is based on illumination at $\phi_{\text{inc}} = \pi/4$.

Bare Magnetic Rod Bistatic Radar Cross Section

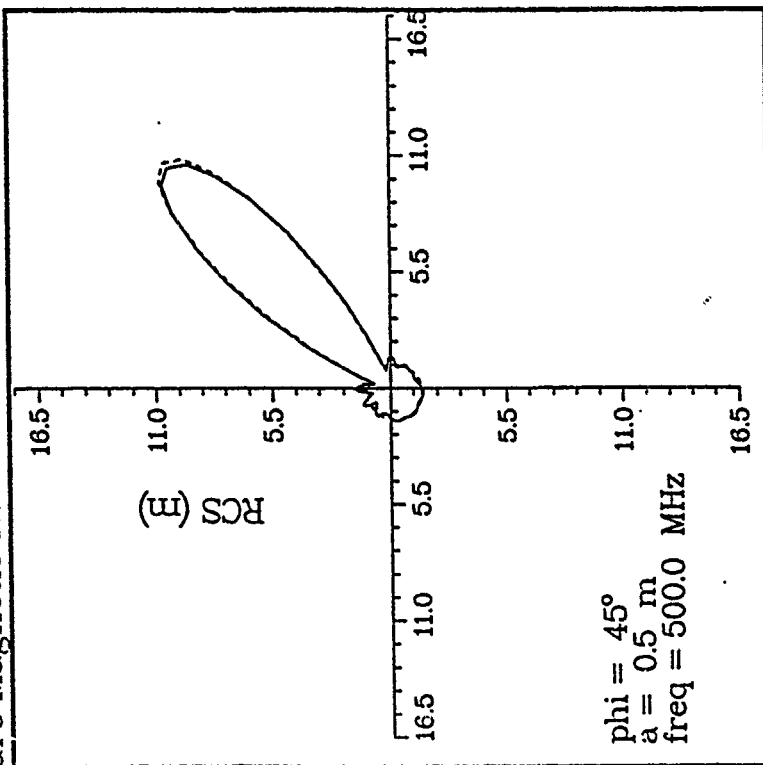


Figure 22. Bistatic RCS for a bare, magnetically conducting circular cylinder at 500 MHz. Solid curve is the TDFD result, and dashed line is the cylindrical harmonic result. Plot is based on illumination at $\phi_{\text{inc}} = \pi/4$.

Bare Magnetic Rod Bistatic Radar Cross Section

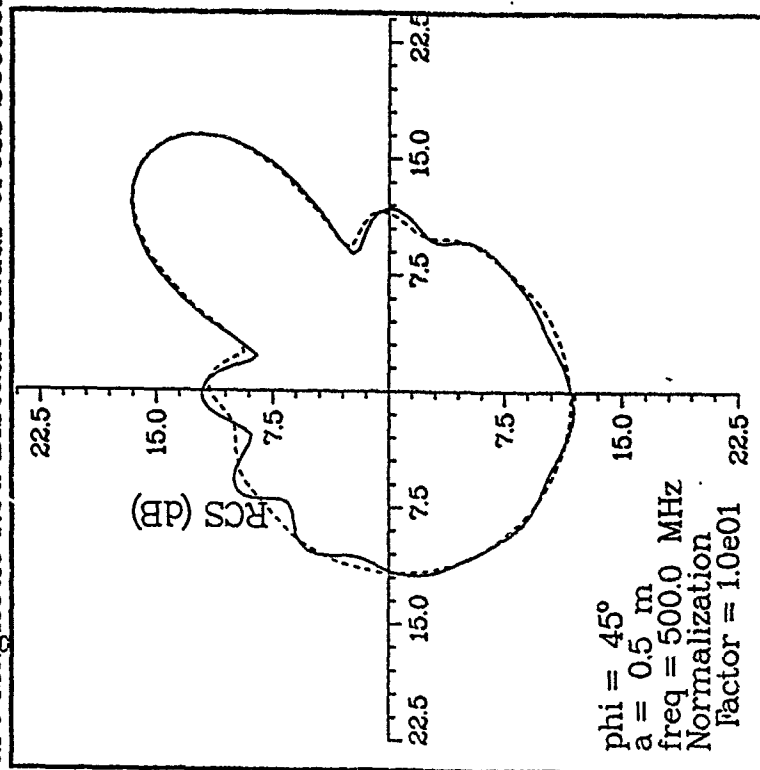


Figure 23. Bistatic RCS for a bare, magnetically conducting circular cylinder at 500 MHz. Solid curve is the TDFD result, and dashed line is the cylindrical harmonic result. Plot is based on illumination at $\phi_{\text{inc}} = \pi/4$.

DAMPED ROD CROSS SECTION

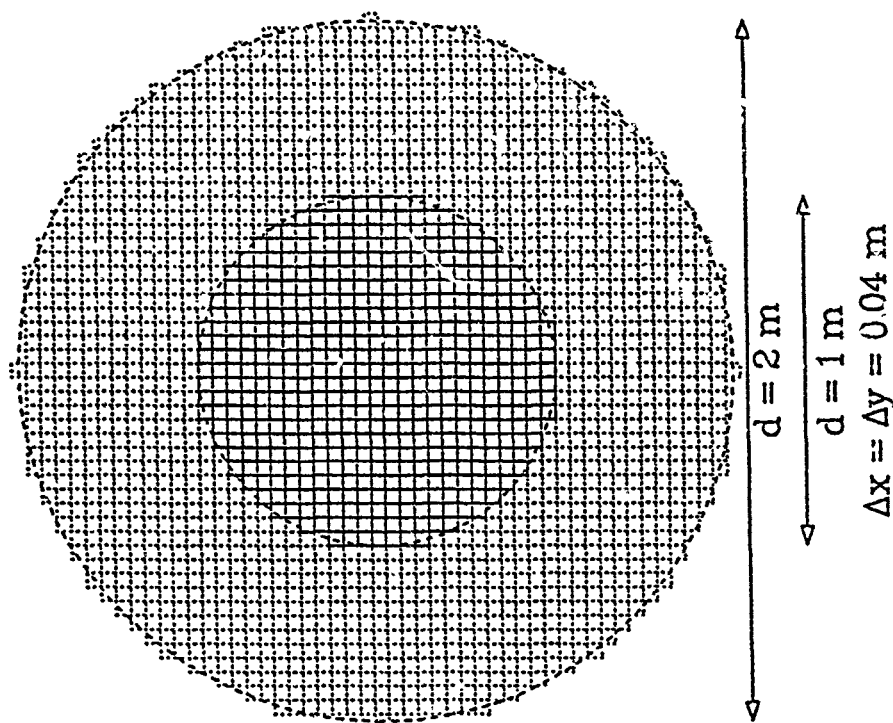


Figure 24. TDFD model of a magnetically conducting cylinder of .5 m radius coated by a damped .5 m thick. Cells are .04 m square.

Coated Magnetic Rod Monostatic Radar Cross Section

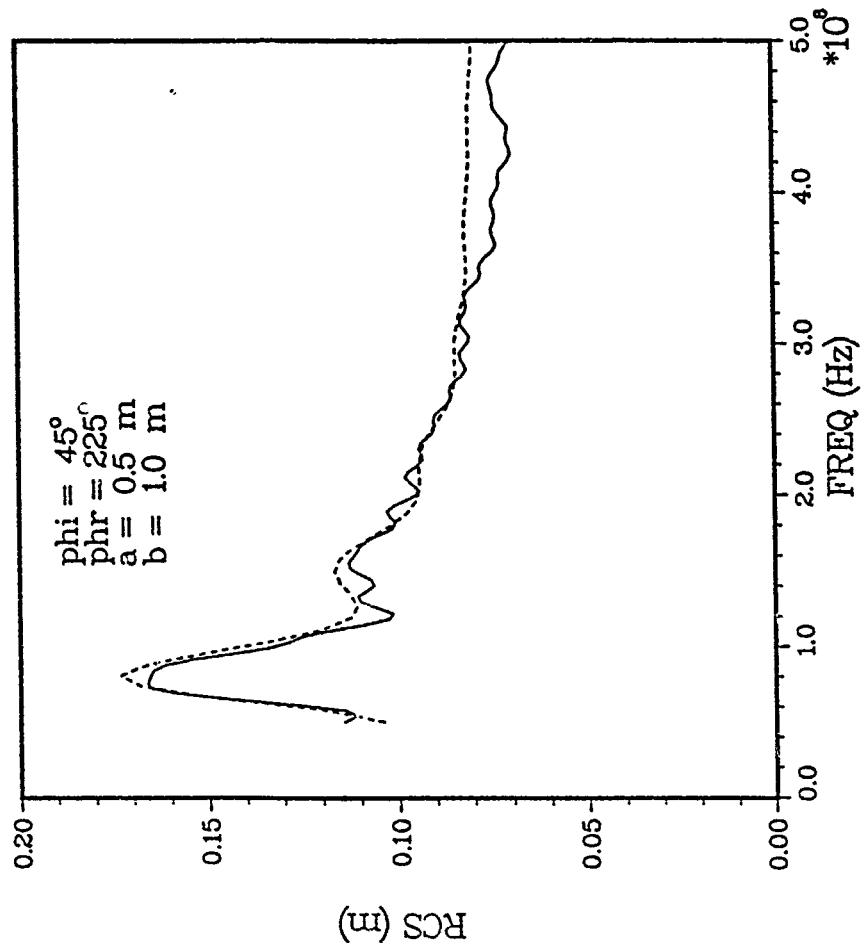


Figure 25. Monostatic RCS for a coated, magnetically conducting circular cylinder. Solid curve is the TDFD result, and dashed line is the cylindrical harmonic result. Plot is based on illumination at $\phi_{inc} = \pi/4$.

Coated Magnetic Rod Monostatic Radar Cross Section

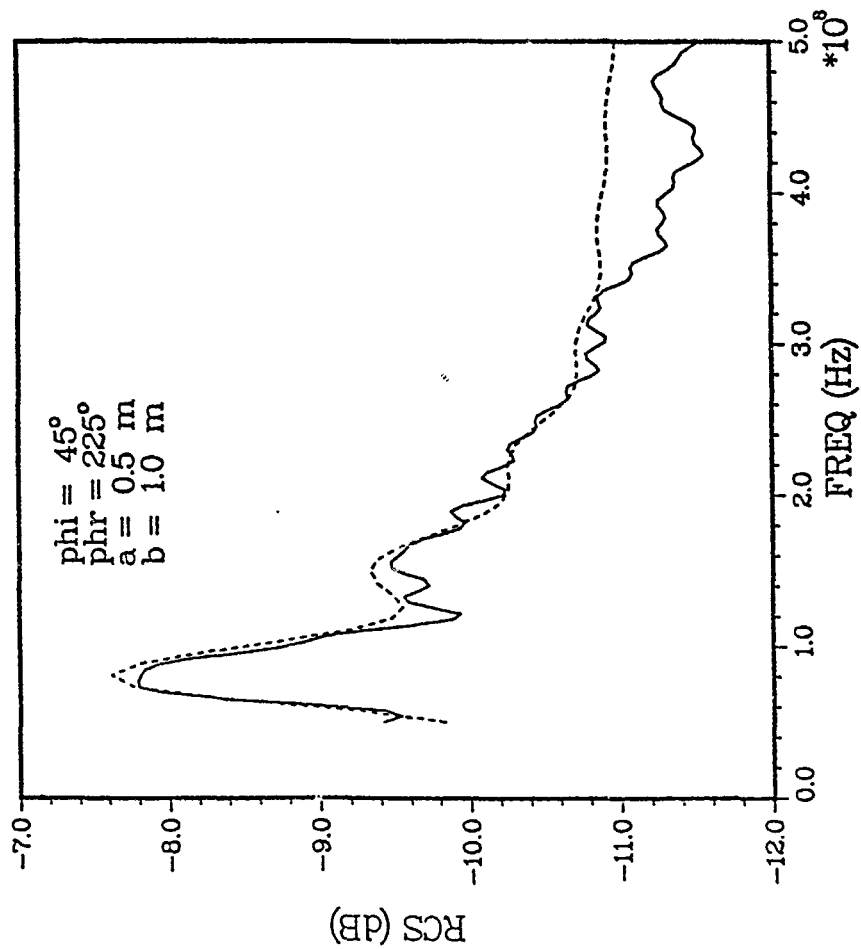


Figure 26. Monostatic RCS for a coated, magnetically conducting circular cylinder. Solid curve is the TDFD result, and dashed line is the cylindrical-harmonic result. Plot is based on illumination at $\phi_{inc} = \pi/4$.

Coated Magnetic Rod Bistatic Radar Cross Section

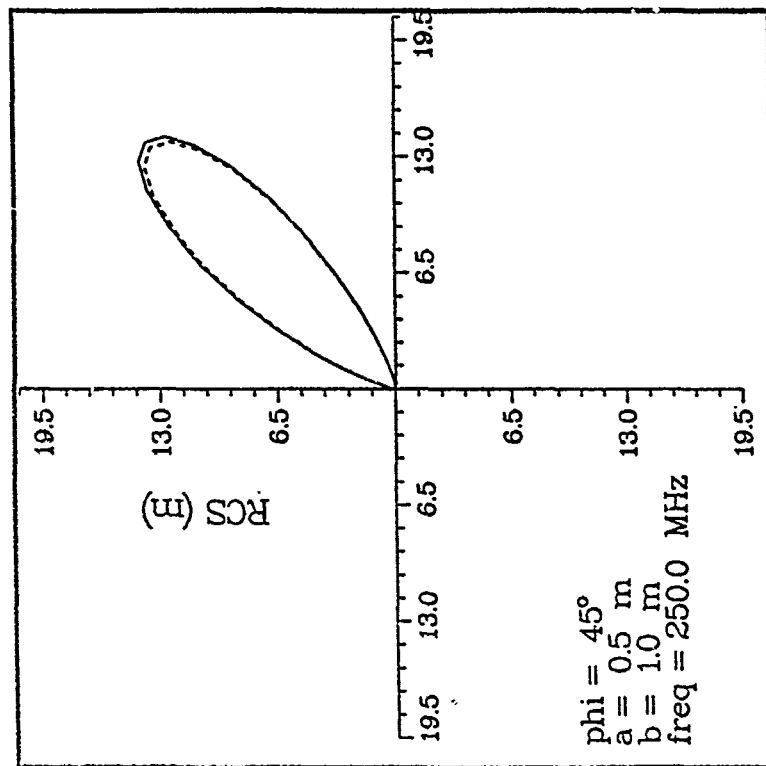


Figure 27. Bistatic RCS for a coated, magnetically conducting circular cylinder at 250 MHz. Solid curve is the TDFD result, and dashed line is the cylindrical-harmonic result. Plot is based on illumination at $\phi_{\text{inc}} = \pi/4$.

Coated Magnetic Rod Bistatic Radar Cross Section

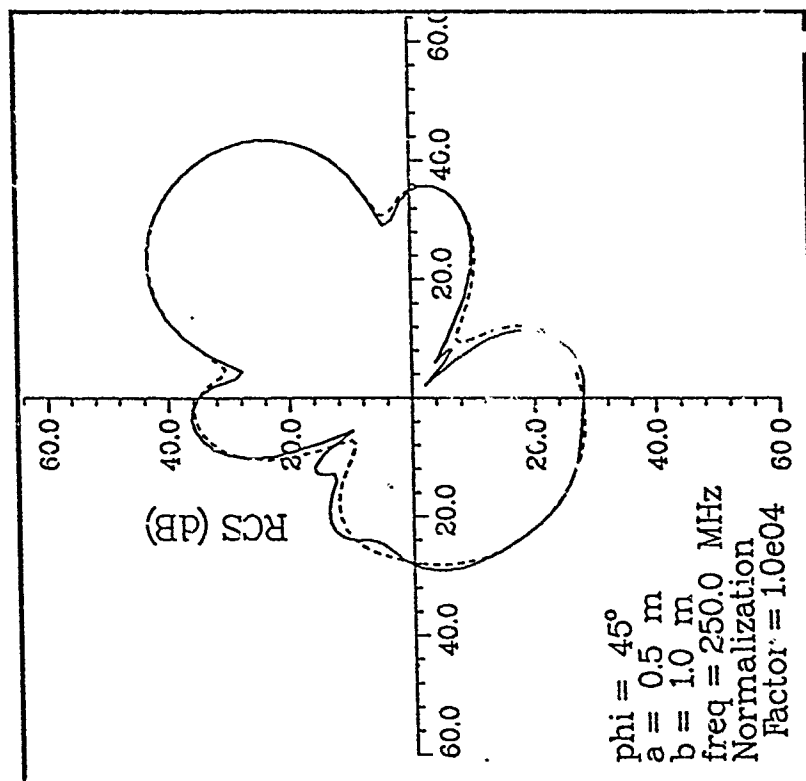


Figure 28. Bistatic RCS for a coated, magnetically conducting circular cylinder at 250 MHz. Solid curve is the TDFD result, and dashed line is the cylindrical-harmonic result. Plot is based on illumination at $\phi_{\text{inc}} = \pi/4$.

Coated Magnetic Rod Bistatic Radar Cross Section

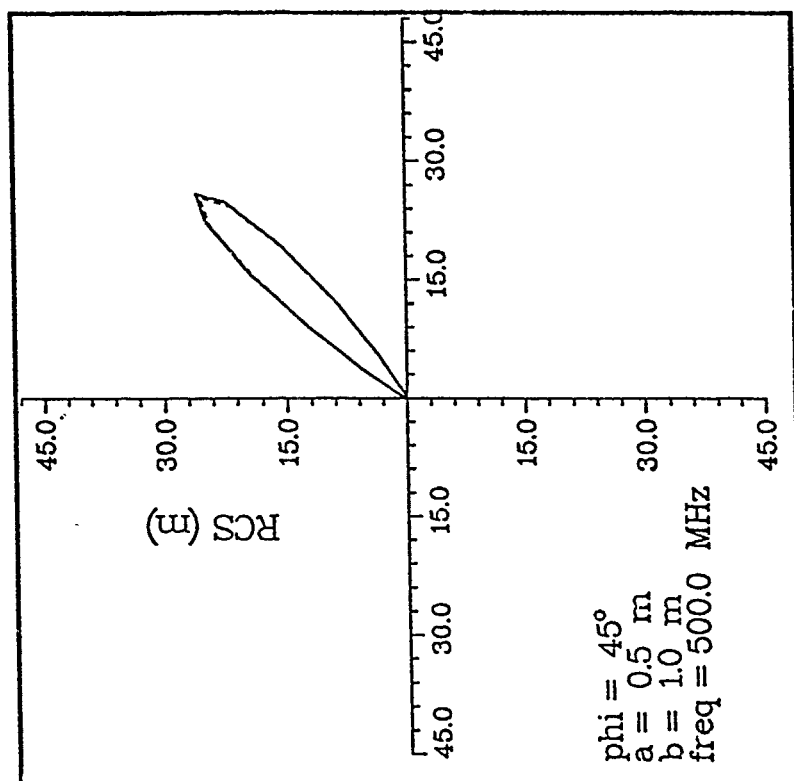


Figure 29. Bistatic RCS for a coated, magnetically conducting circular cylinder at 500 MHz. Solid curve is the TDFD result, and dashed line is the cylindrical harmonic result. Plot is based on illumination at $\phi_{\text{inc}} = \pi/4$.

Coated Magnetic Rod Bistatic Radar Cross Section

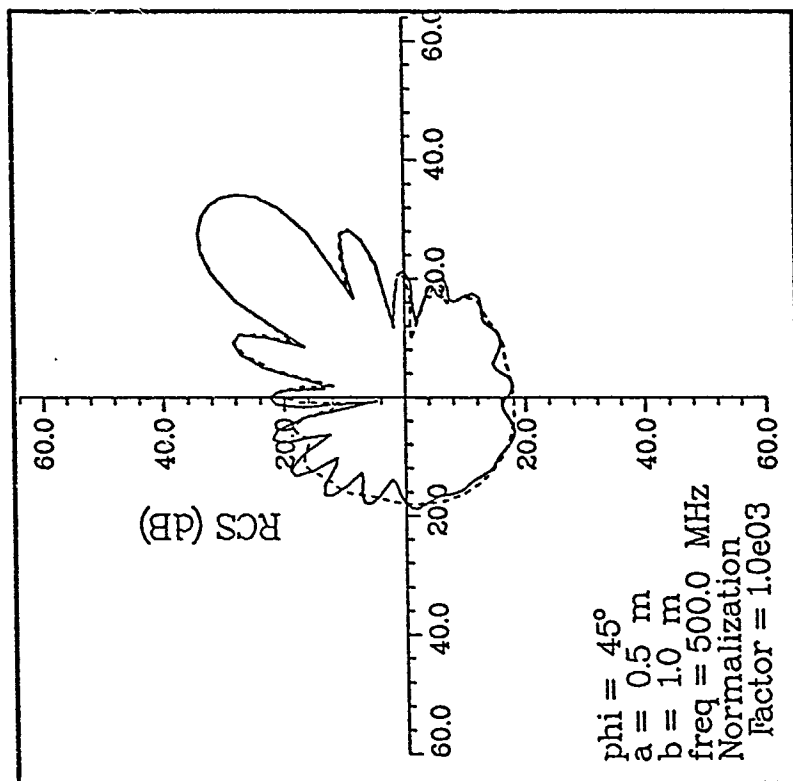


Figure 30. Bistatic RCS for a coated, magnetically conducting circular cylinder at 500 MHz. Solid curve is the TDFD result, and dashed line is the cylindrical harmonic result. Plot is based on illumination at $\phi^{inc} = \pi/4$.

forward direction lies in the scatterer's shadow; that is, $E^{inc} \approx -E^{scat}$ in the forward direction.

Figure 31 is a four-way dB comparison of the monostatic RCS computed by both techniques for the bare and coated magnetic cylinder. It may be seen that the coating reduces the cylinder's RCS by about 13 dB over the frequencies of study.

The fifth and sixth comparisons were the same as the third and fourth, but for a perfectly electrically conducting rod. All other parameters were unchanged between the two pairs of comparisons. Figure 32 gives the four-way dB comparison of the monostatic RCS for the bare and coated electrically conducting cylinder. It may again be seen that the coating results in about a 13 dB reduction of the RCS.

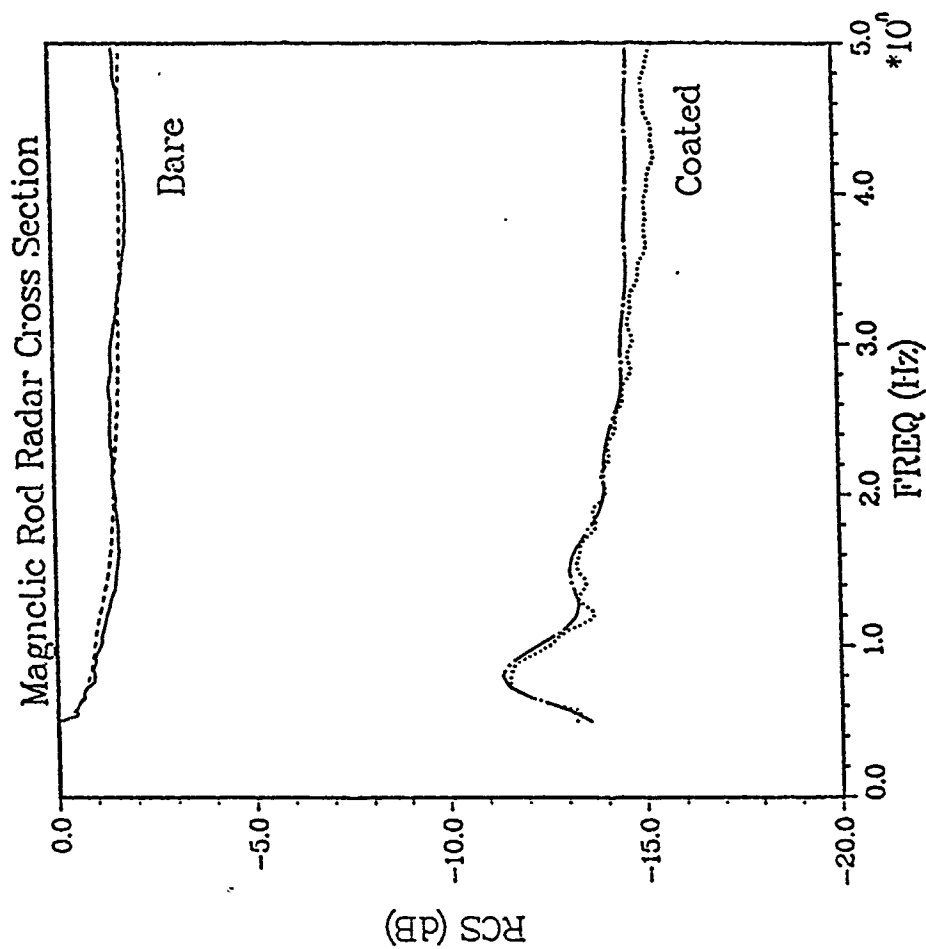


Figure 31. Monostatic RCS of bare and damped magnetically conducting cylinders with H parallel to cylinder axes. Plot is based on illumination at $\phi_{inc} = \pi/4$.

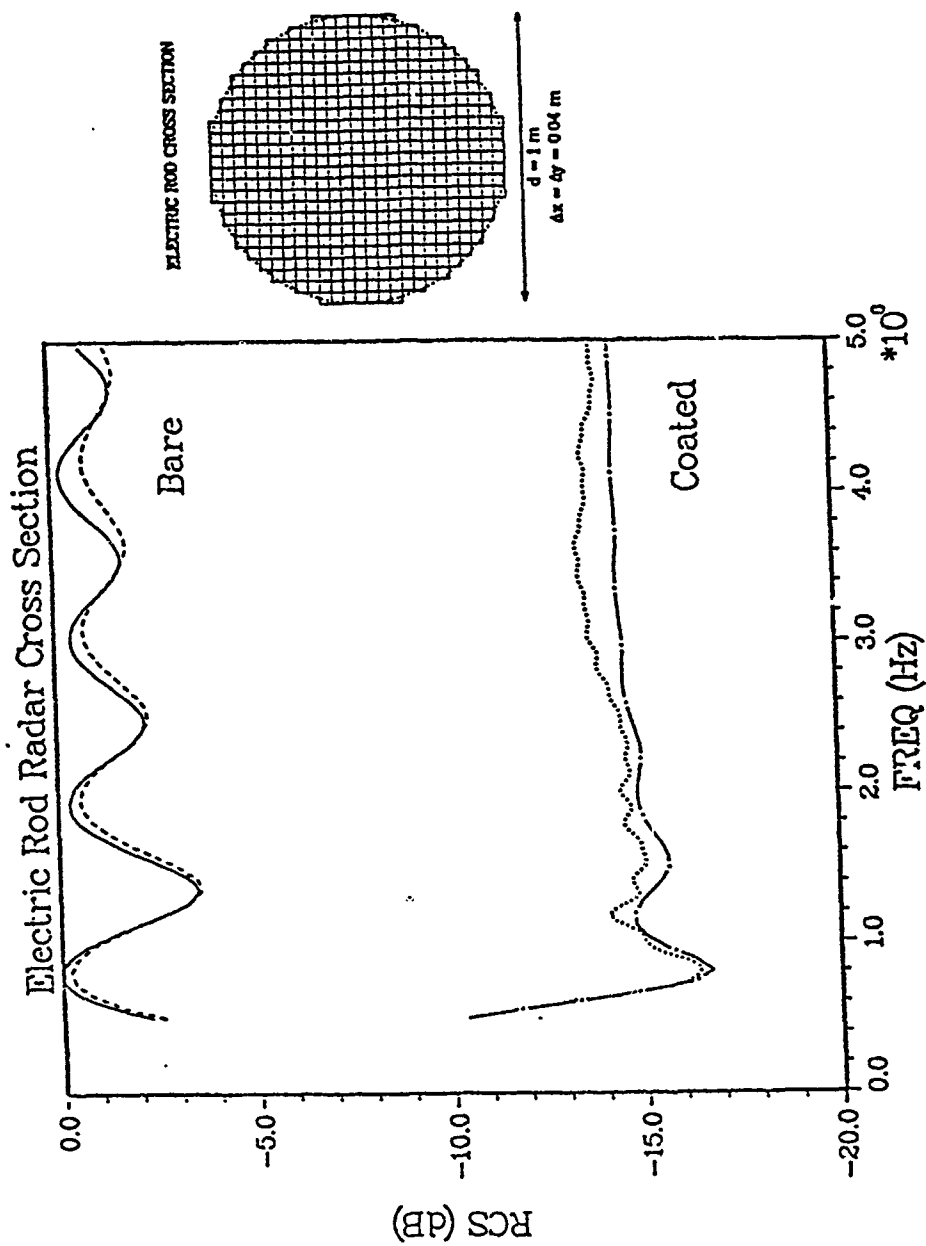


Figure 32. Monostatic RCS of bare and damped electrically conducting cylinders with \vec{E} transverse to cylinder axes. Plot is based on illumination at $\phi_{inc} = \pi/4$.

Scattering from a Thin Dielectric Strip

Richmond¹ has worked out a solution for scattering of a plane wave by an infinite dielectric strip. The strip may be of any width, but its optical thickness should not exceed a tenth of a wavelength.

This approximate solution is based on superimposing arbitrary combinations of the incident wave and the two zero-order waveguide modes a strip can support propagating in its width direction. The coefficients of the three waves are then optimized by a slight variation on Galerkin's method.

It is an intrinsic property of the Richmond solution that the total scattered current (conduction, displacement and Prony) is symmetric with respect to the center line of the strip's thickness dimension. Thus, bistatic cross-sections computed from this algorithm will always have a plane of symmetry coincident with the plane of the strip.

Two code-code comparisons have been run between the Richmond frequency-domain algorithm and our TDFD code. We first did a strip of $\epsilon_r = 2$ which was .04 m thick and 2 m wide. Cells .02 m square were used, so the TDFD model was 2 x 100 cells. Illumination at $\phi^{inc} = 45^\circ$ with the Poynting vector in the first quadrant was assumed. Monostatic RCS comparisons were performed from 50 MHz to 500 MHz, and bistatic RCS comparisons were performed at 250 MHz and 500 MHz.

Figure 33 shows the TDFD model. Figure 34 is a linear comparison of the monostatic result, and Figure 35 is a dB comparison. Figure 36 is a linear comparison of the bistatic result at 250 MHz, and Figure 37 is a dB comparison. Figures 38 and 39 are bistatic comparisons at 500 MHz.

The second comparison was a strip of $\epsilon_r = 9$ with .02 m thickness and 2 m width. Cells were again .02 m square, so the TDFD model was 1 x 100 cells. All other parameters were the same as for the first example. Figures 40 - 46 compare the same data for this case as Figures 33 - 39 did for the first example.

DIELECTRIC STRIP CROSS SECTION

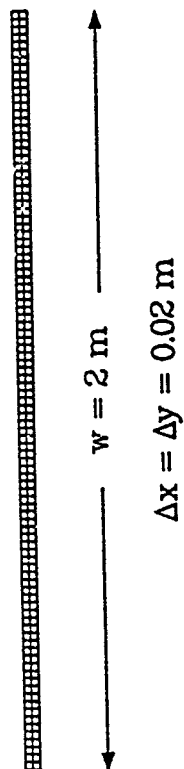


Figure 33. TDFD model of a dielectric strip .04 m \times 2 m in cross-section. Cells are .02 m square.

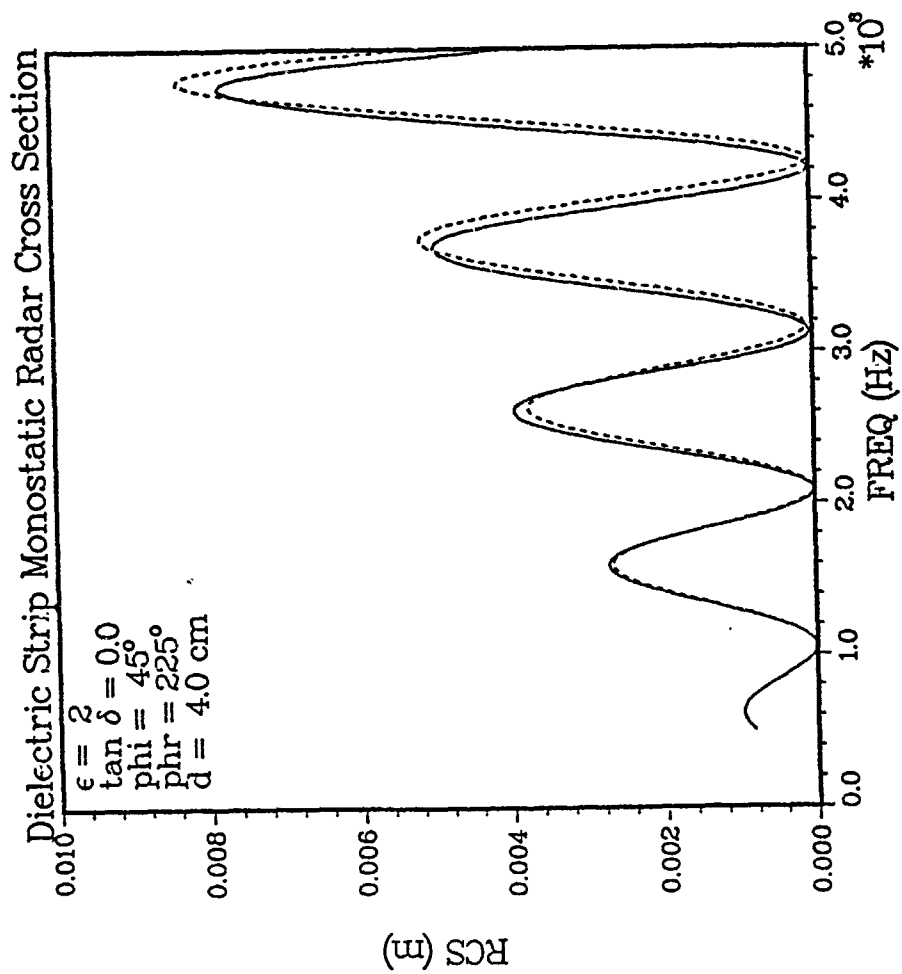


Figure 34. Monostatic RCS for the $\epsilon_r = 2$ dielectric strip. Solid curve is the Richmond result, and dashed line is the TDFD result. Plot is based on illumination at $\phi_{inc} = \pi/4$.

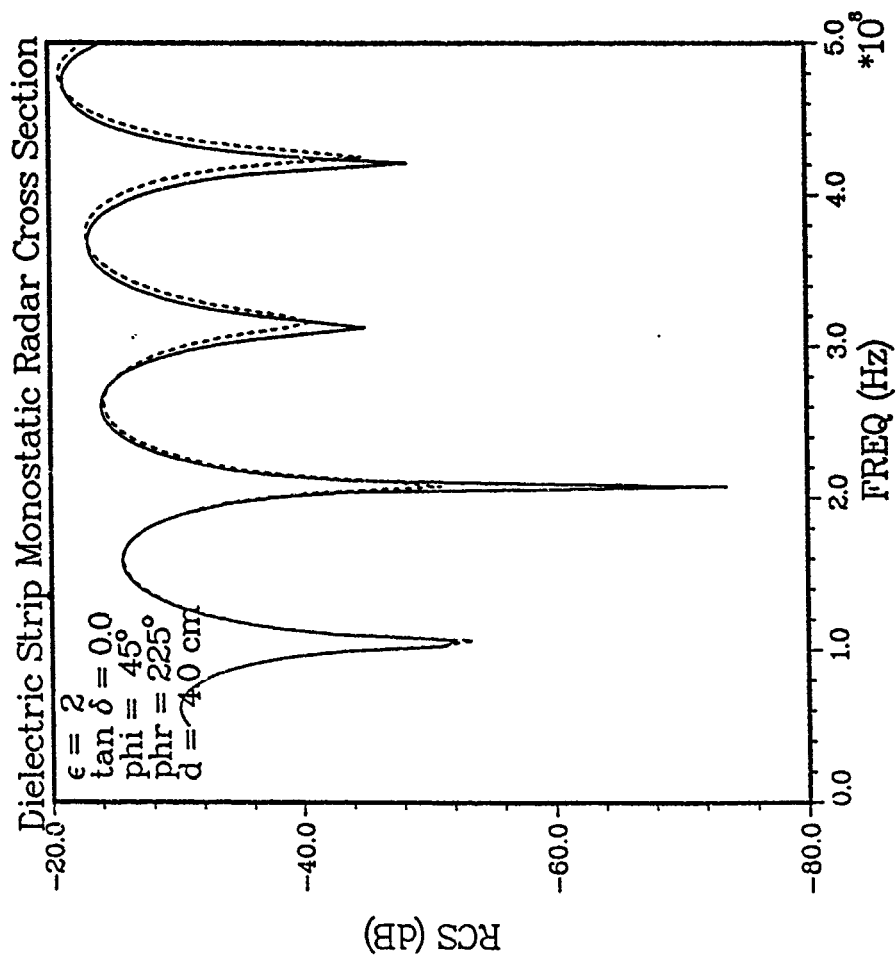


Figure 35. Monostatic RCS for the $\epsilon_r = 2$ dielectric strip.

Solid curve is the Richmond result, and dashed line is the TDFD result. Plot is based on illumination at $\phi_{inc} = \pi/4$.

Dielectric Strip Bistatic Radar Cross Section

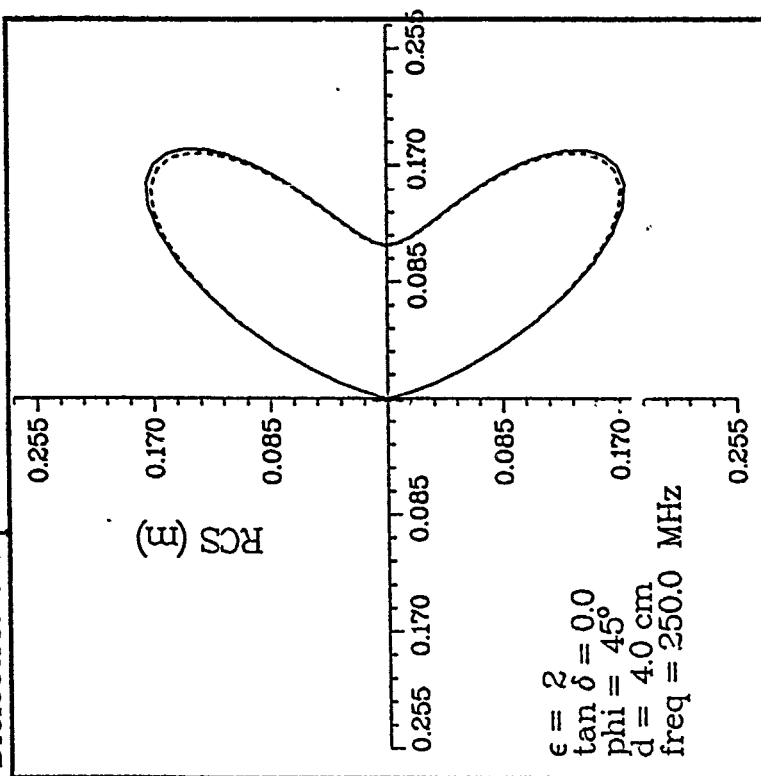


Figure 36. Bistatic RCS for the $\epsilon_r = 2$ dielectric strip at 250 MHz. Solid curve is the Richmond result, and dashed line is the TDFD result. Plot is based on illumination at $\phi_{\text{inc}} = \pi/4$.

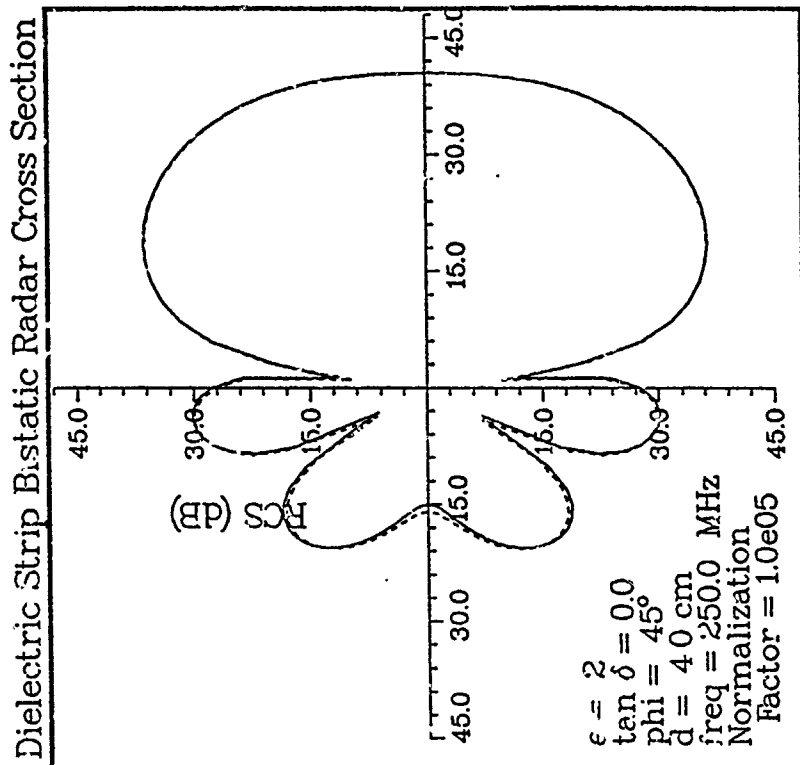


Figure 37. Bistatic RCS for the $\epsilon_r = 2$ dielectric strip at 250 MHz. Solid curve is the Richmond result, and dashed line is the TDFD result. Plot is based on illumination at $\phi_{\text{inc}} = \pi/4$.

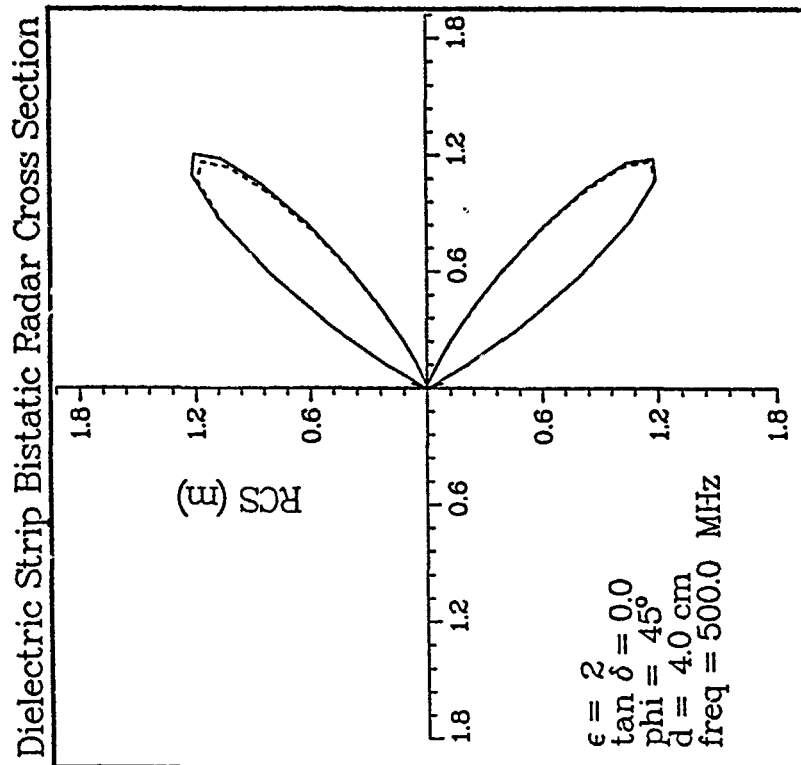


Figure 38. Bistatic RCS for the $\epsilon_r = 2$ dielectric strip at 500 MHz. Solid curve is the Richmond result, and dashed line is the TDFD result. Plot is based on illumination at $\phi_{\text{inc}} = \pi/4$.

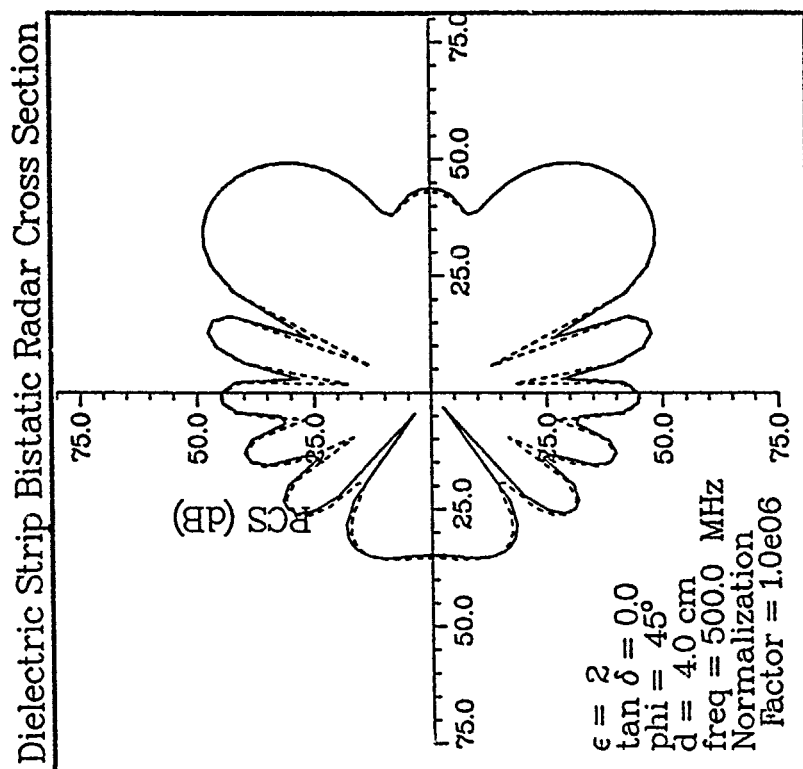


Figure 39. Bistatic RCS for the $\epsilon_r = 2$ dielectric strip at 500 MHz. Solid curve is the Richmond result, and dashed line is the TDFD result. Plot is based on illumination at $\phi_{\text{inc}} = \pi/4$.

DIELECTRIC STRIP CROSS SECTION

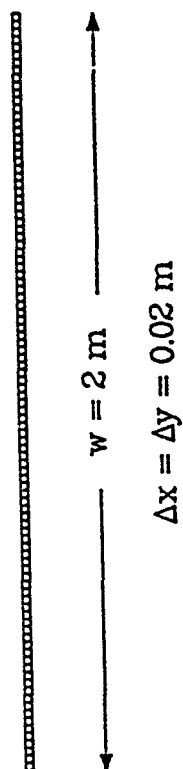


Figure 40. TDFD model of a dielectric strip $.02 \text{ m} \times 2 \text{ m}$ in cross-section. Cells are $.02 \text{ m}$ square.

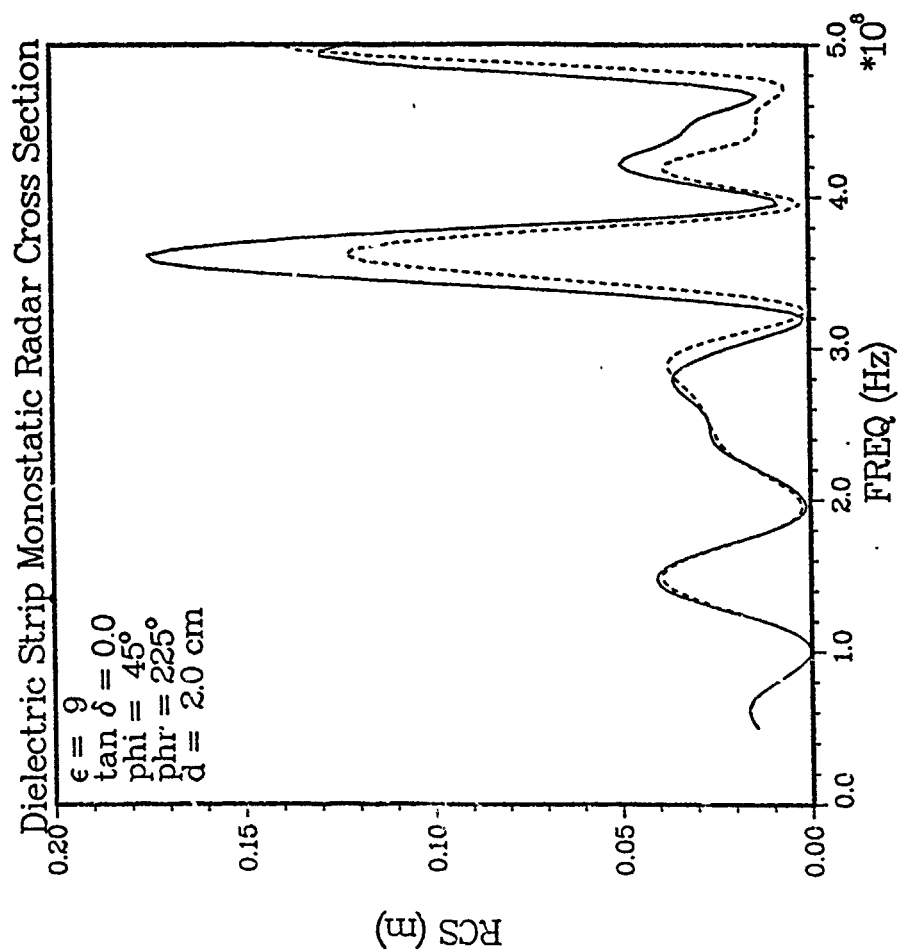


Figure 41. Monostatic RCS for the $\epsilon_r = 9$ dielectric strip. Solid curve is the Richmond result, and dashed line is the TDFD result. Plot is based on illumination at $\phi_{\text{inc}} = \pi/4$.

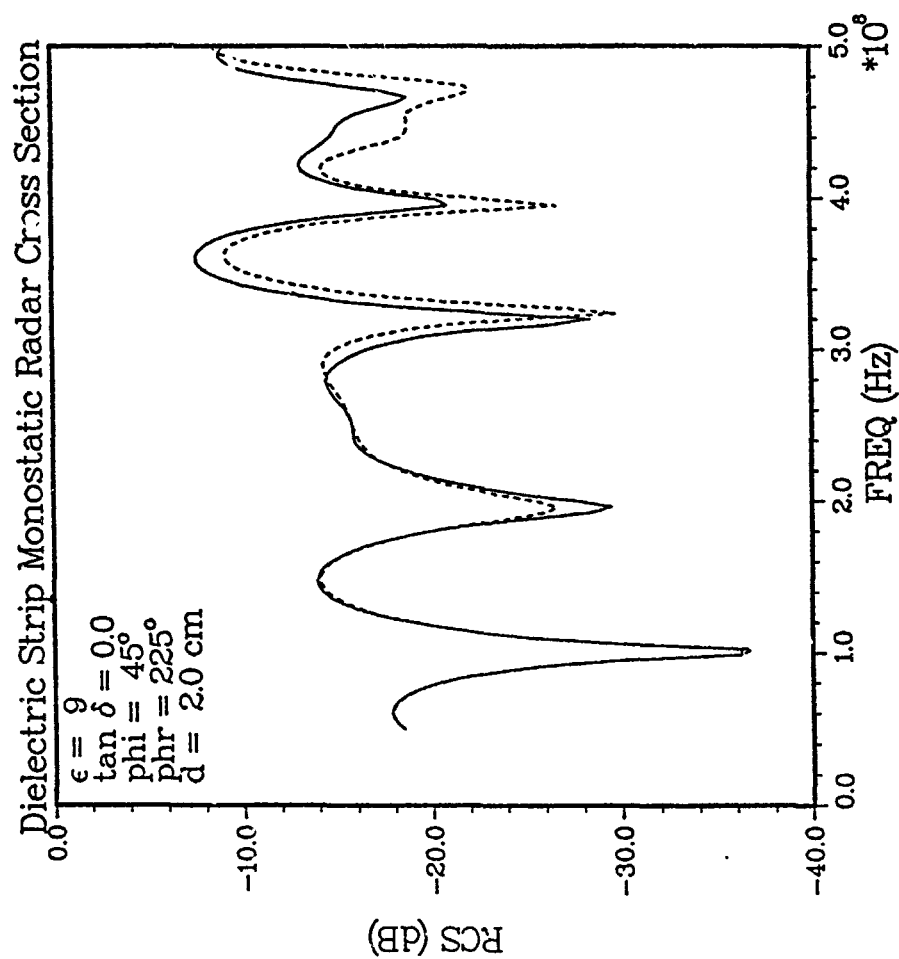


Figure 42. Monostatic RCS for the $\epsilon_r = 9$ dielectric strip. Solid curve is the Richmond result, and dashed line is the TDFD result. Plot is based on illumination at $\phi_{inc} = \pi/4$.

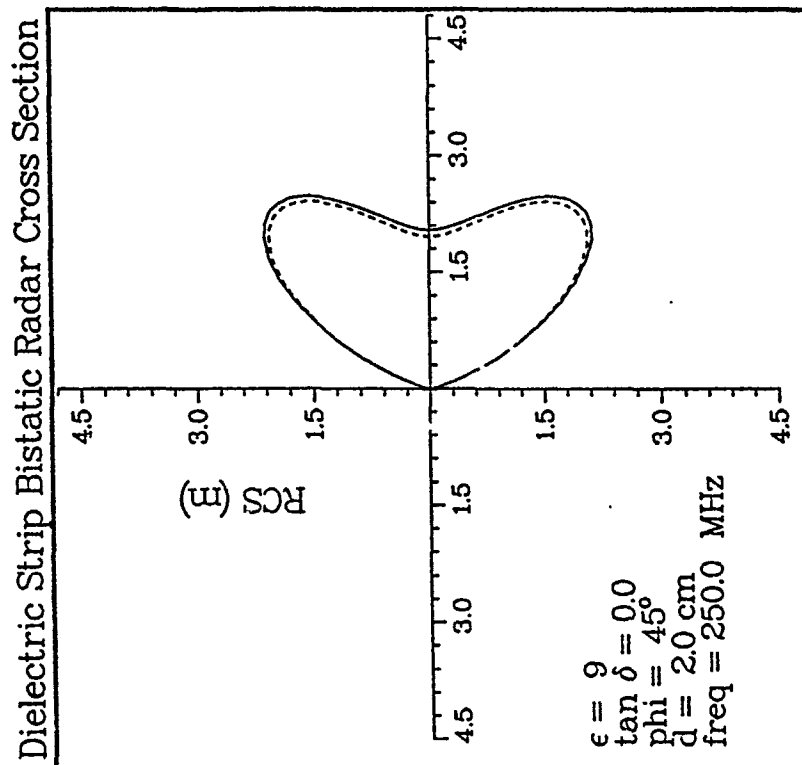


Figure 43. Bistatic RCS for the $\epsilon_r = 9$ dielectric strip at 250 MHz. Solid curve is the Richmond result, and dashed line is the TDFD result. Plot is based on illumination at $\phi_{\text{inc}} = \pi/4$.

Dielectric Strip Bistatic Radar Cross Section

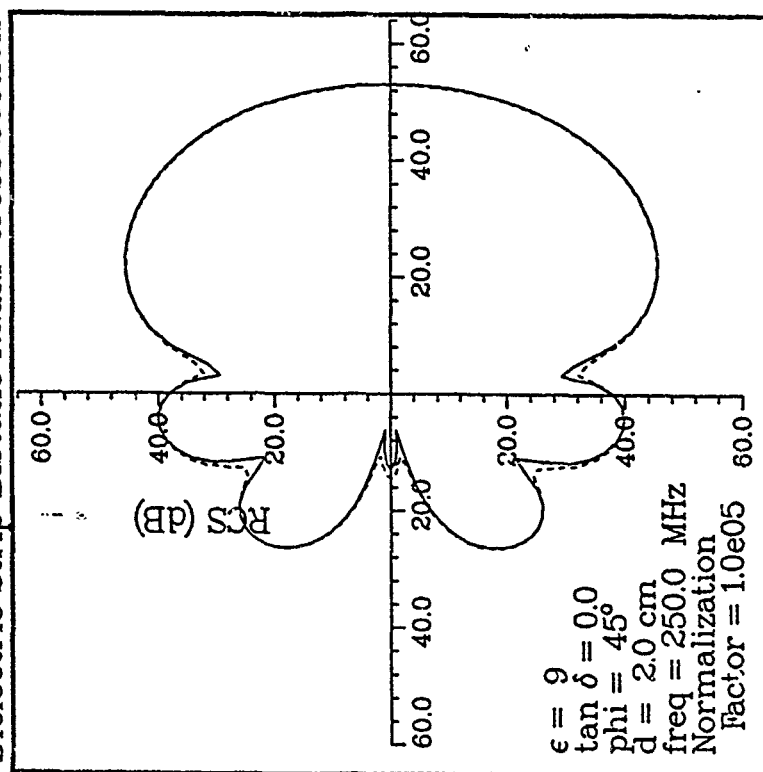


Figure 44. Bistatic RCS for the $\epsilon_r = 9$ dielectric strip at 250 MHz. Solid curve is the Richmond result, and dashed line is the TDFD result. Plot is based on illumination at $\phi_{\text{inc}} = \pi/4$.

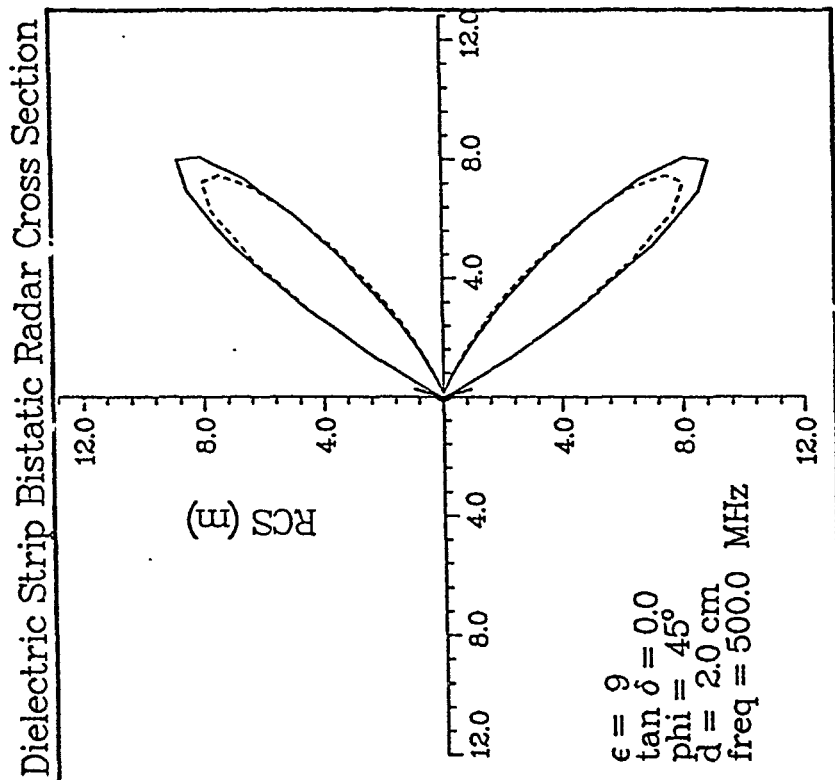


Figure 45. Bistatic RCS for the $\epsilon_r = 9$ dielectric strip at 500 MHz. Solid curve is the Richmond result, and dashed line is the TDFD result. Plot is based on illumination at $\phi_{\text{inc}} = \pi/4$.

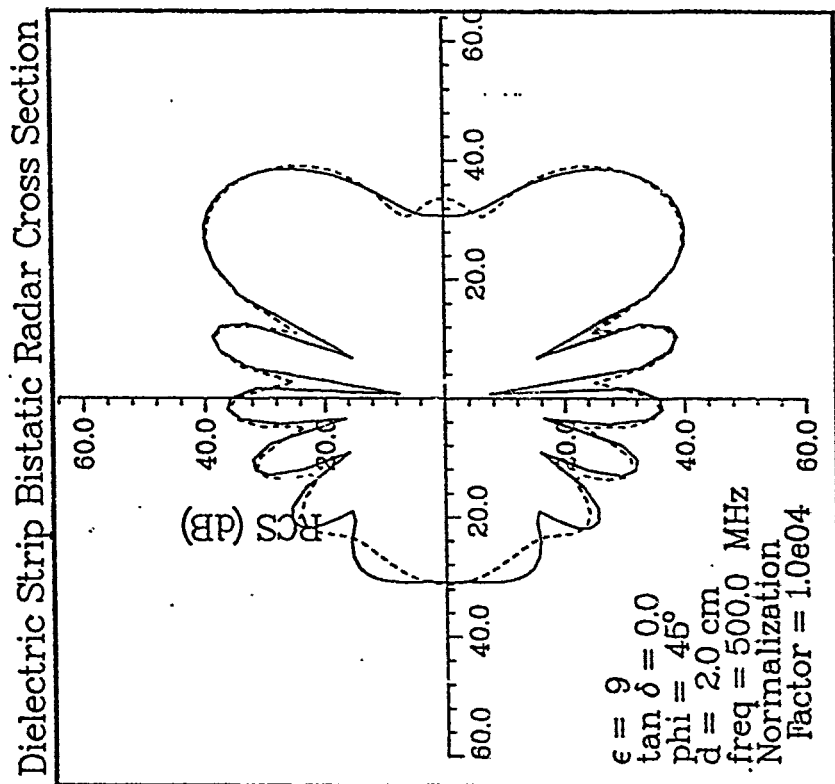


Figure 46. Bistatic RCS for the $\epsilon_r = 9$ dielectric strip at 500 MHz. Solid curve is the Richmond result, and dashed line is the TDFD result. Plot is based on illumination at $\phi_{\text{inc}} = \pi/4$.

It may again be seen that the two results are in excellent agreement for all frequencies in the $\epsilon_r = 2$ case, but that some discrepancies occur above 300 MHz in the $\epsilon_r = 9$ case. For instance, the $\epsilon_r = 9$ bistatic comparison at 500 MHz (Figure 46) again does not show particularly good agreement, especially at the minor lobes. To get really good finite-difference results, especially away from field maxima, we again see that a wavelength must be resolved into 16 segments.

The TDFD and frequency domain solutions are probably less discrepant here in Figure 46 than they were for the $\epsilon_r = 9$ dielectric rod at 500 MHz (Figure 15) because we are here only violating the 16 cells per wavelength rule in one direction. Figure 15 is based on a calculation where the rule was violated in two directions.

Elliptic Cylinder Scattering

The transformation from Cartesian to elliptic cylinder coordinates is

$$x = 1/2 d \cosh u \cos v \quad (1)$$

$$y = 1/2 d \sinh u \sin v \quad (2)$$

$$z = z \quad (3)$$

where d is the distance between the foci of the ellipse. Additionally, we sometimes denote

$$\xi = \cosh u \quad (4)$$

$$\eta = \cos v \quad (5)$$

so that

$$\sinh u = \sqrt{\xi^2 - 1} \quad (6)$$

In this section, we shall use the notation of Uslenghi and Zitran,² that of Blanch³ where it does not conflict with the first notation, and that of Stratton⁴ where it does not conflict with either of the above. (Lack of a standardized notation greatly compounds the inherently difficult problems associated with elliptic cylinder coordinates.)

For all cylindrical coordinate systems, the TM solution for H_z obeys

$$\nabla^2 H_z + k^2 H_z = 0 \quad (7)$$

In elliptic cylinder coordinates, this equation takes the form

$$\frac{1}{(d/2)^2 (\cosh^2 u - \cos^2 v)} \left(\frac{\partial^2 H_z}{\partial u^2} + \frac{\partial^2 H_z}{\partial v^2} \right) + \frac{\partial^2 H_z}{\partial z^2} + k^2 H_z = 0 \quad (8)$$

Let us now assume this equation can be solved by separation of variables,

$$H_z = U(u)V(v)Z(z) \quad (9)$$

Substitution of (9) in (8) yields

$$\frac{1}{(d/2)^2(\cosh^2 u - \cos^2 v)} \left(\frac{U''}{U} + \frac{V''}{V} \right) + \frac{Z''}{Z} + k^2 = 0 \quad (10)$$

Let C be the first separation constant,

$$\frac{Z''}{Z} + C = 0 \quad (11)$$

Then U and V must obey

$$U'' - (a - 1/8 \cdot d^2(k^2 - C) \cosh 2u)U = 0 \quad (12)$$

$$V'' + (a + 1/8 \cdot d^2(k^2 - C) \cos 2v)V = 0 \quad (13)$$

where a is the second separation constant.

In the rest of this report, we shall assume there is no z dependence, so

$$k^2 - C \rightarrow k^2 \quad (14)$$

and we shall denote

$$c = 1/2 \cdot (kd) \quad (15)$$

where c is not the speed of light, but is the number of radians at the frequency of interest between the ellipse center and one of its foci. Then eqs. (12) and (13) become

$$U'' - (a - 1/2 \cdot c^2 \cosh 2u)U = 0 \quad (16)$$

$$V'' + (a + 1/2 \cdot c^2 \cos 2u)V = 0 \quad (17)$$

Equation (17) is Mathieu's equation and (16) is the modified Mathieu equation.

The c of eqs. (15) - (17) corresponds to $c_0 \lambda$ in Stratton and \sqrt{s} in Blanch. In some more modern works, such as Abramowitz and Stegun,⁵ and Hodge,⁶ it corresponds to $2/q$.

It turns out that Mathieu's equation only permits periodic solutions for discrete eigenvalues of a , where these eigenvalues depend on c . If we assume

$$V = \sum_{k=0}^{\infty} D e_{2k}(c) \cos 2kv \quad (18)$$

we obtain even solutions of period π . The r th eigenvalue of this equation is denoted a^{2r} , and the r th eigenfunction is denoted

$$V = \sum_{k=0}^{\infty} D e_{2k}^{2r}(c) \cos 2kv \quad (19)$$

If we normalize these functions to be unity at $v = 0$, we obtain the even Mathieu functions of period π

$$Se_{2r}(c, \eta) = \sum_{k=0}^{\infty} De_{2k}^{2r}(c) \cos 2kv \quad (20)$$

Alternatively, if we let

$$V = \sum_{k=0}^{\infty} De_{2k+1}(c) \cos(2k+1)v \quad (21)$$

we obtain the even solutions of period 2π . The r th eigenfunction of this system, also normalized to be unity at $v = 0$, is

$$Se_{2r+1}(c, \eta) = \sum_{k=0}^{\infty} De_{2k+1}^{2r+1}(c) \cos(2k+1)v \quad (22)$$

Now let us consider odd solutions of period π ,

$$V = \sum_{k=1}^{\infty} Do_{2k}(c) \sin 2kv \quad (23)$$

The r th eigenvalue of this equation is denoted b^{2r} and the r th eigenfunction, normalized to have unity derivative at $v = 0$ is

$$S_{0,2r}(c, \eta) = \sum_{k=1}^{\infty} D_{2k}^{2r}(c) \sin 2kv \quad (24)$$

Finally, the r th odd eigenfunction of period 2π is

$$S_{0,2r+1}(c, \eta) = \sum_{k=0}^{\infty} D_{2k+1}^{2r+1}(c) \sin(2k+1)v \quad (25)$$

Any even Mathieu function is orthogonal to any odd Mathieu function on the interval $(0, 2\pi)$. Likewise, different even or odd Mathieu functions are orthogonal. The normalization factors are

$$\begin{aligned} N_{2r}^{(e)}(c) &= \int_0^{2\pi} S_{0,2r}(c, \cos v)^2 dv \\ &= \pi \left[2(D_{0,2r}^{2r}(c))^2 + (D_{2,2r}^{2r}(c))^2 + \dots \right] \end{aligned} \quad (26)$$

$$N_{2r+1}^{(e)}(c) = \pi \sum_{k=0}^{\infty} (D_{2k+1}^{2r+1}(c))^2 \quad (27)$$

$$N_{2r}^{(o)}(c) = \pi \sum_{k=1}^{\infty} (D_{2k}^{2r}(c))^2 \quad (28)$$

$$N_{2r+1}^{(o)}(c) = \pi \sum_{k=0}^{\infty} (D_{2k+1}^{2r+1}(c))^2 \quad (29)$$

The four types of Mathieu functions defined by eqs. (17) - (29) describe the azimuthal dependence of the elliptic-cylinder harmonics. Equation (16), on the other hand, describes the radial dependence. There are a total of 16 kinds of radial Mathieu functions.

Let $Z_k^{(j)}(x)$ denote the k th Bessel function of the j th kind. For example,

$$Z_k^{(3)}(x) = J_k(x) + iY_k(x) \quad (30)$$

Then the four radial Mathieu functions corresponding to $Se_{2r}(c, \eta)$ may be shown^{4,5} to be

$$Re_{2r}^{(j)}(c, \xi) = \sqrt{\frac{\pi}{2}} \sum_{k=0}^{\infty} \frac{(-1)^{r+k} Se_{2k}^{2r}(c)}{\epsilon_s De_{2s}^{2r}(c)} \cdot [J_{k-r}(\xi_1) Z_{k+s}^{(j)}(\xi_2) + J_{k+s}(\xi_1) Z_{k-s}^{(j)}(\xi_2)] \quad (31)$$

where

$$\epsilon_0 = 2; \epsilon_s = 1 \text{ for } s = 1, 2, \dots \quad (32)$$

$$\xi_1 = (c/2)e^{-u} \quad (33)$$

$$\xi_2 = (c/2)e^u \quad (34)$$

and s is any arbitrary integer, but is best selected if

$$De_{2s}^{2r}(c) = \max_k (De_{2k}^{2r}(c)) \quad (35)$$

Similarly, the four radial Mathieu functions corresponding to $Se_{2r+1}(c, \eta)$ are

$$Re_{2r+1}^{(j)}(c, \xi) = \sqrt{\frac{\pi}{2}} \sum_{k=0}^{\infty} (-1)^{r+k} \frac{De_{2k+1}^{2r+1}(c)}{De_{2s+1}^{2r+1}(c)} \cdot$$

$$\left[J_{k-s}(\xi_1) Z_{k+s+1}^{(j)}(\xi_2) + J_{k+s+1}(\xi_1) Z_{k-s}^{(j)}(\xi_2) \right] \quad (36)$$

The radial Mathieu functions corresponding to $So_{2r+p}(c, \eta)$ are

$$Ro_{2r}^{(j)}(c, \xi) = \sqrt{\frac{\pi}{2}} \sum_{k=1}^{\infty} (-1)^{r+k} \frac{Do_{2k}^{2r}(c)}{Do_{2s}^{2r}(c)} \cdot$$

$$\left[J_{k-s}(\xi_1) Z_{k+s}^{(j)}(\xi_2) - J_{k+s}(\xi_1) Z_{k-s}^{(j)}(\xi_2) \right] \quad (37)$$

$$Ro_{2r+1}^{(j)}(c, \xi) = \sqrt{\frac{\pi}{2}} \sum_{k=1}^{\infty} (-1)^{r+k} \frac{Do_{2k+1}^{2r+1}(c)}{Do_{2s+1}^{2r+1}(c)} \cdot$$

$$\left[J_{k-s}(\xi_1) Z_{k+s+1}^{(j)}(\xi_2) - J_{k+s+1}(\xi_1) Z_{k-s}^{(j)}(\xi_2) \right] \quad (38)$$

Let us now consider the expansion of a plane wave in elliptic-cylinder harmonics. If we have a plane wave propagating at an angle ϕ^{inc} from the + x axis,

$$\underline{H}^{inc} = \underline{i}_z Y_0 e^{i(kx \cos \phi^{inc} + ky \sin \phi^{inc})} \quad (39)$$

then the desired expansion is⁴

$$\begin{aligned} \underline{H}^{inc} = \underline{i}_z Y_0 & \left[\sum_{m=0}^{\infty} a_m^{inc} \text{Re}_m^{(1)}(c, \xi) \text{Se}_m(c, \eta) \right. \\ & \left. + \sum_{m=1}^{\infty} b_m^{inc} \text{Ro}_m^{(1)}(c, \xi) \text{So}_m(c, \eta) \right] \end{aligned} \quad (40)$$

where

$$a_m^{inc} = \sqrt{8\pi} \frac{i^m}{N_m^{(e)}} \text{Se}_m(c, \cos \phi^{inc}) \quad (41)$$

$$b_m^{inc} = \sqrt{8\pi} \frac{i^m}{N_m^{(o)}} \text{So}_m(c, \cos \phi^{inc}) \quad (42)$$

The associated electric field is

$$\underline{E}^{inc} = \frac{-1}{i\omega\epsilon h} \left(\underline{i}_u \frac{\partial H_z^{inc}}{\partial v} - \underline{i}_v \frac{\partial H_z^{inc}}{\partial u} \right) \quad (43)$$

where h is the elliptic cylinder metric

$$h = h_u = h_v = (d/2)(\cosh^2 u - \cos^2 v)^{1/2} \quad (44)$$

Expansion of eq. (43) yields

$$\begin{aligned}
 \underline{E}^{inc} = & -\frac{k}{ih} \left[\underline{i}_u \left[\sum_{m=0}^{\infty} a_m^{inc} Re_m^{(1)}(c, \xi) Se_m'(c, \xi) \right. \right. \\
 & + \left. \sum_{m=1}^{\infty} b_m^{inc} Ro_m^{(1)}(c, \xi) So_m'(c, \eta) \right] \\
 & - \underline{i}_v \left[\sum_{m=0}^{\infty} a_m^{inc} Re_m^{(1)'}(c, \xi) Se_m(c, \eta) \right. \\
 & + \left. \left. \sum_{m=1}^{\infty} b_m^{inc} Ro_m^{(1)'}(c, \xi) So_m(c, \eta) \right] \right] \quad (45)
 \end{aligned}$$

We shall first assume this plane wave is scattered by a perfectly conducting elliptic cylinder. Thus, the scattered solution must be an infinite series of outgoing Mathieu-Hankel functions.

$$\begin{aligned}
 \underline{H}^{scat} = & \underline{i}_z Y_0 \left[\sum_{m=0}^{\infty} a_m^{scat} Re_m^{(3)}(c, \xi) Se_m(c, \eta) \right. \\
 & + \left. \sum_{m=1}^{\infty} b_m^{scat} Ro_m^{(3)}(c, \xi) So_m(c, \eta) \right] \quad (46)
 \end{aligned}$$

$$\begin{aligned}
E^{\text{scat}} = & - \frac{k}{ih} \left[\frac{i}{u} \left[\sum_{m=0}^{\infty} a_m^{\text{scat}} R_o^{(3)}(c, \xi) S_e'(c, \eta) \right. \right. \\
& + \left. \sum_{m=1}^{\infty} b_m^{\text{scat}} R_o^{(3)}(c, \xi) S_o'(c, \eta) \right] \\
& - \frac{i}{v} \left[\sum_{m=0}^{\infty} a_m^{\text{scat}} R_e^{(3)'}(c, \xi) S_e(c, \eta) \right. \\
& + \left. \sum_{m=1}^{\infty} b_m^{\text{scat}} R_o^{(3)'}(c, \xi) S_o'(c, \eta) \right] \quad (47)
\end{aligned}$$

The requirement that on $\xi = \xi_1$

$$E_v^{\text{inc}} + E_v^{\text{scat}} = 0 \quad (48)$$

then yields formulas for a_m^{scat} and b_m^{scat} :

$$a_m^{\text{scat}} = - \sqrt{8\pi} \frac{i^m}{N_m^{(e)}} \frac{R_e^{(1)'}(c, \xi_1)}{R_e^{(3)'}(c, \xi_1)} S_e(c, \cos \phi^{\text{inc}}) \quad (49)$$

$$b_m^{\text{scat}} = - \sqrt{8\pi} \frac{i^m}{N_m^{(o)}} \frac{R_o^{(1)'}(c, \xi_1)}{R_o^{(3)'}(c, \xi_1)} S_o(c, \cos \phi^{\text{inc}}) \quad (50)$$

We are now in possession of enough information to evaluate the RCS of the elliptic cylinder. At large arguments, $Re_m^{(3)}(c, \xi)$ and $Ro_m^{(3)}(c, \xi)$ both approach⁴

$$Re_m^{(3)}(c, \xi) \rightarrow \frac{1}{\sqrt{c\xi}} e^{i(c\xi - \frac{2m+1}{4}\pi)}$$

$$= \frac{1}{\sqrt{c \cosh u}} e^{i(c \cosh u - \frac{2m+1}{4}\pi)\pi} \quad (51)$$

Uslenghi and Zitran² then define the scattering function

$$P(v'_p) = \sqrt{\frac{\pi k r'_p}{2}} e^{i(kr'_p - \pi/4)} H_z^{\text{scat}}(r'_p, v'_p) \quad (52)$$

where v'_p approaches ϕ'_p at large r'_p . In view of eqs. (1), (2), and (15), we can show that

$$kr'_p \rightarrow c \cosh u \quad (53)$$

Substitution of (46), (49) - (51), and (53) into (52) then yields the bistatic scattering function.

$$P(v'_p) = -2\pi \left[\sum_{m=0}^{\infty} \frac{1}{N_m^{(e)}} \frac{Re_m^{(1)'}(c, \xi_1)}{Re_m^{(3)'}(c, \xi_1)} Se_m(c, \cos \phi^{\text{inc}}) Se_m(c, \cos v'_p) \right.$$

$$\left. + \sum_{m=1}^{\infty} \frac{1}{N_m^{(o)}} \frac{Ro_m^{(1)'}(c, \xi_1)}{Ro_m^{(3)'}(c, \xi_1)} So_m(c, \cos \phi^{\text{inc}}) So_m(c, \cos v'_p) \right] \quad (54)$$

We can then evaluate the bistatic RCS,

$$\begin{aligned} \text{RCS}(\mathbf{v}'_p) &= 2\pi \frac{|H_z^{\text{scat}}(\mathbf{r}'_p, \mathbf{v}'_p) \sqrt{r'_p}|^2}{|H_z^{\text{inc}}|^2} \\ &= \frac{4 |P(\mathbf{v}'_p)|^2}{k} \end{aligned} \quad (55)$$

Uslenghi and Zitran² have published curves for $|P(\mathbf{v}'_p)|^2$ as functions of ϕ^{inc} , $c\xi_1$ and $\tanh u_1$. The quantity

$$c\xi_1 = (1/2) \cdot kd \cosh u_1 \quad (56)$$

is the number of free space radians at the frequency of interest along one half of the major axis of the ellipse.

Additionally,

$$\tanh u_1 = \sqrt{\xi_1^2 - 1}/\xi_1 \quad (57)$$

is zero if the ellipse is reduced to a conducting strip, and is unity in the special case where the ellipse fattens to a circular cylinder.

Figures 47 - 49 illustrate our results for $|P(\mathbf{v}'_p)|^2$ when ϕ^{inc} is $0, \pi/4$ and $\pi/2$ and \mathbf{v}'_p is $\phi^{\text{inc}} + \pi$ (the backscatter case). These figures agree exactly with previously published results² and confirm the correctness of our analysis and Mathieu function routines.

We have also reproduced the Uslenghi and Zitran² results for TE scattering by an elliptic cylinder, although this calculation is only relevant

NORMALIZED RADAR CROSS SECTION OF AN ELLIPTIC CYLINDER

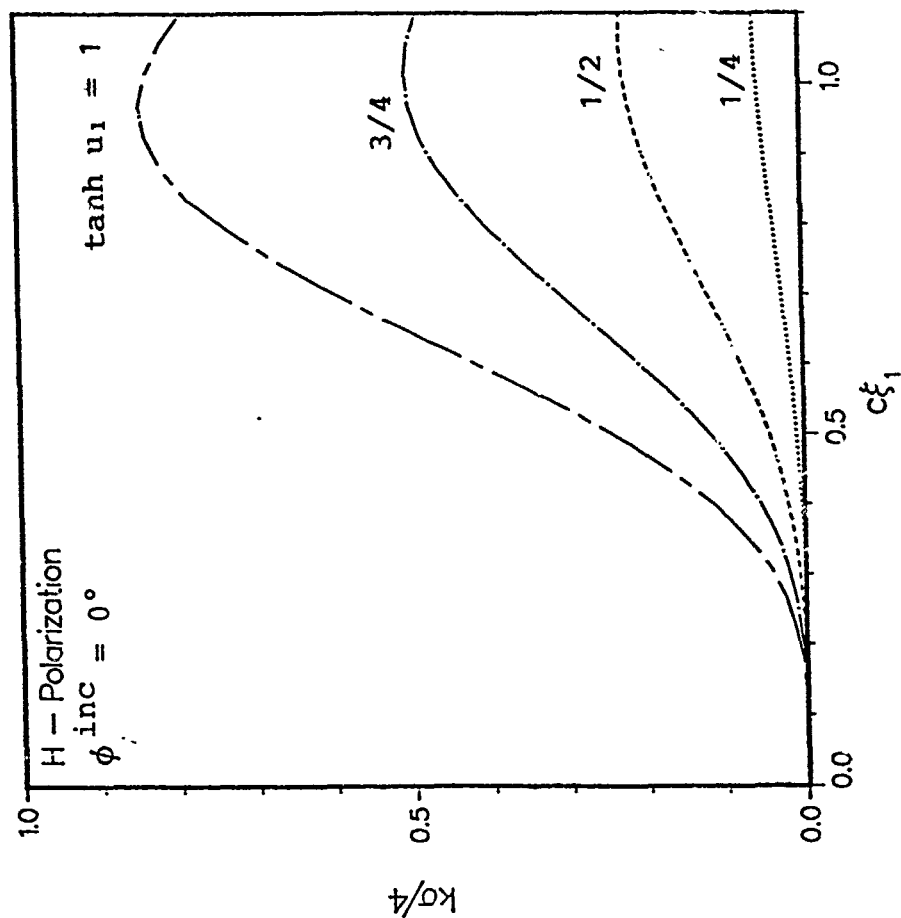


Figure 47. Monostatic RCS for a perfectly conducting elliptic cylinder when illuminated with H parallel to the cylinder axis at $\phi_{inc} = 0$.

NORMALIZED RADAR CROSS SECTION OF AN ELLIPTIC CYLINDER

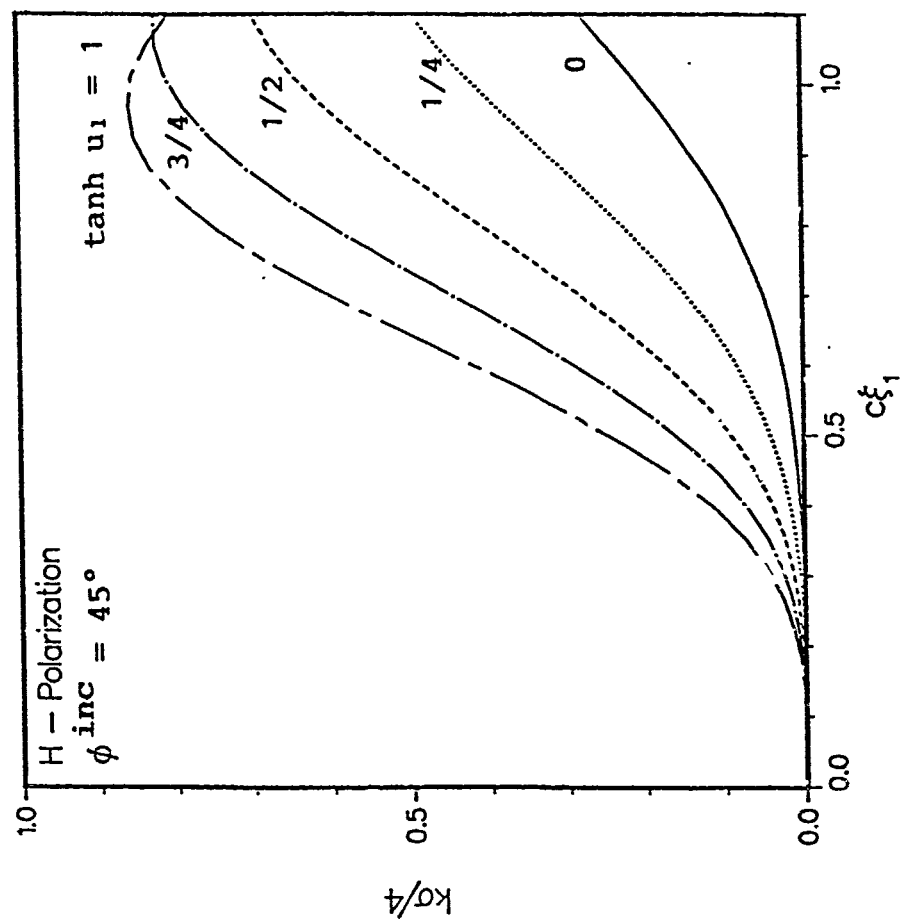


Figure 48. Monostatic RCS for a perfectly conducting elliptic cylinder when illuminated with H parallel to the cylinder axis at $\phi_{\text{inc}} = \pi/4$.

NORMALIZED RADAR CROSS SECTION OF AN ELLIPTIC CYLINDER

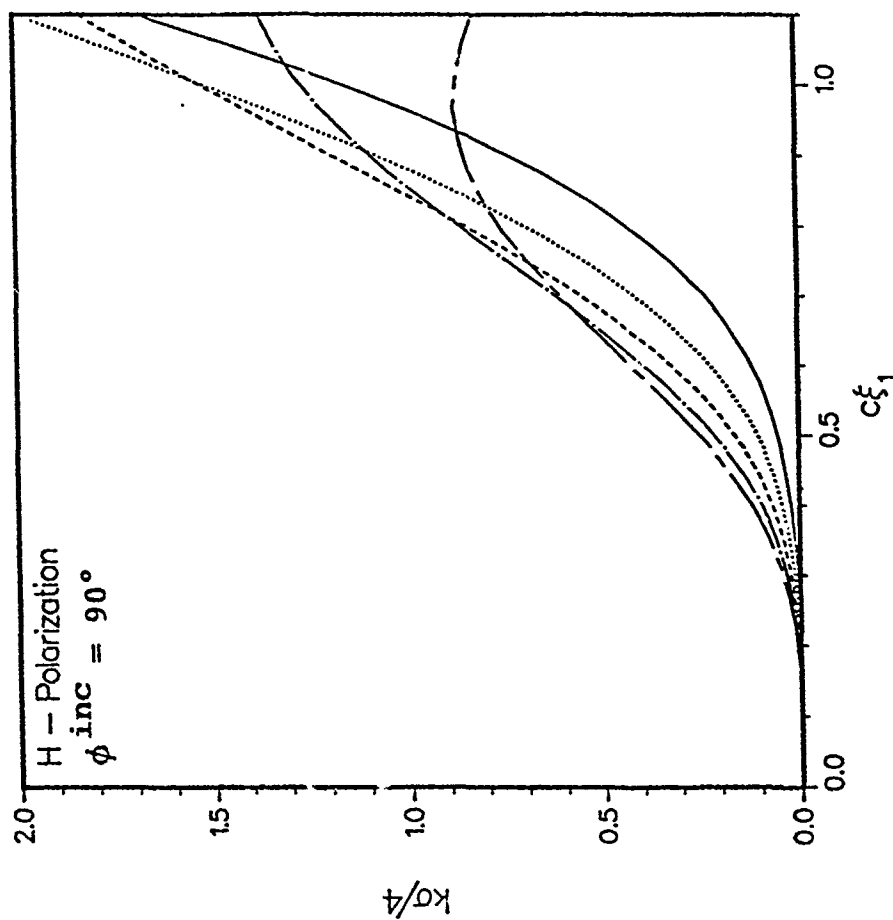


Figure 49. Monostatic RCS for a perfectly conducting elliptic cylinder when illuminated with H parallel to the cylinder axis at $\phi^{inc} = \pi/2$.

to our present work in that it tests our Mathieu function routines under different circumstances.

It is interesting to note that in the case of scattering by a conducting strip, u_1 is zero, ξ_1 is unity, $\text{Re}_m^{(1)'}(c, 1)$ is zero, and all the a_m^{scat} vanish.

For scattering by a dielectric cylinder, we encounter a strange complication which will probably be new to anyone who has previously only used Bessel functions and spherical harmonics. The incident and scattered fields can still be represented by eqs. (40) - (47). However, we must now also consider the fields which penetrate the cylinder,

$$\begin{aligned} \underline{H}^{\text{trans}} = & \underline{i}_z Y_1 \left[\sum_{m=0}^{\infty} a_m^{\text{trans}} \text{Re}_m^{(1)}(c_1, \xi) \text{Se}_m(c_1, \eta) \right. \\ & \left. + \sum_{m=1}^{\infty} b_m^{\text{trans}} \text{Ro}_m^{(1)}(c_1, \xi) \text{So}_m(c_1, \eta) \right] \end{aligned} \quad (58)$$

$$\begin{aligned} \underline{E}^{\text{trans}} = & - \frac{k_1}{ih} \left[\underline{i}_u \left[\sum_{m=0}^{\infty} a_m^{\text{trans}} \text{Re}_m^{(1)}(c_1, \xi) \text{Se}_m'(c_1, \eta) \right. \right. \\ & \left. \left. + \sum_{m=1}^{\infty} b_m^{\text{trans}} \text{Ro}_m^{(1)}(c_1, \xi) \text{So}_m'(c_1, \eta) \right] \right. \\ & \left. - \underline{i}_v \left[\sum_{m=0}^{\infty} a_m^{\text{trans}} \text{Re}_m^{(1)'}(c_1, \xi) \text{Se}_m(c_1, \eta) \right. \right. \end{aligned}$$

$$+ \left. \sum_{m=1}^{\infty} b_m^{\text{trans}} R_o_m^{(1)'}(c_1, \xi) S_o_m(c_1, \eta) \right] \quad (59)$$

Here Y_1 is the characteristic admittance of the dielectric

$$Y_1 = \sqrt{\epsilon_1 / \mu_0} \quad (60)$$

k_1 is the wavenumber in the dielectric

$$k_1 = \omega \sqrt{\epsilon_1 \mu_0} \quad (61)$$

and c_1 is the number of radians between the ellipse center and a foci for a wave travelling in the dielectric,

$$c_1 = (1/2) \cdot k_1 d \quad (62)$$

The boundary conditions at $\xi = \xi_1$ are now the continuity of H_z and E_v ,

$$H_z^{\text{inc}} + H_z^{\text{scat}} = H_z^{\text{trans}} \quad (63)$$

$$E_v^{\text{inc}} + E_v^{\text{scat}} = E_v^{\text{trans}} \quad (64)$$

These conditions lead to the relationships

$$Y_0 \sum_{m=0}^{\infty} (a_m^{\text{inc}} R_e_m^{(1)}(c, \xi_1) + a_m^{\text{scat}} R_e_m^{(3)}(c, \xi_1)) S_e_m(c, \eta)$$

$$= Y_1 \sum_{m=0}^{\infty} a_m^{\text{trans}} \text{Re}_m^{(1)}(c_1, \xi_1) \text{Se}_m(c_1, \eta) \quad (65)$$

$$k \sum_{m=0}^{\infty} (a_m^{\text{inc}} \text{Re}_m^{(1)'}(c, \xi_1) + a_m^{\text{scat}} \text{Re}_m^{(3)'}(c, \xi_1)) \text{Se}_m(c, \eta)$$

$$= k \sum_{m=0}^{\infty} a_m^{\text{trans}} \text{Re}_m^{(1)'}(c_1, \xi_1) \text{Se}_m(c_1, \eta) \quad (66)$$

plus an additional pair of relationships connecting the odd elliptic harmonics.

The complication now arising is that $\text{Se}_m(c, \eta)$ and $\text{Se}_m(c_1, \eta)$ are not equal, since c and c_1 are different. In other words, the dielectric cylinder causes each incident elliptic harmonic to couple to every scattered elliptic harmonic. Thus, unlike the case for a circular cylinder or a sphere, eqs (65) and (66) do not separate out into decoupled equation pairs for each value of m .

It is necessary to substitute eqs. (20) and (22) for $\text{Se}_m(c, \eta)$ and $\text{Se}_m(c_1, \eta)$ into (65) and (66). Doing this, rearranging terms, and factoring out the trigonometric functions yields

$$\begin{aligned} \sum_{m=0}^{\infty} a_m^{\text{scat}} Y_0 \text{De}_m^n(c) \text{Re}_m^{(3)}(c, \xi_1) &= \sum_{m=0}^{\infty} a_m^{\text{trans}} Y_1 \text{De}_m^n(c_1) \text{Re}_m^{(1)}(c_1, \xi_1) \\ &= \sum_{m=0}^{\infty} a_m^{\text{inc}} Y_0 \text{De}_m^n(c) \text{Re}_m^{(1)}(c, \xi_1) \end{aligned} \quad (67)$$

$$\begin{aligned}
\sum_{m=0}^{\infty} a_m^{\text{scat}} c_1 \text{Re}_m^n(c) \text{Re}_m^{(3)'}(c, \xi_1) &= \sum_{m=0}^{\infty} a_m^{\text{trans}} c_1 \text{De}_m^n(c_1) \text{Re}_m^{(1)'}(c_1, \xi_1) \\
&= \sum_{m=0}^{\infty} a_m^{\text{inc}} c \text{De}_m^n(c) \text{Re}_m^{(1)'}(c, \xi_1)
\end{aligned} \tag{68}$$

These equations must be satisfied for all n , as must a similar family of equations for the odd elliptic harmonic. Once such a solution has been performed, the RCS is still given by eqs. (46) - (55). We have not yet programmed this solution, but certainly have all the necessary bits and pieces of Mathieu programs on the shelf, and could quickly assemble them.

The two-medium elliptic cylinder problem is a fairly straightforward extension of eqs. (67) and (68). Unlike Bessel functions of the second kind, radial Mathieu functions of the second kind do not go to infinity at $u = 0$. However, they do have both nonzero values and nonzero derivatives there. This means elliptic-cylinder harmonics with radial Mathieu functions of the second kind have either a sharp ridge or a step discontinuity on the line connecting the coordinate system foci. Consequently, their appearance is forbidden in the case of scattering from a uniform single-medium elliptic cylinder. Such is not the case, however, for the outer medium in the two-medium case.

Subject to this understanding, the elliptical-cylinder harmonic coefficients for the two-medium cylinder obey

$$\begin{aligned}
\sum_{m=0}^{\infty} (a_m^{\text{outer}(1)} y_2 \text{Re}_m^{(1)}(c_2, \xi_1) + a_m^{\text{outer}(2)} y_2 \text{Re}_m^{(2)}(c_2, \xi_1)) \text{De}_m^n(c_2) \\
= \sum_{m=0}^{\infty} a_m^{\text{inner}} y_1 \text{Re}_m^{(1)}(c_1, \xi_1) \text{De}_m^n(c_1)
\end{aligned} \tag{69}$$

$$\sum_{m=0}^{\infty} (a_m^{\text{outer}(1)} c_2 \text{Re}_m^{(1)'}(c_2, \xi_1) + a_m^{\text{outer}(2)} c_2 \text{Re}_m^{(2)'}(c_2, \xi_1)) \text{De}_m^n(c_2) \\ = \sum_{m=0}^{\infty} a_m^{\text{inner}} c_1 \text{Re}_m^{(1)'}(c_1, \xi_1) \text{De}_m^n(c_1) \quad (70)$$

$$\sum_{m=0}^{\infty} (a_m^{\text{inc}} y_0 \text{Re}_m^{(1)}(c, \xi_2) + a_m^{\text{scat}} y_0 \text{Re}_m^{(3)}(c, \xi_2)) \text{De}_m^n(c) \\ = \sum_{m=0}^{\infty} (a_m^{\text{outer}(1)} y_2 \text{Re}_m^{(1)}(c_2, \xi_2) + a_m^{\text{outer}(2)} y_2 \text{Re}_m^{(2)}(c_2, \xi_2)) \text{De}_m^n(c_2) \quad (71)$$

$$\sum_{m=0}^{\infty} (a_m^{\text{inc}} c \text{Re}_m^{(1)'}(c, \xi_2) + a_m^{\text{scat}} c \text{Re}_m^{(3)'}(c, \xi_2)) \text{De}_m^n(c) \\ = \sum_{m=0}^{\infty} (a_m^{\text{outer}(1)} c_2 \text{Re}_m^{(1)'}(c_2, \xi_2) + a_m^{\text{outer}(2)} c_2 \text{Re}_m^{(2)'}(c_2, \xi_2)) \text{De}_m^n(c_2) \quad (72)$$

The odd elliptic-cylinder harmonic coefficients obey a similar equation family.

If the inner region is a perfect conductor, we need only be concerned with the vanishing of the total tangential electric field at its surface. Thus, in that case, we can ignore eq. (69) which pertains to continuity of H_z . Moreover, we know that a_m^{inner} will vanish if the inner material is a perfect conductor. This has the effect of decoupling the elliptic harmonics from each other at the inner interface; eq. (70) reduces to

$$a_m^{\text{outer}(1)} \text{Re}_m^{(1)'}(c_2, \xi_1) + a_m^{\text{outer}(2)} \text{Re}_m^{(2)'}(c_2, \xi_1) = 0 \quad (73)$$

Equations (71) and (72) do not simplify.

The problem of a perfectly conducting ellipse or strip confocally coated by a dielectric is probably by far the closest replication of a stealth wing which there is any chance of solving canonically. As such, this problem is of great importance in testing out numerical codes for RCS reduction.

SUMMARY

In this report, we have presented canonical solutions for 2D TM electromagnetic scattering by lossy, layered circular cylinders; thin dielectric strips; thin perfectly conducting strips; and lossless, conformally layered elliptic cylinders.

These canonical solutions have been used to check out a TDFD code designed to give the monostatic and bistatic RCS of a generalized cylinder. (The TDFD result undergoes a Fourier and a near-field to far-field transformation before yielding an RCS which can be checked against the canonical results.)

The TDFD code can handle cylinders containing abrupt electrical discontinuities, including conducting or resistive cards, anisotropy in the plane of the cylinder, and frequency dependence in ϵ , μ and σ .

The only major limitation we have found on the TDFD code is that about 16 cells are required to resolve the shortest wavelength of interest. Also, about 80 cells must be interposed between the scatterer and the outer boundary to isolate the reactive field of the scatterer from outer boundary effects.

REFERENCES

1. Richmond, J.H., "Scattering by Thin Dielectric Strips, IEEE Trans. Antennas & Propagat., Vol. AP-33, pp. 64-68, January 1985.
2. Uslenghi, P.L.E. and N. R. Zitran, "The Elliptic Cylinder," in Electromagnetic and Acoustic Scattering by Simple Shapes, pp. 129-180, edited by J.J. Bowman, T.B. Senior, and P.L.E. Uslenghi. North Holland Publishing Co., 1969.
3. Blanch, G., Tables Relating to Mathieu Functions, New York, Columbia University Press, 1951.
4. Stratton, J.A., Electromagnetic Theory, New York, McGraw-Hill Book Company, 1941, pp. 375-387.
5. Abramowitz, M. and I.A. Stegun, Handbook of Mathematical Functions, Washington, DC, National Bureau of Standards, June 1964, pp. 721-750.
6. Hodge, D.B., "The Calculation of the Eigenvalues and Eigenfunctions of Mathieu's Equation," Ohio State University, ElectroScience Laboratory, Report 2902-4, June 1971.
7. Longmire, C.L. and H.J. Longley, "Time Domain Treatment of Media with Frequency-Dependent Electrical Parameters," DNA 3167F, 23 September 1973.
8. Yee, K.S., "Numerical Solution of Initial Boundary Value Problems Involving Maxwell's Equations in Isotropic Media," IEEE Trans. Antennas & Propagat., Vol. AP-14, pp. 302-307, May 1966
9. Longmire, C.L., "State of the Art in IEMP and SGEMP Calculations," IEEE Trans. Nuc. Sci., Vol. NS-22, pp. 2340-2344, December 1975.
10. Holland, R., "THREDE: A Free-Field EMP Coupling and Scattering Code," IEEE Trans. Nuc. Sci., Vol. NS-24, pp. 2416-2421, December 1977.
11. Holland, R., "The EMP Tunnel Code DHTRANS," IEEE Trans. Nuc. Sci., Vol. NS-25, pp. 1404-1411, December 1978.

APPENDIX 1

TIME-DOMAIN TREATMENT OF MAXWELL'S EQUATIONS IN FREQUENCY DEPENDENT MEDIA

Introduction

Consider a medium with anisotropic, frequency-dependent electrical properties. The electrical response of such a material may be fairly generally described by

$$\nabla \times \underline{H} = \underline{J}(t) + \underline{J}_f(t) \quad (1)$$

where $\underline{J}_f(t)$ is a forced current and

$$\underline{J}(t) = \underline{\sigma}_0 \cdot \underline{E}(t) + \underline{\epsilon}_\infty \cdot D\underline{E}(t) + \int_{-\infty}^t \underline{K}(t-t') \cdot D\underline{E}(t') dt' \quad (2)$$

with D indicating the time-derivative operator. In this formulation, $\underline{\sigma}_0$, $\underline{\epsilon}_\infty$, and $\underline{K}(t-t')$ are second-rank tensors.

The frequency-domain form of eq. (2) is

$$\underline{J}(\omega) = \left[\underline{\sigma}_0 + i\omega \underline{\epsilon}_\infty + i\omega \int_0^\infty e^{-i\omega u} \underline{K}(u) du \right] \cdot \underline{E}(\omega) \quad (3)$$

Separation of eq. (3) into real and imaginary parts gives representations for the frequency-dependent conductivity and permittivity tensors,

$$\underline{\sigma}(\omega) = \underline{\sigma}_0 + \text{Re} \left[i\omega \int_0^\infty e^{-i\omega u} \underline{K}(u) du \right] \quad (4)$$

$$\underline{\epsilon}(\omega) = \underline{\epsilon}_{\infty} + \text{Re} \left[\int_0^{\infty} e^{-i\omega u} \underline{K}(u) du \right] \quad (5)$$

Longmire and Longley⁷ have considered the scalar version of this formulation for the special case when $K(u)$ can be expressed as an exponential series,

$$K(u) = \sum_{m=1}^M a_m e^{-\beta_m u} \quad (6)$$

For this situation, eq. (2) may be rewritten

$$\underline{J}(t) = \sigma_0 \underline{E}(t) + \epsilon_{\infty} D \underline{E}(t) + \sum_{m=1}^M a_m \underline{J}_m(t) \quad (7)$$

with

$$\underline{J}_m(t) = e^{-\beta_m t} \int_{-\infty}^t D \underline{E}(t') e^{\beta_m t'} dt' \quad (8)$$

Equation (8) is equivalent to the differential equation

$$D \underline{J}_m(t) = D \underline{E}(t) - \beta_m \underline{J}_m(t) \quad (9)$$

Longmire and Longley assumed that materials could be represented by the exponential series of eq. (6) with one term for each decade of frequency over the spectrum of interest. This is equivalent to doing a Prony expansion of $K(u)$ [or $\sigma(\omega)$ and $\epsilon(\omega)$] with the poles forced to be spaced at

$$s_m = 10^{m+m_0} - \beta_m \quad (10)$$

While this assumption has been claimed to be reasonably accurate for wet soil, it would seem generally more correct to determine the poles from a Prony analysis of the medium's measured frequency-dependent characteristics. This is especially likely to be true if the material exhibits rapid variation in σ and ϵ with frequency.

State Theory Applications

Let us first assume the Prony analysis reveals no complex-conjugate pole pairs. In general, the a_m will be second rank tensors, but the β_m will only be scalars. Then for every pole, each component of J_m will obey

$$DE_i - DJ_{mi} - \beta_m J_{mi} = 0 \quad m = 1 - M, i = 1 - 3 \quad (11)$$

Additionally, the tensor form of eq. (7) gives

$$\epsilon_{\infty ij} DE_j + \sigma_{0ij} E_j + \sum_{m=1}^M a_{mij} J_{mj} = J_j \quad i, j = 1 - 3 \quad (12)$$

where

$$J_j = (\nabla \times \underline{H} - \underline{J}_f)_j \quad (13)$$

Equations (11) and (12) constitute a set of $3(M+1)$ coupled first order differential equations.

If anisotropy and frequency dependence were not present, the usual method of numerical solution would be explicit time-domain finite differencing. In this method, \underline{E} and \underline{H} evaluation points alternate both spatially and temporally using a well-tested leapfrog arrangement.⁸⁻¹⁰ In this arrangement, no two equations are coupled, and $E_x^{n+1/2}(I,J,K)$ means E_x evaluated at $((I + 1/2)\Delta X, J\Delta Y, K\Delta Z, (n + 1/2)\Delta t)$.

However, the present system of equations requires the three E_j 's and $3M J_{mj}$'s all to be evaluated simultaneously. While this cannot be done using conventional time-domain finite differencing, state theory does indicate an appropriate generalization of time-domain finite differencing.

First, let us consider the case where anisotropy, but not frequency dependence, is present,

$$[\epsilon_\omega] D[E] + [\sigma_0][E] = [J] \quad (14)$$

This matrix differential equation has a homogeneous solution

$$[E]_h = e^{-[\epsilon_\omega]^{-1}[\sigma_0]t} [A] \quad (15)$$

and a particular solution

$$[E]_p = [\sigma_0]^{-1}[J] \quad (16)$$

giving a general solution

$$[E] = e^{-[\epsilon_\omega]^{-1}[\sigma_0]t} [A] + [\sigma_0]^{-1}[J] \quad (17)$$

The constant vector $[A]$ may be evaluated at $(n - 1/2)\Delta t$:

$$[E]^{n-1/2} = [A] + [\sigma_0]^{-1}[J]^n \quad (18)$$

This gives the new E-field vector in terms of the old,

$$[E]^{n+1/2} = e^{-[\epsilon_\omega]^{-1}[\sigma_0]\Delta t} [E]^{n-1/2} + \left([I] - e^{-[\epsilon_\omega]^{-1}[\sigma_0]\Delta t} \right) [\sigma_0]^{-1}[J]^n \quad (19)$$

Similar exponential matrix techniques have been reported for time-domain solution of generalized multi-conductor transmission lines.¹¹ In the previous work, one may see how to evaluate eq. (19) if $[\sigma_0]$ is singular or if $[\epsilon_\omega]^{-1}[\sigma_0]\Delta t$ has arbitrarily large elements. Basically, matrices are exponentiated using the power-series representation of an exponential.

If frequency dependence is present, the $[E]$ vector of eqs. (14) - (19) becomes replaced by

$$[E] \rightarrow \begin{bmatrix} \underline{E} \\ \underline{J}_1 \\ \vdots \\ \underline{J}_M \end{bmatrix} = [E'] \quad (20)$$

The $[\epsilon_\omega]$ matrix becomes

$$[\epsilon_\omega] \rightarrow \begin{bmatrix} \underline{\epsilon}_\omega & \underline{0} & \cdots & \underline{0} \\ \underline{I} & -\underline{I} & \cdots & -\underline{I} \\ \vdots & \vdots & \ddots & \vdots \\ \underline{I} & -\underline{I} & \cdots & -\underline{I} \end{bmatrix} = [\epsilon'] \quad (21)$$

and the $[\sigma_0]$ matrix becomes

$$[\sigma_0] \rightarrow \begin{bmatrix} \underline{\sigma}_0 & \underline{a}_1 & \cdots & \underline{a}_M \\ 0 & -\beta_1 \underline{I} & \cdots & 0 \\ \vdots & \vdots & \ddots & \vdots \\ 0 & 0 & \cdots & -\beta_M \underline{I} \end{bmatrix} = [\sigma'] \quad (22)$$

Lastly, the forcing vector becomes

$$[J] \rightarrow \begin{bmatrix} \underline{J} \\ 0 \\ \vdots \\ 0 \end{bmatrix} = [\underline{J}'] \quad (23)$$

Then the matrix equation for simultaneous advancement of \underline{E} and the \underline{J}_m is

$$[\underline{E}']^{n+1/2} = e^{-[\epsilon']^{-1}[\sigma']\Delta t} [\underline{E}']^{n-1/2} + \left([\underline{I}] - e^{-[\epsilon']^{-1}[\sigma']\Delta t} \right) [\sigma']^{-1} [\underline{J}']^n \quad (24)$$

In the past, time-domain finite differencing has not often considered anisotropy. Frequency-dependent effects have been included by using the old $\underline{J}_m^{n-1/2}$ to find the new $\underline{E}^{n+1/2}$. (This decouples \underline{E} from the \underline{J}_m in eq. (12).) Then the new $\underline{E}^{n+1/2}$ have been used to find the new $\underline{J}_m^{n+1/2}$ from eq. (11).

Treatment of Complex Poles

If Prony analysis of the material's frequency dependence reveals complex pole pairs, a more general treatment becomes necessary. In this case, $\underline{K}(u)$ will contain terms of the form

$$\begin{aligned}
\underline{K}(u) &= \underline{b}_m \sin(\gamma_m u + \phi_m) e^{-\beta_m u} \\
&= \underline{b}_m \cos \phi_m \sin \gamma_m u e^{-\beta_m u} + \underline{b}_m \sin \phi_m \cos \gamma_m u e^{-\beta_m u}
\end{aligned} \tag{25}$$

The $\underline{J}_m(t)$ of eq. (8) now becomes

$$\begin{aligned}
\underline{J}_m(t) &= \int_{-\infty}^t \underline{DE}(t') (\cos \phi_m \sin \gamma_m (t-t') e^{-\beta_m (t-t')} \\
&\quad + \sin \phi_m \cos \gamma_m (t-t') e^{-\beta_m (t-t')}) dt' \\
&= \underline{J}_{mc}(t) \cos \phi_m + \underline{J}_{ms}(t) \sin \phi_m
\end{aligned} \tag{26}$$

where \underline{J}_{mc} and \underline{J}_{ms} are the parts of \underline{J}_m associated with $\cos \phi_m$ and $\sin \phi_m$, respectively:

$$\underline{J}_{mc}(t) = \int_{-\infty}^t \underline{DE}(t') \sin \gamma_m (t-t') e^{-\beta_m (t-t')} dt \tag{27}$$

$$\underline{J}_{ms}(t) = \int_{-\infty}^t \underline{DE}(t') \cos \gamma_m (t-t') e^{-\beta_m (t-t')} dt \tag{28}$$

Differentiation of $\underline{J}_{mc}(t)$ and $\underline{J}_{ms}(t)$ yields

$$D\underline{J}_{mc}(t) = -\beta_m \underline{J}_{mc}(t) + \gamma_m \underline{J}_{ms}(t) \tag{29}$$

$$D\mathbf{J}_{ms}(t) - D\mathbf{E}(t) - \beta_m \mathbf{J}_{ms}(t) + \gamma_m \mathbf{J}_{mc}(t) \quad (30)$$

These equations can be solved for $\mathbf{J}_{mc}(t)$ and $\mathbf{J}_{ms}(t)$ using Heavyside algebra:

$$[(D + \beta_m)^2 + \gamma_m^2] \mathbf{J}_{mc}(t) - \gamma_m D\mathbf{E}(t) \quad (31)$$

$$[(D + \beta_m)^2 + \gamma_m^2] \mathbf{J}_{ms}(t) - (D + \beta_m) D\mathbf{E}(t) \quad (32)$$

Thus, $\mathbf{J}_m(t)$ obeys the differential equation

$$[(D + \beta_m)^2 + \gamma_m^2] \mathbf{J}_m(t) - [\sin\phi_m(D + \beta_m) + \cos\phi_m \gamma_m] D\mathbf{E}(t) \quad (33)$$

In principle, equations like (33) could be added to the set of equations given by (11) and (12), and the entire ensemble solved by state theory. This approach, however, requires treatment of second-order matrix differential equations of the form

$$[A]D^2[E] + [B]D[E] + [C][E] = [F] \quad (34)$$

The homogeneous solution of this equations includes square roots and complex exponents of matrices; it is much more complicated than eqs. (14) - (19). (To the best of our knowledge, exponential differencing has never been applied even to scalar second-order differential equations.)

Consequently, when Prony analysis of the material data yields complex pole pairs, our present strategy is to fall back to the old technique for dealing with real poles: First find $\mathbf{E}^{n+1/2}$ using the old $\mathbf{J}_m^{n-1/2}$. Then use

the new $\underline{E}^{n+1/2}$ and the finite-difference form of eq. (33) to find the new $\underline{J}_m^{n+1/2}$.